

Dissertation  
submitted to the  
Combined Faculty of Natural Sciences and Mathematics  
of the Ruperto Carola University Heidelberg, Germany  
for the degree of  
Doctor of Natural Sciences

Presented by M.Sc. Anastasiia Vlasiuk

born in: Kiev, Ukraine

Oral examination: 16<sup>th</sup> March, 2021

**Retinal circuit as computational unit for  
visual information processing**

Referees: Dr. Santiago Rompani

Prof. Dr. Hannah Monyer

# Summary

Retina represents a highly complex, interconnected neural circuit that performs a variety of computations starting from the first photoreceptor synapse. Retinal ganglion cells (RGCs) are commonly described as output retinal neurons that relay visual information to the brain. As they do not form chemical synapses in the retina, RGCs are viewed as upstream signal integrators. Yet, they form electrical synapses among each other and with upstream amacrine cells. To investigate these connections and their function, we incorporated gap junctional couplings into a biologically inspired cascade modeling framework that faithfully fits RGC responses to light. This model structure is based on the knowledge of retinal anatomy and physiology. Though electrical synapses convey excitatory signals between neurons, apart from excitation, our model predicted inhibitory connections among RGCs in both salamander and mouse retinas. Experimental results confirmed that such a negative feedback effect involved gap junctions and amacrine cells. As well, modeling results suggested that inhibition between RGCs modulates their response gain without affecting their visual feature selectivity. Such gain modulation was also confirmed by the experiments. Together, our finding showed that RGCs actively participate in the visual information processing by sending feedback signals into the inner retina. To foster further investigations of retinal circuit processing capabilities, we have been also developing a recording technique that will allow to monitor signal flow in the retinal circuitry. A greater understanding of neural computation can ultimately help develop retina prosthetics. As a side project, we have also contributed to the investigations of the visual loss therapeutics. A chapter is devoted to describe our on-going collaborative efforts to examine the functional role of nerve growth factor in retinal ganglion cell survival.

# Zusammenfassung

Die Netzhaut stellt einen hochkomplexen, miteinander verbundenen neuronalen Schaltkreis dar, der ausgehend von der ersten Photorezeptorsynapse eine Vielzahl von Berechnungen durchführt. Retinale Ganglienzellen (RGCs) werden allgemein als retinale Ausgangsneuronen beschrieben, die visuelle Informationen an das Gehirn weiterleiten. Da sie keine chemischen Synapsen in der Netzhaut bilden, werden RGCs als vorgeschaltete Signalintegratoren angesehen. Dennoch bilden sie elektrische Synapsen untereinander und mit vorgeschalteten Amacrin-Zellen aus. Um diese Verbindungen und ihre Funktion zu untersuchen, haben wir Gap-junction-Kopplungen in ein biologisch inspiriertes Kaskadenmodellierungssystem eingebaut, das die Reaktionen der RGC auf Licht getreu wiedergibt. Diese Modellstruktur basiert auf dem Kenntnis der Anatomie und Physiologie der Netzhaut. Obwohl elektrische Synapsen neben der Erregung auch erregende Signale zwischen Neuronen übertragen, sagte unser Modell inhibitorische Verbindungen zwischen RGCs sowohl in der Netzhaut von Salamandern als auch von Mäusen voraus. Experimentelle Ergebnisse bestätigten, dass ein solcher negativer Rückkopplungseffekt Gap Junctions und Amacrine Zellen betrifft. Die Modellierungsergebnisse deuteten auch darauf hin, dass die Hemmung zwischen RGCs deren Reaktionsgewinn moduliert, ohne die Selektivität ihrer visuellen Merkmale zu beeinträchtigen. Diese Verstärkungsmodulation wurde durch die Experimente ebenfalls bestätigt. Zusammengefasst zeigten unsere Ergebnisse, dass RGCs aktiv an der visuellen Informationsverarbeitung teilnehmen, indem sie Rückkopplungssignale in die innere Netzhaut senden. Um weitere Untersuchungen der Verarbeitungsfähigkeiten der retinalen Schaltkreise zu fördern, haben wir auch eine Aufzeichnungstechnik entwickelt, die es erlaubt, den Signalfluss in den retinalen Schaltkreisen zu überwachen. Ein besseres Verständnis der neuronalen Berechnung kann letztlich zur Entwicklung von Netzhautprothesen beitragen. Als Nebenprojekt haben wir auch zu den Untersuchungen der Sehverlusttherapeutika beigetragen. Ein Kapitel ist der Beschreibung unserer laufenden gemeinsamen Bemühungen gewidmet, die funktionelle Rolle des Nervenwachstumsfaktors beim Überleben retinaler Ganglienzellen zu untersuchen.

# Acknowledgements

First and foremost, I would like to thank **Dr. Hiroki Asari** for allowing me to pursue a PhD in his lab, for his indispensable support and mentoring throughout. Thank you for giving me the freedom to investigate multiple directions, for your vast expertise and fruitful discussions that guided me through each stage of the process.

I would also like to thank my thesis advisory committee members, **Prof. Dr. Paul Heppenstall** and **Dr. Alba Diz-Muñoz**, for their guidance, and **Prof. Dr. Hannah Monyer**, apart from her advices, for all the scientific and personal inspiration.

I would also like to acknowledge our collaborators, **Dr. Silvia Marinelli** and **Dr. Laura Latini**, for giving me opportunity to contribute to their exciting project, for their support and enthusiasm.

My sincere gratitude goes to all the members of Asari lab, past and present, for creating such a great working environment on both professional and personal levels. Thank you, **Tom Boissonnet**, for your friendship and technical support, and, **Dr. Dmitry Molotkov**, for all the mountain adventures and your help in the lab. I also give a credit to **Harsh Kanodia** for the experiments with retinal slices. I extend my appreciation to all the people I met at EMBL who made it feels like my second home.

This work would not be possible without the help of EMBL staff. I am grateful to **Dr. James Sawitzke** for making viruses, **Alessandra Pisaniello** and mouse facility staff for taking care of all the mice used in this work. Thank you, **Dr. Santiago Rompani**, for your advice with viruses, injection techniques and for reviewing our manuscript together with **Dr. Cornelius Gross**.

I am very grateful to all my friends back home and all-around Europe. Thank you, **Olga**, for all the fun times here in Rome. Big thanks to you, **Kseniia**, for your love and support regardless of the distance between us.

Special thanks to you, **Daniel**, for your great support during the most stressful times and for bringing so much joy and happiness into my life.

Last but not least, I would like to thank my parents **Victoria** and **Andrey**, my sisters and brothers, for their enormous unconditional love. Thanks for always believing in me and staying my safe harbor that refills my energy.

# Table of Contents

<b>SUMMARY.....</b>	<b>1</b>
<b>ZUSAMMENFASSUNG.....</b>	<b>2</b>
<b>ACKNOWLEDGEMENTS.....</b>	<b>3</b>
<b>FIGURE LIST .....</b>	<b>6</b>
<b>ABBREVIATIONS .....</b>	<b>8</b>
<b>1 INTRODUCTION .....</b>	<b>10</b>
1.1 PARALLEL IMAGE PROCESSING BY THE RETINA .....	10
1.2 THE ROLE OF THE ELECTRICAL SYNAPSES .....	15
1.3 NEURAL ACTIVITY MODELLING .....	18
1.4 BIOLOGICALLY RELEVANT CASCADE MODEL .....	22
1.5 AIM: INVESTIGATING THE FUNCTION OF RGCs GAP-JUNCTIONAL COUPLINGS.....	23
<b>2 RETINAL GANGLION CELLS FEEDBACK TO THE INNER RETINA .....</b>	<b>25</b>
2.1 MATERIALS AND METHODS .....	25
2.1.1 <i>Modeling datasets.....</i>	25
2.1.2 <i>Cell selection criteria.....</i>	26
2.1.3 <i>Model formalism.....</i>	27
2.1.4 <i>Model fitting and assessment.....</i>	28
2.1.5 <i>Model analysis .....</i>	30
2.1.6 <i>Electrophysiology.....</i>	31
2.1.7 <i>Visual stimulation.....</i>	32
2.1.8 <i>Analysis of the optic nerve stimulation in the dark.....</i>	32
2.1.9 <i>Analysis of the simultaneous stimulation of the optic nerve and photoreceptors.....</i>	33
2.2 RESULTS .....	34
2.2.1 <i>Cascade models with couplings estimate visual responses of retinal ganglion cells better than non-coupled models.....</i>	34
2.2.2 <i>Coupled model predicts both excitatory and inhibitory effects of the RGC cross-talk....</i>	40
2.2.3 <i>RGCs cross-talk upon optic nerve stimulation.....</i>	45
2.2.4 <i>Amacrine cells and gap junctions are involved in RGC cross-talk.....</i>	48
2.2.5 <i>RGC visual response gain is modulated by negative feedback signaling .....</i>	50
2.3 DISCUSSION.....	54
2.3.1 <i>Evolutionary conserved mechanism .....</i>	54
2.3.2 <i>Dopamine regulation.....</i>	55
2.3.3 <i>Future directions .....</i>	56
2.4 PUBLICATION .....	57

<b>3</b>	<b>NERVE GROWTH FACTOR EFFECT ON DEVELOPING RETINA.....</b>	<b>58</b>
3.1	INTRODUCTION .....	58
3.1.1	<i>Retinal waves refine circuit formation.....</i>	58
3.1.2	<i>Microglia in the developing retina of a mouse.....</i>	59
3.1.3	<i>Aim of the experiments.....</i>	60
3.2	MATERIALS AND METHODS.....	61
3.2.1	<i>Electrophysiology .....</i>	61
3.2.2	<i>Data Analysis .....</i>	62
3.3	RESULTS .....	62
3.3.1	<i>Nerve growth factor facilitates retinal waves.....</i>	62
3.3.2	<i>NGF acts through binding to TrkA receptor .....</i>	65
3.3.3	<i>Microglia effect on retinal waves.....</i>	66
3.4	DISCUSSION.....	66
<b>4</b>	<b>SIMULTANEOUS RECORDING OF ALL RETINAL CELL LAYERS.....</b>	<b>68</b>
4.1	MATERIALS AND METHODS.....	68
4.1.1	<i>Viruses .....</i>	68
4.1.2	<i>Mouse lines.....</i>	69
4.1.3	<i>Intravitreal injection .....</i>	69
4.1.4	<i>Systemic injection.....</i>	70
4.1.5	<i>Retina dissection .....</i>	70
4.1.6	<i>Electroporation and bulk loading .....</i>	70
4.1.7	<i>Two-photon imaging .....</i>	71
4.1.8	<i>Visual stimulation.....</i>	71
4.1.9	<i>Analysis.....</i>	72
4.2	RESULTS AND DISCUSSION .....	72
4.2.1	<i>Monitoring retinal slices .....</i>	72
4.2.2	<i>Calcium indicators delivery .....</i>	74
4.2.3	<i>Z-scanning technique.....</i>	77
4.2.4	<i>Transgenic mouse lines.....</i>	79
4.2.5	<i>Future directions .....</i>	80
	<b>BIBLIOGRAPHY .....</b>	<b>82</b>

## Figure list

Figure 1.1 A schematic of the laminar structure of the retina.

Figure 1.2 Schematics diagram of gap junctions between retinal cells formed by different connexin types.

Figure 1.3 Illustration of reverse correlation method.

Figure 1.4 Sigmoidal nonlinearity illustration.

Figure 1.5 Illustration of neural response nonlinearity calculation.

Figure 1.6 Schematic comparison of the retinal circuit (Left) and the LNFDSTNF model (Right).

Figure 2.1 Model schemes and example dataset.

Figure 2.2 Correlation analysis of the coupled RGCs.

Figure 2.3 Coupled models outperform non-coupled ones.

Figure 2.4 Coupled model suppresses false positive activity.

Figure 2.5 Positive couplings occur among more proximal cells than negative.

Figure 2.6 Latency of positive couplings is faster than of negative.

Figure 2.7 Comparison of couplings bidirectionality.

Figure 2.8 Ganglion cell module processing is not influenced by couplings.

Figure 2.9 Optic nerve stimulation experimental scheme.

Figure 2.10 Optic nerve stimulation allows to detect RGC cross-talk.

Figure 2.11 Enhanced and suppressed activity is observed upon optic nerve stimulation in both, mouse and salamander, cells regardless of antidromic spike presence.

Figure 2.12 Electrical synaptic transmission is required for negative feedback between RGCs.

Figure 2.13 Inhibitory synaptic transmission is required for negative feedback between RGCs.

Figure 2.14 Visual response gain is modulated by the negative feedback in salamander retina.

Figure 2.15 Visual response properties are modulated by the negative feedback in mouse retina.

Figure 3.1 Example recording of retinal waves with NGF application.

Figure 3.2 NGF increases wave frequency without affecting peak firing rate.

Figure 3.3 Blocking TkaA receptor attenuates NGF effect.

Figure 3.4 Blocking microglial cells attenuates NGF effect.

Figure 4.1 Retinal slice electroporated with calcium indicator OGB1 (green) in the presence of SR101 (red) indicating dead cells.

Figure 4.2 GCaMP expression pattern in the retina explants.

Figure 4.3 Example recording with RGC visual responses estimated from calcium imaging.

Figure 4.4 Schematic diagram of the imaging planes in the whole-mount retina preparation.

Figure 4.5 Example XZ-scanning recordings of the whole-mount retinas infected with rAAV7m8::EF1 $\alpha$ -jGCaMP7f.

## Abbreviations

RGC:	Retinal ganglion cell
HC:	Horizontal cell
BC:	Bipolar cell
RBC:	Rod bipolar cell
AC:	Amacrine cell
AII:	Amacrine cell type II
mGluR6:	Metabotropic glutamate receptor 6
TRPM1:	Transient receptor potential cation channel subfamily M member 1
AMPA:	$\alpha$ -amino-3-hydroxy-5-methyl-4-isoxazolepropionic acid
GABA:	$\gamma$ -aminobutyric acid
RNA:	Ribonucleic acid
STA:	Spike-triggered average
LN:	Linear-nonlinear model
LNFDSCNF:	Linear-nonlinear-feedback-delayed-sum-nonlinear-feedback model
BCM:	Bipolar cell module
ACM:	Amacrine cell module
GCM:	Ganglion cell module
LNSN:	Linear-nonlinear-sum-nonlinear model
LNFDSCNF:	Linear-nonlinear-feedback-delayed-sum-coupling-nonlinear-feedback model
LNSCN:	Linear-nonlinear-sum- coupling-nonlinear model
PSTH:	Peri-stimulus time histogram
MFA:	Meclofenamic acid
PTX:	Picrotoxin
STR:	Strychnine
NGF:	Nerve growth factor
TrkA:	Tyrosine kinase receptor A
ANOVA:	Analysis of variance
AAV:	Adeno-associated virus

WPI:	World precision instruments
MCE:	Mixed cellulose esters
SR101:	Sulphorodamine-101
OGB1:	Oregon Green 488 BAPTA-1
DMSO:	Dimethyl sulfoxide
DLP:	Digital light processing projector
LED:	Light emitting diode
CaImAn:	Calcium imaging analysis tool
ONL:	Outer nuclear layer
OPL:	Outer plexiform layer
INL:	Inner nuclear layer
IPL:	Inner plexiform layer
GCL:	Ganglion cell layer

# 1 INTRODUCTION

## 1.1 Parallel image processing by the retina

Retina is a part of the central nervous system located at the periphery. Numerous techniques were utilized to study its anatomy, physiology and function in detail (J. R. Anderson et al., 2009; Baden et al., 2016; Denk & Detwiler, 1999; Helmstaedter et al., 2013; Meister, Pine, & Baylor, 1994; Sakata, DeLeon-Ortega, Sakata, & Girkin, 2009; Sakuranaga & Naka, 1985). Compared to the brain volume, retina is a compact sheet of tissue, approximately 200  $\mu\text{m}$  thick (Ferguson, Dominguez, Balaiya, Grover, & Chalam, 2013), with relatively small cell bodies that are densely packed in a laminar structure (Figure 1.1) (Masland, 2012; C. Zhang, Kolodkin, Wong, & James, 2017). Regardless of the size, rod photoreceptors constitute the second most numerous type of neurons in the human body after the cerebellar granule cells (Curcio, Sloan, Kalina, & Hendrickson, 1990; Walløe, Pakkenberg, & Fabricius, 2014). There are five main types of neurons in the retina: photoreceptors, horizontal cells, bipolar cells, amacrine cells and retinal ganglion cells (Masland, 2012). Yet, all these cells can be subdivided into anatomically and functionally distinct subtypes, forming a cohort of more than 100 types of neural cells in the retina (Helmstaedter et al., 2013; Sanes & Masland, 2015; Yan et al., 2020). Though each cell has a particular location in a layer of the retina it belongs to, it connects to many different neighboring cells according to its function (Baden et al., 2018; Demb & Singer, 2015; Gollisch & Meister, 2010; Masland, 2012). The diversity of such connections supports an immense computational power of the retina (Baden et al., 2018; Demb & Singer, 2015; Gollisch & Meister, 2010; Masland, 2012).

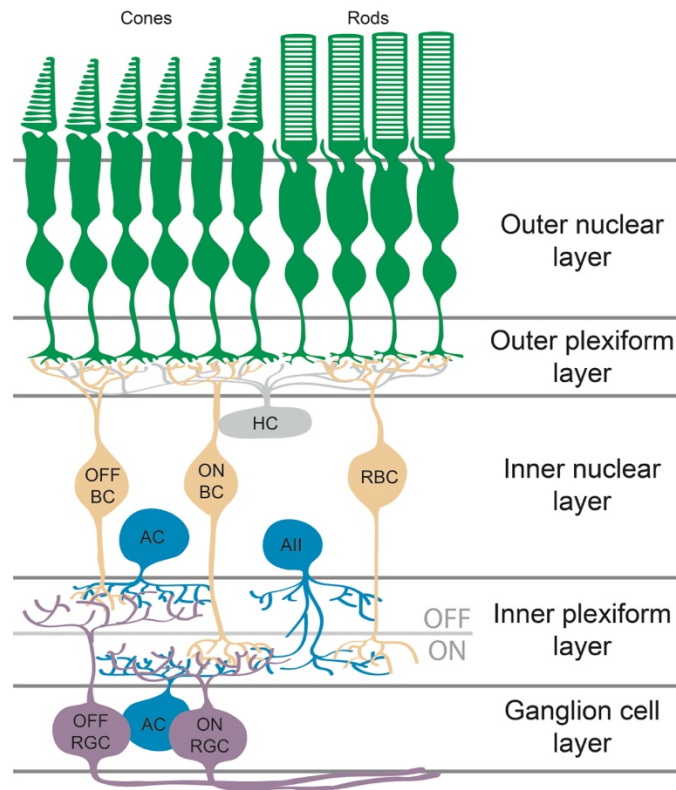


**Figure 1.1** A schematic of the laminar structure of the retina. HC – horizontal cell, BC – bipolar cell, RBC – rod bipolar cell, AC – amacrine cell, AII - AII amacrine cell, RGC – retinal ganglion cell.

Image processing in the retina starts in the most outer, photoreceptor layer (Baylor, 1996; Fu & Yau, 2007; Yau & Hardie, 2009). Photoreceptors have two main subtype specifications: 1) rods – cells that are highly sensitive to light, primarily active during the night (scotopic vision) (Herrmann et al., 2011); and 2) cons – cells that function best in daytime (photopic) conditions and are responsible for color vision (Fu & Yau, 2007). Both types of photoreceptors are active during twilight and rods also contribute to the photopic vision (C. Zhang et al., 2017). Rods express a G-coupled receptor protein, rhodopsin, that contains a light-sensitive chromophore, retinal, and are able to respond even to a single photon (Hecht, Shlaer, & Pirenne, 1942). Cones are divided into subtypes depending on the type of opsin they express. For example, in the mouse retina cones express either S-opsin or M-opsin, or both (Baden et al., 2013). “S” stands for “short” wavelength, meaning that “S-cones” respond to UV/blue light with a peak absorption at 370 nm, while “M” means “medium” wavelength – green light with a peak at 510 nm (Jacobs, Neitz, & Deegan, 1991). Photoreceptors are

glutamatergic neurons constantly releasing excitatory neurotransmitter glutamate in the dark at the synaptic terminals with bipolar and horizontal cells (Fu & Yau, 2007; Sterling & Matthews, 2005). Photon absorption by the chromophore in the photoreceptor's opsin launches a cascade of molecular reactions that lead to a cell hyperpolarization; in other words, when photoreceptor is activated by light, the release of glutamate is suppressed (Fu & Yau, 2007).

Bipolar cells respond differently to above mentioned glutamate signals from photoreceptors, depending on the types of receptors and ion channels expressed, and intracellular signaling pathways they utilize (Asari & Meister, 2012; Awatramani & Slaughter, 2000; Devries, 2000; Morgans et al., 2009). For example, bipolar cells are divided into ON or OFF types, responding to an increase or decrease of the light intensity, respectively (Wässle, Puller, Müller, & Haverkamp, 2009). ON bipolar cells express a metabotropic glutamate receptor, mGluR6, that controls the cation channel, transient receptor potential cation channel subfamily M member 1 (TRPM1) (Morgans et al., 2009; Nawy, 2000). Binding of glutamate to the mGluR6 causes the cation channel to close. Thus, in the presence of light, when glutamate is not released from the photoreceptor, TRPM1 channel opens causing depolarization of the cell. Because loss of the signal causes cell to depolarize, such synapse is called sign-inverting. On the other hand, OFF type bipolar cells' synapses are sign-conserving. They express  $\alpha$ -amino-3-hydroxy-5-methyl-4-isoxazolepropionic acid (AMPA) and kainate receptors (Devries, 2000). These are cation channels directly activated by glutamate; thus, such bipolar cells depolarize in the absence of light.

Both ON and OFF bipolar cells can be further divided into transient and sustained types, depending on how fast the glutamate receptors they express are inactivated (Awatramani & Slaughter, 2000; Devries, 2000). As well, there is a special rod bipolar cell type that preferentially makes contacts with rod photoreceptors with sign-inverting synapses (Shen et al., 2009). Bipolar cell axons stratify in a laminar fashion, with OFF-types occupying the outer part of the inner plexiform layer and ON-types, including rod bipolar cells, the inner part (Figure 1.1) (Nelson, Famiglietti, & Kolb, 1978).

There are between 10 and 20 types of bipolar cells in total in the vertebrate retina (Euler, Haverkamp, Schubert, & Baden, 2014). In most cases, each bipolar cell receives inputs from multiple cones. Exception is the fovea region in the primate retina. It is responsible for the acute vision where each retinal ganglion cell is excited by one bipolar cell that receives input from a single cone (Schein, 1988). In the mouse retina, morphological studies and single cell transcriptomic analysis defined 14 cone-contacting bipolar cell types (Helmstaedter et al., 2013; Shekhar et al., 2017). One of them, S-cone bipolar cell, preferentially makes contacts with S-cones (Haverkamp et al., 2005). Each S/M-cone is sending signal to all the other 13 cone bipolar cell types (Wässle et al., 2009). But each bipolar cell type integrates and processes these signals differently, hence dividing the very same signal into 13 parallel channels of information to be sent downstream (Euler et al., 2014).

The input to bipolar cells is even more complex due to the integration of the lateral signals from horizontal cells. In the outer part of the inner nuclear layer, a single type of horizontal cells in the mouse retina forms a large neural network interconnected by the gap junctions - fast electrical synapses (Vaney, 1991; Yamada & Ishikawa, 1965). This enables horizontal cells to rapidly sample local average light intensity from photoreceptors' glutamatergic input (Xin & Bloomfield, 1999). Then they act as a gain controller by sending inhibitory feedback to photoreceptors via chemical synapses (Thoreson & Mangel, 2012). This allows retina to function in a wide range of luminance, as well as helps to sharpen the edges of the objects of different brightness (C. J. Dong & McReynolds, 1991; Jackman, Babai, Chambers, Thoreson, & Kramer, 2011). The feed-forward input from horizontal cells to bipolar cells participate in the formation of bipolar cell receptive field center-surround structure (Sakuranaga & Naka, 1985; Thoreson & Mangel, 2012). It is also proposed that horizontal cells' activity shapes response properties of the retinal ganglion cells (Chaya, Matsumoto, Sugita, Watanabe, & Kuwahara, 2017; Drinnenberg et al., 2018). Though the first retinal synapse between photoreceptors, horizontal cells and

bipolar cells was extensively studied, new functional features of their interaction may be revealed with time (Drinnenberg et al., 2018; Jackman et al., 2011).

As described above, parallel streams of information are created by different bipolar cells. They pass those features onto even bigger variety of retinal ganglion cells (RGCs). Not all RGC types are fully characterized yet: in the mouse retina, for example, morphological and functional studies describe more than 30 types of RGCs (Baden et al., 2016; Bae et al., 2018; Sanes & Masland, 2015), while single-cell RNA sequencing defines 46 types (Tran et al., 2019). Much as for bipolar cells, RGCs can be divided into transient-ON, sustained-ON, transient-OFF, and sustained-OFF types, depending on their response polarity and kinetics (Kuffler, 1953). Further investigations showed that each type of RGC is specialized to select a specific feature from the upstream signal, e.g., detecting small moving objects, like predators (Y. Zhang, Kim, Sanes, & Meister, 2012), distinguishing motions in four different directions (Weng, Sun, & He, 2005), responding to a looming stimulus (Münch et al., 2009). As well, receptive fields of each single type of RGC tile the visual space to evenly sample a given feature (Azeredo da Silveira & Roska, 2011). In this way, the brain receives multiple representations of the same image, each with a distinct information about it (Field & Chichilnisky, 2007; Wässle, 2004).

The variability in RGC function is determined not only by their receptors, ion channels and intercellular signaling as in bipolar cells, but also by modulation arising from inhibitory interneurons, amacrine cells (Vaney, 1990). Amacrine cells receive inputs from bipolar cells and synapse back onto bipolar cells, as well as ganglion cells and other amacrine cells utilizing primarily  $\gamma$ -aminobutyric acid (GABA), glycine and acetylcholine neurotransmitters (Flores-Herr, Protti, & Wässle, 2001; MacNeil & Masland, 1998). Electron microscopy image reconstruction revealed 45 different types of amacrine cells in the mouse retina (Helmstaedter et al., 2013), while single-cell RNA sequencing divided amacrine cells into 63 types (Yan et al., 2020). They are located in the inner part of the inner nuclear layer and in the ganglion cell layer of the retina (Helmstaedter et al., 2013). They are usually found to be highly specialized on the particular computation,

where several types of amacrine cells shape the output of the particular type of RGC (Briggman, Helmstaedter, & Denk, 2011; Diamond, 2017; Famiglietti & Kolb, 1975; Kim, Shen, Hsiang, Johnson, & Kerschensteiner, 2020; Masland, 2012; Nelson & Kolb, 1985). Wide-field amacrine cells can transfer information laterally spanning big chunks of the retina space (Lin & Masland, 2006). In contrast, narrow-field amacrines are responsible for vertical information transfer between upper and lower parts of the inner plexiform layer (Macneil, Heussy, Dacheux, Raviola, & Masland, 1999; Roska & Werblin, 2001). Amacrine cells are considered to be the most diverse type of retinal cells. Yet, their functions remain largely uncharacterized.

## **1.2 The role of the electrical synapses**

Electrical synapses are constituted of connexin proteins that transverse the membranes of two adjacent neurons to form a so-called gap junction that allows direct flow of ions, electrical signals, between the two cells (Furshpan & Potter, 1959; Goodenough & Revel, 1970; Kumar & Gilula, 1992). As electrical synapses enable fast signal transfer between neighboring neurons, they are commonly involved in a synchronous firing in the brain (Gibson, Beierlein, & Connors, 2005; Hormuzdi, Filippov, Mitropoulou, Monyer, & Bruzzone, 2004; Lewis & Rinzel, 2000). Yet, retina studies revealed much more diverse functions of the gap junctional connections between neurons (Bloomfield & Völgyi, 2009; Brien & Bloomfield, 2018; Hormuzdi et al., 2004).

Most of retinal processing described above relies on chemical synapse connections. Nevertheless, not only horizontal cells, but all retinal cells form electrical synapses with their neighbors (Figure 1.2) (Bloomfield & Völgyi, 2009; Brien & Bloomfield, 2018). These electrical synapses have very diverse functionality as different retinal cell types express different connexin types whose conductance varies from several pS (Bukauskas, Angele, Verselis, & Bennett, 2002; Srinivas et al., 1999) to hundreds of nS (Lasater & Dowling, 1985). Though connexin type 36 is very common in the retina, many other types are present (Figure 1.2) (Brien & Bloomfield, 2018). Moreover, connexins in the retina

exhibit plasticity on different time scales, from milliseconds to hours (O'Brien, 2019). Thus, electrical couplings constitute an additional dynamic system of neural activity modulation in the retina.

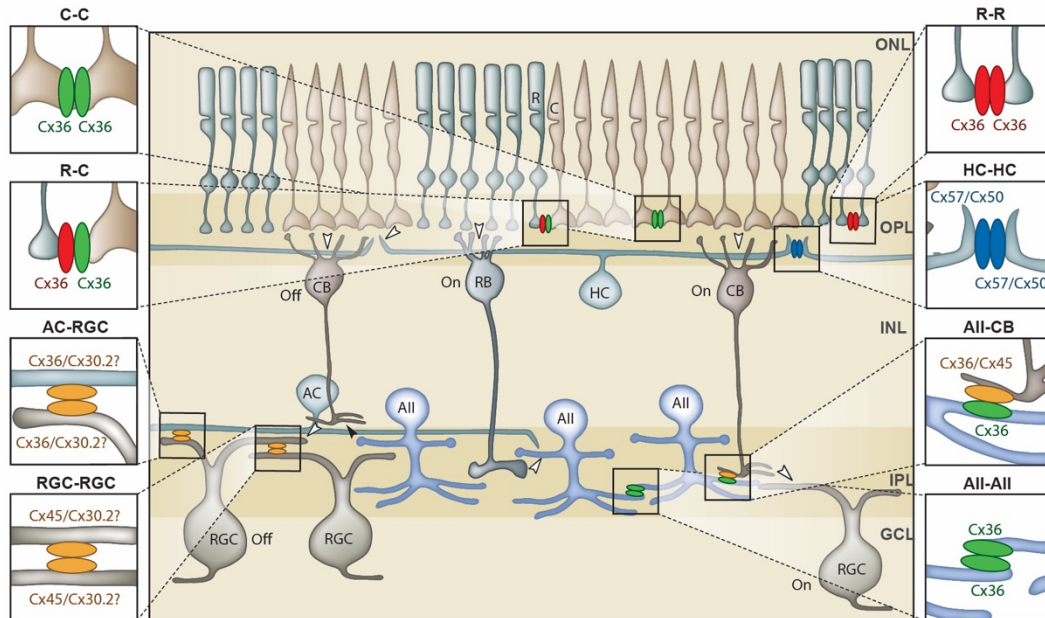


**Figure 1.2** Schematics diagram of gap junctions between retinal cells formed by different connexin types. White and black arrowheads represent excitatory and inhibitory synapses, respectively. R – rod, C – cone, HC – horizontal cell, CB – cone bipolar cell, RB – rod bipolar cell, AC – amacrine cell, AII - AII amacrine cell, RGC – retinal ganglion cell. ONL – outer nuclear layer, OPL – outer plexiform layer, INL – inner nuclear layer, IPL – inner plexiform layer, GCL – ganglion cell layer. Adapted from O'Brien (*Brien & Bloomfield, 2018*).

Best described couplings in the retina are among photoreceptors, horizontal cells and type II amacrine cells (AII). Electrical coupling between cones was shown to increase their signal-to-noise ratio (DeVries, Qi, Smith, Makous, & Sterling, 2002). Same holds true for the couplings between rods; though, this effect is observed under a dim light condition because connexins in rod's gap junctions are modulated by dopamine (Jin, Chuang, Masson, & Ribelayga, 2015). Dopamine is released under photopic conditions by dopaminergic amacrine cells in accordance with the circadian rhythm when photoreceptors stop releasing melatonin (Witkovsky & Dearry, 1991). Rods are expressing D2 type dopamine receptor that, upon binding of dopamine, activates intracellular cascade leading to a reduction of electrical synapse conductance (Akopian & Witkovsky, 1996).

Thus, coupling is stronger during the night. Similarly, gap junctional connections between rods and cones are stronger during scotopic vision, allowing rods to utilize the cone pathway for signal processing (Devries & Baylor, 1995; Raviola & Gilula, 1973; Ribelayga, Cao, & Mangel, 2008). It is referred in the literature as the secondary rod pathway. The primary rod pathway also involves gap junctions. Rods signal onto rod bipolar cells, which in turn excite, via chemical synapse, AII amacrine cells that form sign-conserving electrical synapses with ON cone bipolar cells and sign-inverting chemical synapses with OFF cone bipolar cells (Kolb & Famiglietti, 1974). Couplings between AII and between horizontal cells are also modulated by dopamine, but they exhibit a triphasic coupling behavior (Bloomfield, Xin, & Osborne, 1997; Hampson, Vaney, & Weiler, 1992; Lasater & Dowling, 1985; Xin & Bloomfield, 1999). Their coupling is weak during darkness to prevent dispersion of the single photon signals. During dim light, electrical coupling strength is increased by 7 times to ensure signal fidelity. In the bright light, it is again decreased to the similar level as in the darkness, ensuring sharpness of the image. All electrical couplings mentioned above help increase the receptive field size (Bloomfield et al., 1997; Bloomfield, Xin, & Persky, 1995; P. H. Li, Verweij, Long, & Schnapf, 2012; Ribelayga et al., 2008), confirming that gap junctions actively contribute to the primary stage of the image processing.

As is the case with chemical synapses network, electrical interactions of the retinal ganglion cells (RGCs) are possibly the most complex in the retina. RGCs of many types are connected with RGCs of the same type and/or amacrine cells (Cook & Becker, 1995; Völgyi, Chheda, & Bloomfield, 2009). Investigating the function of these interactions is more difficult than in the outer part of the retina, because conductance of electrical synapses between RGCs is low (Hidaka, Akahori, & Kurosawa, 2004). Small conductance facilitates only subthreshold effects that require direct excitatory pathway to generate RGC spike (Trenholm et al., 2014). Nevertheless, several physiological studies proved that electrical couplings do participate in signal processing. RGCs of the same type reciprocally excite each other via electrical synapses on the short timescale of 1-2 ms

(Brivanlou, Warland, & Meister, 1998b; Hu & Bloomfield, 2003; Völgyi et al., 2013). Moreover, widely separated RGCs can exhibit correlated activity on 10-100 ms timescale, mediated by gap junctional couplings to amacrine cells (Brivanlou et al., 1998b; Völgyi et al., 2013). Such long-range correlations are thought to play a role in global object recognition (K. Roy, Kumar, & Bloomfield, 2017). In one study, negative correlation between RGCs was shown to be mediated by amacrine cells (Greschner et al., 2016). Specifically, ON parasol cells in the monkey retina can excite via electrical synapsis polyaxonal amacrine cells which in turn can inhibit neighboring ON parasol cells. In one type of the ON-OFF direction-selective ganglion cells, electrical couplings were shown to facilitate signal anticipation that allows to minimize the delay of fast-moving object detection (Trenholm, McLaughlin, Schwab, & Awatramani, 2013). Only the last example demonstrates precise processing task of electrical couplings in RGCs, while function of the vast variety of gap-junctional connections remains to be described.

### **1.3 Neural activity modelling**

Given the complexity of the retinal circuitry, we are still far from being able to create a prosthetic device with a full computational power of the biological retina. Yet, arriving to our current understanding of the image processing by the retina would not be possible without computational studies. Modeling neural spike trains can be performed on different scales with various details and level of abstraction. The “integrate-and-fire” model considers a neuron as a signal accumulator that fires a spike, an action potential, when the incoming stimuli bring the membrane voltage to a defined threshold (Lapicque, 1907). The spikes are viewed as instantaneous events at the time when the threshold is reached. To describe the shape of a spike, one may use the famous Hodgkin-Huxley model (Hodgkin & Huxley, 1952). It focuses on the ionic currents to recreate in detail subthreshold activity and action potential generation on the neuronal membrane. The dynamics of these currents numerically describe phasic or bursting spiking, as well as spike-frequency adaptation (Koch, 1998). Morphologically realistic

representations are given by multi-compartment models which divide the neuron into multiple segments, from several to hundreds (Rall, 1964). Such models utilize the cable theory, discretizing the neuron and giving each of the separate compartments a specific capacity and conductivity depending on the type of receptors and ionic currents present in it. It is a powerful tool to quantitatively describe different phenomena of dendritic and somal computations. Due to mathematical complexity, however, it is very hard to conceptualize the phenomenon to describe functional property of a given neuron. More abstract representation formulated by cascade models, described below, work best to understand the function of a given sensory neuron.

In the experiment with the retina, we can present a precise sensory stimulus, a sequence of images, and record the responses of retinal ganglion cells, spikes. As we know the exact input and output of a given neuron, our goal is to find a cascade of mathematical transformations, a cascade model, from the multi-dimensional image input into binary neural output. The most basic, but very widely adopted, cascade sequence is a linear-nonlinear (LN) model (Chichilnisky, 2001).

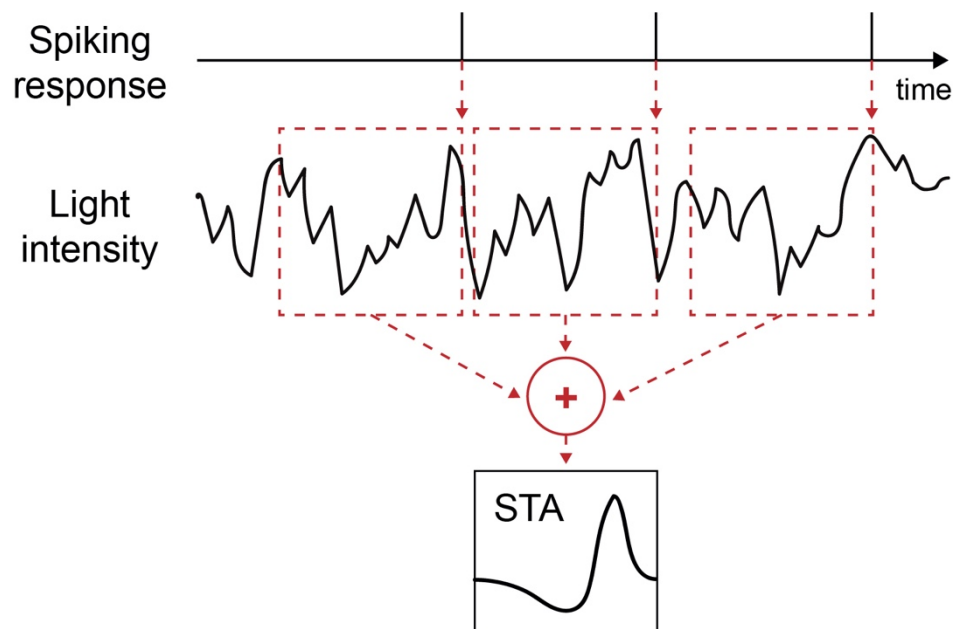


**Figure 1.3** Illustration of reverse correlation method. Top: Observed neural response – spike train. Middle: Light intensity trace of a full-field random visual stimulus. Bottom: spike-triggered average (linear filter) calculated as a mean of the stimulus intensities in a time window preceding each spike.

First, a linear (L) transformation is applied to the image in the form of a linear filter, which can be estimated for a given neuron using reverse correlation technique to calculate spike-triggered average (STA) (Figure 1.3) (Simoncelli, Paninski, Pillow, & Schwartz, 2004):

$$STA = \frac{1}{N} \sum_{n=1}^N \vec{s}(t_n), \quad (1)$$

where  $\vec{s}(t_n)$  is a vector of the stimulus frames in a particular time window (red dashed square in Figure 1.3) preceding the  $n$ -th spike and  $N$  is a total number of recorded spikes. We can define STA as an average stimulus that triggers a spike in a given neuron or, from the downstream point of view, it can be considered as the visual messages conveyed from the neuron. The selection of the time window over which we calculate the STA depends on the integration time of the upstream signals by this neuron, or so-called “memory” of the neuron. It was empirically estimated that RGCs’ memory length is between 40 and 240 ms (Tengölics et al., 2019).

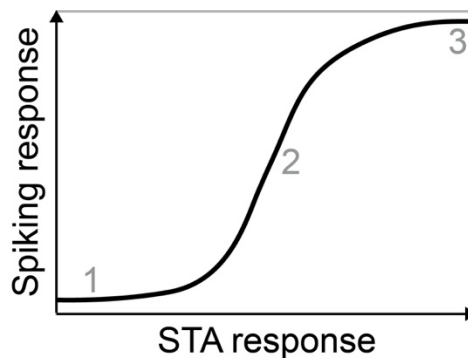


**Figure 1.4** Sigmoidal nonlinearity illustration. Neuron will respond (spiking response) to the stimulus (STA selectivity) in a nonlinear fashion: 1 – no response, 2 – linear response, 3 – response saturation.

Second, linearly transformed input is passed through a nonlinear (N) function because neurons respond nonlinearly to the stimulus. Responses of ON and OFF type RGCs most commonly follow sigmoidal nonlinearity. Intuitively, we can imagine that signals that do not match the STA of a cell will not trigger the response (Figure 1.4, region 1). Stimuli that is partially or precisely matching the STA will trigger single or multiple spikes, respectively – this corresponds to the linear part of the sigmoidal curve (Figure 1.4, region 2). And the right side of the sigmoid corresponds to the saturation of the neural response because neurons

have a physiological limitation to their highest possible firing rate (Figure 1.4, region 3).

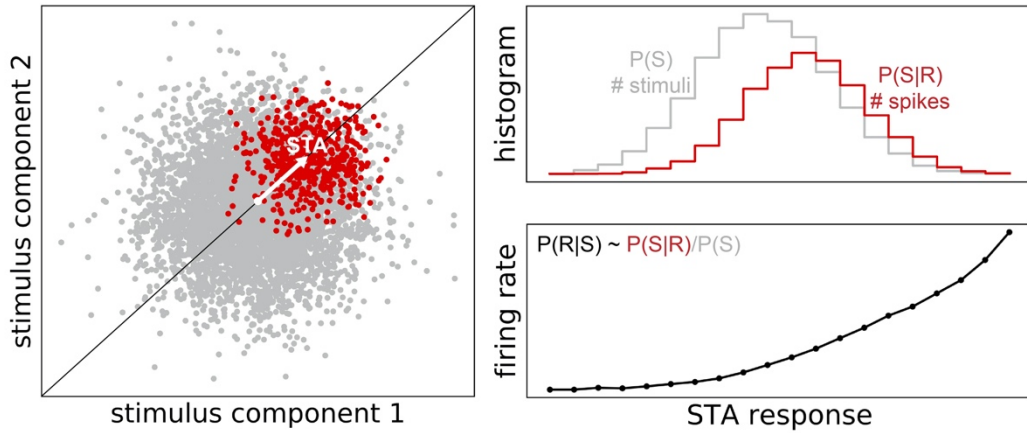


**Figure 1.5** Illustration of neural response nonlinearity calculation. Left: geometric representation of the STA in the multidimensional stimulus space viewed from 2 dimensions (stimulus component 1 and 2). Each red dot represents a stimulus segment that triggered a spike, while all other stimulus segments are in grey. STA is a center point of the spike-triggering stimulus ensemble. Top right: Histogram of all (grey) and spike-triggering (red) stimuli projected onto the STA vector direction (white arrow on the left panel). Bottom right: estimate of the nonlinearity given as a ratio (Bayes' theorem) of spike-triggered and raw histograms on top. Adapted from (*Simoncelli et al., 2004*).

Numerically, we can estimate nonlinearity function using Bayes' theorem:

$$P(R|S) \sim P(S|R)/P(S), \quad (2)$$

where  $P(R|S)$  is a probability of the response given the stimulus,  $P(S|R)$  is a probability of the stimulus given the response,  $P(S)$  is a probability of the stimulus (Figure 1.5). This approximation allows us to calculate the nonlinearity by dividing projections of the spike-triggering stimuli by all stimuli on the STA in the multi-dimensional stimulus space. Depending on the type of neuron, nonlinearity function can take other form than a sigmoid. For example, for ON-OFF RGCs, it can be approximated with a parabolic function because they respond to both an increase and decrease of the light intensity. After passing the input images through above described LN model, we obtain an estimation of the spike responses as a probability of observing a spike at any given time during stimulus presentation. Typically, this probability time series is then compared with the recorded spikes using the Pearson correlation coefficient or coefficient of determination to evaluate how well LN model fits neural response.

## 1.4 Biologically relevant cascade model

The LN model gives a good approximation of ON or OFF RGC responses without considering the upstream processing of signal by the outer retina. Real and colleagues elaborated the cascade model framework following consecutive processing of the light by different types of retinal cells creating linear-nonlinear-feedback-delayed-sum-nonlinear-feedback (LNFDSNF) model (Figure 1.6) (Real, Asari, Gollisch, & Meister, 2017).

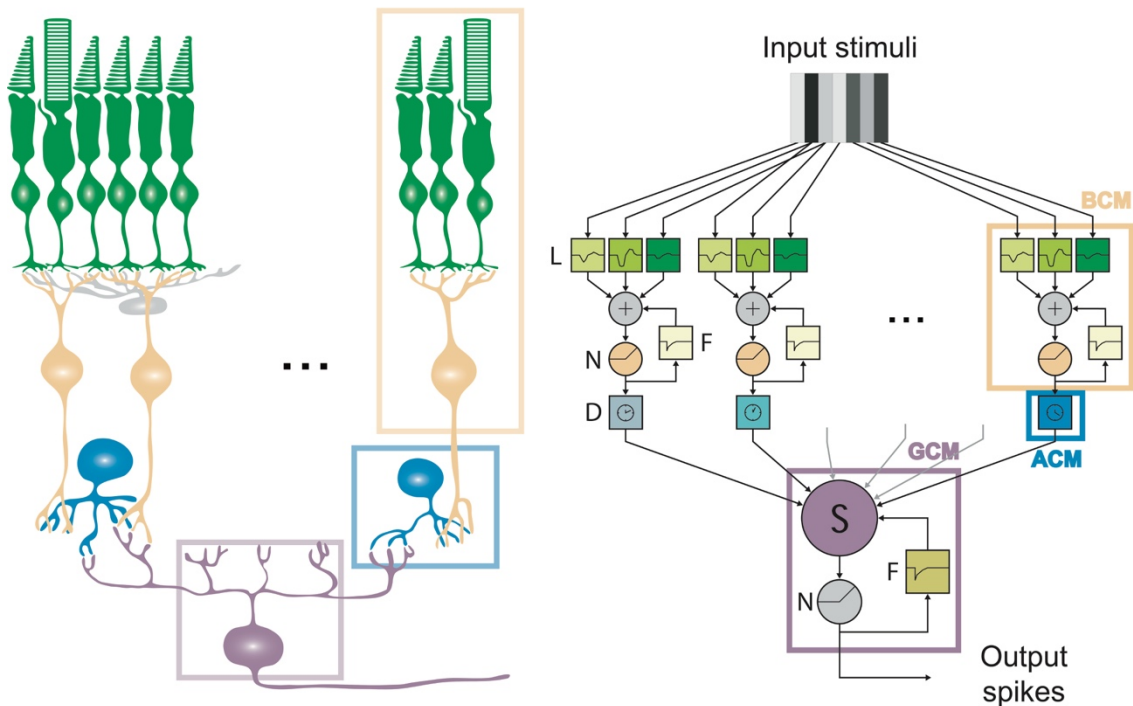


**Figure 1.6** Schematic comparison of the retinal circuit (Left) and the LNFDSNF model (Right). Stages of the model are marked next to corresponding filter representations: L – linear, N – nonlinear, F – feedback, D – delay, S – sum. Computational modules, analogous to cells, are marked with rectangles: BCM – bipolar cell module, ACM – amacrine cell module, GCM – ganglion cell module. Adapted from (Real *et al.*, 2017).

Each of the mathematical operators of the LNFDSNF model has biological meaning (Figure 1.6). These operators are grouped together to mimic computations performed by particular cell types into three modules: bipolar cell module (BCM), amacrine cell module (ACM), and ganglion cell module (GCM). The first processing stage (“LNF”) consists of multiple identical BCMs in parallel that include: spatio-temporal linear filter (L) – correlate of photoreceptor and horizontal cell signal transduction to the bipolar cell; nonlinearity (first N) –

transmission at the BC to RGC synapse; and feedback (first F) – activity-dependent reduction in the efficiency of glutamate vesicles exocytosis that depresses the synapse on short time scales as well as the reciprocal feedback inhibition from amacrine cells. The next stage includes the delays (D) that account for extra time of distant BC signal arrival imposed by amacrine cells. It consists of the same number of ACMs as BCMs. The single GCM performs the summation (S) of the BC signals by the target RGC, where positive and negative weights indicate monosynaptic excitation directly from BC and polysynaptic inhibition via amacrine cells, respectively. Finally, the GCM has its own nonlinearity (second N) to produce firing rate and feedback (second F) to account for the refractoriness and the slow inactivation of sodium current after an increase in the firing rate. Summing up, the LNFDSNF model is superior to the LN model in predicting RGC responses as it takes advantage of the accumulated knowledge about the retina and infers separate processing steps occurring the upstream of RGCs.

## **1.5 Aim: investigating the function of RGCs gap-junctional couplings**

Many principal neurons in the brain form recurrent connections that are shaping the dynamics of neural activity, from sensory information processing to decision making (Carandini & Heeger, 2012; Ito, 2000; Maass & Markram, 2004; Xiaojing, 2008). In most studies, retinal ganglion cells are characterized as a feed-forward relay of the visual information to the brain. But, as described in the second section above, RGCs have a possibility to spread signals laterally to their neighbors of the same type via electrical synapses as well as to form a feedback circuitry with the inner retina through gap-junctional connections to amacrine cells. Further investigation of the RGC dynamic interactions with upstream signals will aid understanding of global rules of neural computations.

The main question is how electrical synapses contribute to the output signals of the RGC. To tackle this question, we can use a theory-driven approach. Modelling studies help us dissect the function of a particular neural circuit and guide future experiments. Therefore, in this thesis work, we decided to extend the

cascade modeling described in the previous section by including electrical synapses. It is also interesting to know whether the contribution of gap junctions varies across species or it is a conserved feature of the retinal processing. Thus, we compare couplings between RGCs from salamander and mouse retinas.

# 2 RETINAL GANGLION CELLS FEEDBACK TO THE INNER RETINA

## 2.1 Materials and Methods

The sample size was not predetermined by any statistical methods. The significance level of 0.05 with Bonferroni correction where appropriate was used unless stated otherwise. All experimental procedures were conducted in accordance with the protocols of Institutional Animal Care and Use Committee at Harvard University or California Institute of Technology, or under the license 233/2017-PR from the Italian Ministry of Health. Matlab (Mathworks) and Python were used for the data analysis and modeling.

### 2.1.1 Modeling datasets

For the modeling of RGC responses, the data from micro-electrode array recordings in the isolated retina from salamander (Asari & Meister, 2012, 2014) and mouse (Lefebvre, Zhang, Meister, Wang, & Sanes, 2008) was used. Following LNFDSNF cascade model formalism (Real et al., 2017), responses to the random noise stimulus were modelled. In particular, presented stimulus was 1-dimensional array of adjoining bars that were changing their intensity simultaneously, randomly and independently from a binary distribution. Parameters of the stimulus were different depending on the species. Mouse RGCs were stimulated with the bars of 16.6  $\mu\text{m}$  width, luminance range between 0.5-3.8  $\text{mW}/\text{m}^2$ , and frame rate of 60 Hz. Salamander RGCs were stimulated with the bars of 80  $\mu\text{m}$  width, luminance range between 0.5-36  $\text{mW}/\text{m}^2$ , and frame rate of 100 Hz.

To estimate distances between modeled cells (Figures 2.5-6), their receptive fields were calculated from the responses to the random binary checkerboard stimulus. For mouse and salamander datasets, stimulus consisted of 30 and 83  $\mu\text{m}$  squares with 60 and 100 Hz frame rate, respectively. Reverse-correlation method was used to calculate spatiotemporal receptive fields in 0.4 s

time window. The cell was characterized as ON or OFF if the polarity of its receptive field center was positive or negative, respectively. Cell center location was estimated as a center of 3-dimensional Gaussian fit of the receptive field frame with highest contrast (Figure 2.1C). Subsequently, distance between cells is calculated as length of the vector between their centers.

### **2.1.2 Cell selection criteria**

Initially chosen datasets contained recordings from 10 salamander retinas with a total of 479 RGCs and 1 mouse retina with 35 RGCs. Cell selection criteria, described below, resulted in the final of 185 OFF and 4 ON salamander RGCs and 10 ON and 12 OFF mouse RGCs used for the modeling analysis.

1. Each electrode of the micro-electrode array can potentially record extracellular action potentials of multiple RGCs. Spike sorting analysis was previously performed to separate signals of different cells (Asari & Meister, 2012, 2014; Lefebvre et al., 2008). If spikes from multiple cells are assigned to single cell, we can observe spikes nearly coincident in time. To minimize such possibility, inter-spike intervals were calculated for each cell. The cell was removed from the analysis if inter-spike intervals of less than 1.7 ms were observed in more than 15% of its spikes.
2. Other possible consequence of spike sorting is that a given cell, detected by several electrodes, can be added to the dataset multiple times. Therefore, if the spatiotemporal receptive fields of two cells were nearly identical, the cell with a smaller number of spikes was discarded.
3. Not all cells respond robustly to the stochastic bar stimulus. A limited duration of stimulus presentation may not be sufficient to apply the cascade modeling. To assess applicability of the modeling for each cell, we first fitted the LN model (Chichilnisky, 2001; Wu, David, & Gallant, 2006) utilizing the reverse-correlation technique as described in the Introduction. For the subsequent analysis, only cells with more than 3000 spikes and with the LN model prediction (coefficient of determination, see below Eq.(5)) higher than 10% were taken.

4. Correlation between spike trains of RGCs usually comes from the common visual input. Either their receptive field may overlap and receive common upstream signals, or they are stimulated by the same set of bars if their centers lay on one axis relative to the stimulus. To model coupling interactions between RGCs, only cells with a low spike train correlation (between -0.1 and 0.1; Pearson correlation coefficient) were considered as neighbors (see below “Model formalism”) (Figure 2.2). In this way, couplings were considered only between cells without common visual input (e.g., Figure 2.1C).

### 2.1.3 Model formalism

Cascade modeling framework introduced by Real and colleagues (Real et al., 2017) was modified in this study. The model described in the Introduction, LNFDSNF or full model (Figure 1.3), was implemented, as well as reduced “linear-nonlinear-sum-nonlinear” model (LNSN) (Figure 2.4B). We modified output nonlinearity of the ganglion cell module (GCM) for both of the models to include two free parameters,  $\alpha$  and  $\theta$ , by replacing Eq.(S6) in Real et al. (2017) with the following formula:

$$y(t) = \begin{cases} 0, & \text{if } z(t) \leq \theta \\ \alpha(z(t) - \theta), & \text{otherwise,} \end{cases} \quad (\text{S6}')$$

where  $y(t)$  is the output spike probability at time  $t$  (modified with feedback filter Eq.(S7) from Real et al. for the full model),  $z(t)$  is an input signal from the previous processing step,  $\alpha$  and  $\theta$  are the slope and threshold of the N step, a half-wave rectification function. In Real et al. (2017), GCM rectification parameters were fixed with  $\alpha = 1$  and  $\theta = 0$ . While our approach allows them to vary freely, enabling us to observe variations in GCM processing stage.

Biologically, contributions of the electrical synapses arrive to the RGC soma from the dendrites. This means that they have to be included in the model before the output rectification and feedback of the GCM. Thus, coupling step, C, is added to the GCM summation step, S. The resulting models are referred as full and reduced model with coupling and they follow LNFDSNCF and LNSCN

processing steps, respectively (Figure 2.1A, B). For each of  $k$  neighboring cells we assign two free parameters:

1. Coupling strength  $\alpha_k$  that represents the number of electrical synapses between the modeled cell and its neighbor.
2. Latency of the signal  $l_k$  that accounts for the time of signal transmission from neighbor to the modeled cell.

Taken together, electrical couplings are added to the model as a delayed weighted sum of the activities of neighboring RGCs. Firing rate for each cell is binned to match the frame rate of the visual stimulus. To delay such binned activity of the neighboring cell  $r_k(t)$ , we interpolate it using integer  $[l_k]$  and decimal  $\{l_k\}$  part of the latency parameter  $l_k$  (non-negative value) according to the formula:

$$r_k^*(t) = (1 - \{l_k\})r_k(t - [l_k]) + \{l_k\}r_k(t - [l_k] - 1). \quad (3)$$

The output  $r_k^*(t)$  is a delayed activity for each  $k$ -th neighboring cell. It is then weighted by the corresponding coupling strength parameter  $\alpha_k$  and summed with the signal  $x(t)$  representing upstream chemical synapses input (S step):

$$z(t) = x(t) + \sum_k \alpha_k r_k^*(t), \quad (4)$$

where  $z(t)$  output is used as an input to Eq.(S6') to produce estimate of the firing rate of the modeled cell for the reduced model, or Eq.(S6') and Eq.(S7) in Real *et al.* for the full model.

#### **2.1.4 Model fitting and assessment**

To fit the model, custom code was written in Python programming language. NumPy and SciPy libraries were used for mathematical operations and statistics calculation, respectively. Visual stimulus served as an input to the cascade of mathematical functions that transformed it into output estimate of the firing rate of a given ganglion cell (bin size of 10 ms for salamander cells and 17 ms for mouse cells). To fit free parameters of the model, objective function was minimized with “optimize.minimize” function from SciPy library. The objective function was represented by the mean squared error between the firing rate

estimated by the model and the firing rate recorded in the experiment. Coefficient of determination was used to evaluate model performance:

$$R^2 = 1 - \frac{\sum_t (r(t) - \hat{r}(t))^2}{\sum_t (r(t) - \langle r(t) \rangle)^2}, \quad (5)$$

where  $r(t)$  and  $\hat{r}(t)$  are a recorded and model estimated firing rates, respectively, and  $\langle * \rangle$  denotes the mean. If recorded and estimated firing rates match each other perfectly, the coefficient value equals to 1. The coefficient is sensitive to the amplitude of the signals, all the matched and mismatched spikes. It can take 0 or negative values if sequences are unrelated and/or on the different order of magnitude.

Model performance was assessed on the part of the data that was not used for fitting of the free parameters. For the mouse recording, the data was divided into training - 80% and testing - 20% datasets. Stimulus for the salamander recording contained 8-12 repeats of the same testing frame sequence. Thus, the coefficient of determination was calculated using the mean firing rate over these repeats.

For the models with coupling, each cell was assigned with the surrounding cells according to cell selection criterion number 4 described above. ON and OFF RGCs receiving same visual input may have anticorrelated spiking activity. In the model, such cells can cancel each other activity if they are taken together as two surrounding cells. This may result into very high non-biologically relevant coupling strength. Thus, for each cell, we have performed model fitting separately with the neighboring cells of the same response polarity, e.g. OFF target cell with OFF neighbors, and of the different response polarity, e.g. OFF target cell with ON neighbors (Figure 2.3). As there are too little ON cells in the salamander dataset (2 per recording with a total of 4), they were not modelled with ON neighbors.

To compare model performance with and without couplings, we used paired t-test (Figure 2.3). It did not show improvement for the mouse cells modeled with cells of different response polarity (Figure 2.3B, D, right).

Therefore, this configuration was not used in the following model parameter analysis.

### 2.1.5 Model analysis

Coupling parameters in the described modeling framework are subject to noise (gray shading, Figures 2.2, 2.5-7). Such noise level was determined by minimization of LN<sub>SCN</sub> and LN<sub>FDSCNF</sub> models with spiking responses of the neighboring cells shuffled in time. Specifically, responses of the modeled cell remained the same while the timing of each response of the neighboring cell (binned at 10 and 17 ms) was randomly changed. In such way, the total number of spikes for each neighbor was preserved while all the temporal relationship with the modeled cell firing rate and visual stimulus was abolished. Thus, coupling parameters of shuffled model form a chance level distribution. Distribution of coupling strength parameters was used to determine the upper and lower bounds of the noise level (0.05 and 99.5 percentile, respectively). If coupling strength parameter of the full or reduced model (without shuffling) was within the noise level, all the parameters from a given cell pair (target cell and a given neighbor) were not included in further analysis.

After removing the noise, coupling parameters were pulled together (Figures 2.5-7). ON and OFF cells coupled to the neighbors of the same polarity showed similar trends, therefore, were analyzed together. Positively and negatively coupled cell pairs according to their coupling strength formed two distributions, between which the differences in the cell to cell distance and latency of the signal arrival were assessed by Wilcoxon rank-sum test (Figures 2.5-6). For any coupled cell pair  $i$  and  $j$ , there were two sets of parameters: when cell  $i$  is coupled to the modeled cell  $j$  and the opposite,  $j$  coupled to modeled  $i$ . We examined the symmetry of such couplings utilizing  $\chi^2$ -test (Figure 2.7).

We examined differences in the ganglion cell module (GCM) processing between coupled and non-coupled models. To compare the input from the upstream processing into the GCM, we extracted temporal signals from the summation step,  $S$  (Eq.(S9) in Real et al.). For each cell, we calculated Pearson's

correlation coefficient between these signals for the models with and without couplings (Figure 2.8A, D). For the full model, we pulled together all the feedback filters of the GCM (Eq.(S7) in Real *et al.*) (Figure 2.8B, E). As well, we calculated Pearson's correlation between distributions of parameters of the GCM nonlinearity in models with and without couplings (threshold  $\theta$  and slope  $\alpha$  in the Eq.(S6')) (Figure 2.8C, F).

### **2.1.6 Electrophysiology**

These experiments were performed by Dr. Hiroki Asari.

Retina of dark-adapted larval tiger salamander (*Ambystoma tigrinum*) or an adult wild-type mouse (*Mus musculus*; C57BL/6J strain) was isolated with an intact optic nerve attached. It was placed with a ganglion cell side down on a micro-electrode array with 61 extracellular electrodes. During the experiment, retina was perfused with oxygenated solution (equilibrated 95% O<sub>2</sub> and 5% CO<sub>2</sub> gas): Ringer's medium at room temperature for the salamander retina (in mM: NaCl, 110; NaHCO<sub>3</sub>, 22; KCl, 2.5; MgCl<sub>2</sub>, 1.6; CaCl<sub>2</sub>, 1; and D-glucose, 10); and Ames' medium at 37 °C for the mouse retina (Sigma-Aldrich, A1420). Extracellular signals were recorded by the micro-electrode array with a sampling rate of 10 kHz. Visual and/or electrical stimulation was used to excite photoreceptors and/or optic nerve, respectively. To separate signals from individual RGCs, spike-sorting was performed with a semi-automated algorithm (Pouzat, Mazor, & Laurent, 2002) written in IGOR Pro (Wave Metrics).

Optic nerve was captured with a glass electrode filled with the solution described above (Figure 2.9). Electrical stimulus was delivered to the optic nerve using custom software written in LabView (National Instrument) that was transferring commands onto stimulus isolator (Grass Instrument, SD9) to generate bipolar pulses of 10-50 V with a duration of 0.02-0.5 ms at 2/3-1 Hz. For the dark condition, it was repeated 100-200 times. With the visual stimulation, repetition number was 1300-2000. Optic nerve stimulation evoked action potentials propagating back to the ganglion cells. The latency to observe such antidromic spikes at the RGC upon stimulation was around 5 ms (Figure 2.9B, asterisk).

Within a few milliseconds after the electrical impulse it was not possible to record any spikes due to the stimulation evoked artifacts (Figure 2.8B).

For the described experiment, 19 salamander and 7 mouse retinas with intact optic nerve were recorded with a total of 885 and 368 ganglion cells signals extracted with spike-sorting, respectively. Of those, responses from 11 salamander retinas (349 RGCs) were additionally treated with a gap junction blocker (100  $\mu$ M meclofenamic acid) (Figure 2.12) and other 6 salamander retinas (380 RGCs) received treatment with inhibitory transmission blockers (100  $\mu$ M picrotoxin and 1  $\mu$ M strychnine) (Figure 2.13). Visual stimulation was used in 6 salamander retinas (167 RGCs) and 3 mouse retinas (172 RGCs). To be able to evaluate suppression between RGCs, only cells exceeding baseline firing rate of 1Hz were chosen for further analysis. Due to a very slow washout of the drug from the whole-mount preparation, it was not possible to observe reverse effect within the time window that ensures stable nerve stimulation (30-60 min). Thus, experimental results are reported only for the pre- and post-drug administration conditions.

### **2.1.7 Visual stimulation**

Visual stimulus was projected onto the photoreceptor layer from the gamma-corrected cathode-ray tube monitor (Dell E773c) through a custom-made lens system. Glass electrode for the nerve stimulation presents an obstacle that creates an uncontrollable distortion of any image with spatial structure. Therefore, full-field visual stimulation was used. Specifically, stimulus intensity was drawn randomly from a Gaussian distribution with a luminance of  $18 \pm 7$  mW/m<sup>2</sup> (mean  $\pm$  standard deviation) at a frequency of 100 Hz.

### **2.1.8 Analysis of the optic nerve stimulation in the dark**

To evaluate the result of the optic nerve stimulation in the dark for a given RGC, peri-stimulus time histogram (PSTH) was calculated with increasing bin sizes of 0-10, 10-20, 20-40, 40-80, 80-160, 160-320 and 320-640 ms (Figure 2.11). The baseline activity was computed over 320 ms prior to the electrical

stimulation. Bootstrap method (10000 repeats) with resampling over trials was used to evaluate the significance of the firing rate change relative to the baseline in each PSTH bin. Given that latency of the antidromic spike is around 5 ms, significant increase of the firing rate in the first time bin (0-10 ms) was considered to be caused by optic nerve stimulation (Figure 2.11A, first and third columns). Significant differences in all other time bins (> 10 ms) were viewed as an indirect effect of the electrical stimulation (Figure 2.11, 2<sup>nd</sup>-4<sup>th</sup> columns). For the display purpose, peri-stimulus time histograms (PSTHs) in the Figure 2.10 were calculated over 20 ms bins, blue and red shades were added to demonstrate the bins with significant decrease or increase, respectively, of the firing rate relative to the baseline (250 ms prior to the electrical stimulation).

### **2.1.9 Analysis of the simultaneous stimulation of the optic nerve and photoreceptors**

Liner filter and static nonlinear gain function, described in the Introduction, were calculated for each RGC in the 0.4 s time window (10 ms bin size) (Figures 2.14-15). We compared their parameters between the baseline and at the time of the significant change (bootstrap resampling method over trials, 10000 repeats) of the firing rate upon delivery of the optic nerve stimulation during full-field random flicker stimulus presentation (Figures 2.14B, 2.15B). In this case, PSTHs were calculated with 100 ms bin size (centered at the nerve stimulation). Baseline was taken over 500 ms window prior to the electrical stimulus. To compare linear filters (spike-triggered averages), they were characterized with an ON-OFF index for different times of interest (Figure 2.14C). The index represents a normalized difference between the maximum and minimum values of the linear filter, called peak and valley, respectively:

$$ON - OFF \text{ index} = \frac{|peak| - |valley|}{|peak| + |valley|}. \quad (6)$$

Depending on the stimulus preference of the cell, the ON-OFF index can take values between -1 for purely OFF selective cell and +1 for purely ON selective. If cell is equally responsive to both ON and OFF stimuli, index will

equal to 0. The changes in the cohort of linear filters for the enhanced and suppressed firing periods were assessed with the sign-test, while their variances were compared with the F-test (Figures 2.14-15 E, F).

To quantify corresponding differences of the static nonlinear gain functions, they were fitted with a sigmoid function  $f(x)$ :

$$f(x) = \frac{u-l}{1 + \exp^{-s(x-c)}} + l, \quad (7)$$

where  $u$  is an upper bound,  $l$  – lower bound,  $c$  – center,  $s$  – slope. Statistical significance was evaluated with a sign-test and F-test (Figures 2.14-15 G).

## 2.2 Results

### 2.2.1 Cascade models with couplings estimate visual responses of retinal ganglion cells better than non-coupled models

The aim of this project is to investigate interactions between retinal ganglion cells (RGCs). For the start, we decided to utilize a modeling approach where we have included the possibility of electrical coupling between RGCs. We have implemented cascade models from Real et al. (Real et al., 2017) to serve as a baseline estimate of RGC activity. These are: a full model “linear-nonlinear-feedback-delay-sum-nonlinear-feedback” (LNFDSNF) and a reduced model “linear-nonlinear-sum-nonlinear” (LNSN). As described in the introduction, processing steps in these models follow the anatomy and signal flow in the retina. We have modified the final nonlinearity step (see Eq(S6’) in Materials and Methods) to allow for more flexibility at the ganglion cell processing level.

We have extended the baseline models to include couplings of a target ganglion cell to the neighboring cells (LNFDSCNF and LNSCN, Figure 2.1A, B). The coupling processing step includes two free parameters for each neighboring RGC: coupling strength and latency (see Eq.(3) and (4) in Materials and Methods). Biologically, the strength of coupling depends on the conductance and number of electrical synapses between the two cells. In the model, the coupling strength parameter is given as a percentage of the activity of the surrounding cell injected into the target cell. If it is positive, we assume that the cells are directly and/or

indirectly connected by the gap junction network. A negative coupling strength can be observed if the surrounding cell is electrically coupled to the amacrine cell, which in turn inhibits the target cell. The latency parameter accounts for the delay of signal arrival from the surrounding cell. Thus, shorter latency is expected between the directly connected cells, while longer signal delays would signify indirect connections between cells. Such coupled model formalism allows us to keep the number of free parameters low to ensure efficient minimization of the objective function (see Materials and Methods). On the other hand, it remains flexible enough to detect all the possible effects of RGCs interactions including the inner retina circuitry.

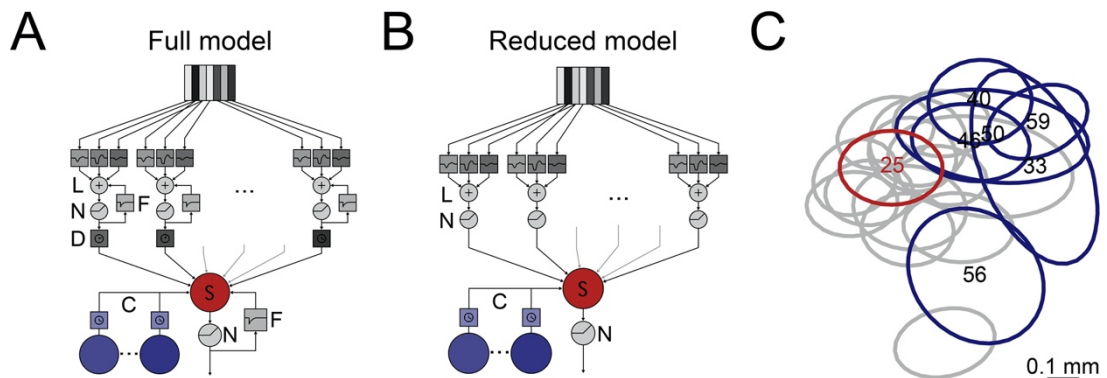


**Figure 2.1** Model schemes and example dataset. A: Full coupled model (LNFDCSCNF) with processing steps marked next to the schematic representation of their mathematical operation. LNF steps form a bipolar cell module (BCM). Each BCM receives input from 7 adjacent bars of the visual stimuli (for simplification, only 3 are illustrated). B: Reduced coupled model (LNDCSCN). C: Receptive fields (RFs) of 20 OFF RGCs recorded simultaneously from one salamander retina. As an example, RFs of a target cell is shown in red and coupled neighboring cells in blue, in grey – RFs of cells that receive significant amount of common visual input with a target cell. A and B are adopted from Real et al. (Real et al., 2017).

Coupled model takes the “flickering bars” visual stimulus and the activity of neighboring RGCs (Figure 2.1 in blue) as inputs, and outputs an estimate of the firing rate of a target cell (Figure 2.1 in red). Clearly, only cells that were recorded simultaneously can be coupled (e.g. Figure 2.1C). Also, to exclude false positive couplings, as neighbors we took only those cells that do not receive common visual input with a target cell. Lastly, for each target cell, we selected two cohort of neighbors - with the same and different response polarity. It was necessary to

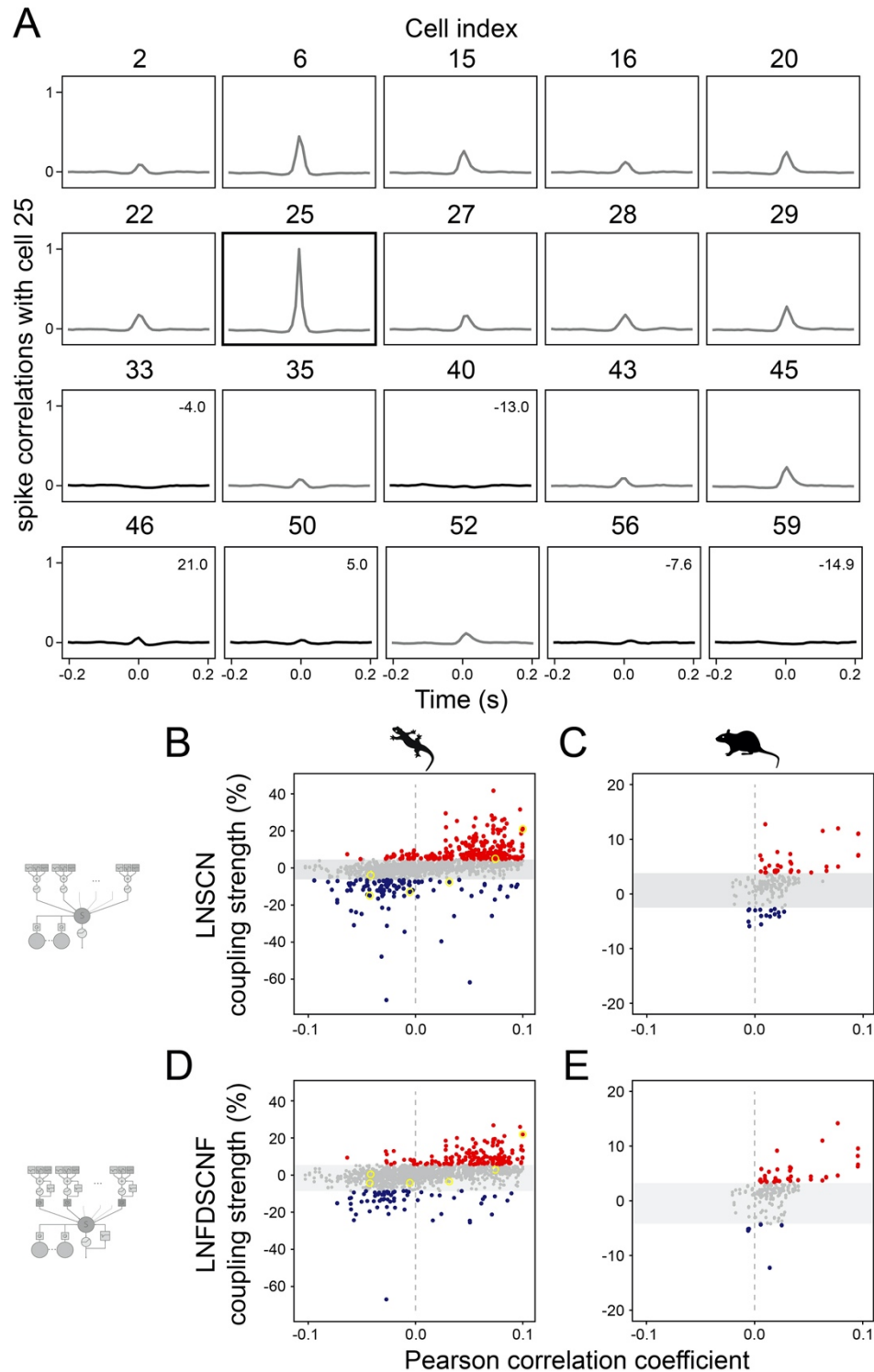


**Figure 2.2** Correlation analysis of the coupled RGCs. **A**: Cross-correlation of the spike trains between the example OFF RGC number 25 (Figure 2.1C) and all other simultaneously recorded OFF RGCs (auto-correlation in bold square). Coupling strength parameter values from LNSCN model for the target cell 25 are marked in the top right corner for each chosen neighboring cell (black curves) that satisfy low correlation criterion at the peak of cross-correlation curve ( $>0.1$ ,  $<0.1$ , see Materials and Methods). **B**, **C**: Coupling strength parameters for each cell pair (positive – red, negative - blue) in the LNSCN model are plotted as a function of Pearson correlation between spike trains (**B** – salamander, **C** - mouse). Example parameters for coupled cells from **A** are in yellow circles. Grey shading indicates parameters within noise level (see Materials and Methods). **D**, **E**: Same plot as **B** and **C** for the coupling strength parameters fitted in LNFDCNF model.

exclude the possibility of counteracting effects from two surrounding cells of different response polarity. These conditions were achieved by restricting the Pearson's correlation between the spike train of a target and neighboring cells between -0.1 and +0.1 (Figure 2.2). After fitting the models, we checked the relationship between the resulting coupling strength parameters and the correlation between spike trains of each connected cell pair. We observed strong couplings of either polarity that do not have the same sign as spike train correlation. This confirms that our coupled model paradigm works beyond simple correlation analyses.

We have successfully fitted both coupled and non-coupled models for each selected RGC from salamander and mouse retinas responding to random flickering bars stimulus (see Materials and Methods). With a part of the data not used for the fitting, model performance for each target cell was evaluated by calculating coefficient of determination,  $R^2$ , between model estimated and recorded firing rates (Eq.(5) in Materials and Methods). Fitting of the feedback filters,  $F$  steps, is the most computationally heavy and time-consuming task. Thus, we first fitted reduced models (LNSN and LN SCN). The highest improvement after adding couplings was observed for the set of salamander OFF RGCs coupled with the neighbors of the same response polarity (Figure 2.3A;  $R^2 = 0.314 \pm 0.091$  versus  $0.297 \pm 0.087$ ,  $p < 0.001$ ; mean  $\pm$  standard deviation, paired t-test). As can be seen from the Figure 2.3, there is high variability in the performance gain for different cells. It is expected considering that we observe together only a small fraction of RGC population. When we fitted full models (LNFDSNF and LNFDS CNF) to the same salamander OFF RGCs, we again observed that coupled model outperformed non-coupled one (Figure 2.3A;  $R^2 = 0.390 \pm 0.112$  versus  $0.382 \pm 0.112$ ,  $p < 0.001$ ). Though, the performance gain is smaller for the full model, it is possible that the coupling effect is partially substituted by the delay,  $D$ , and feedback filter,  $F$ , in the uncoupled full model. As will be shown later, distribution of coupling parameters is consistent for full and reduced model. Therefore, we present results of both models.

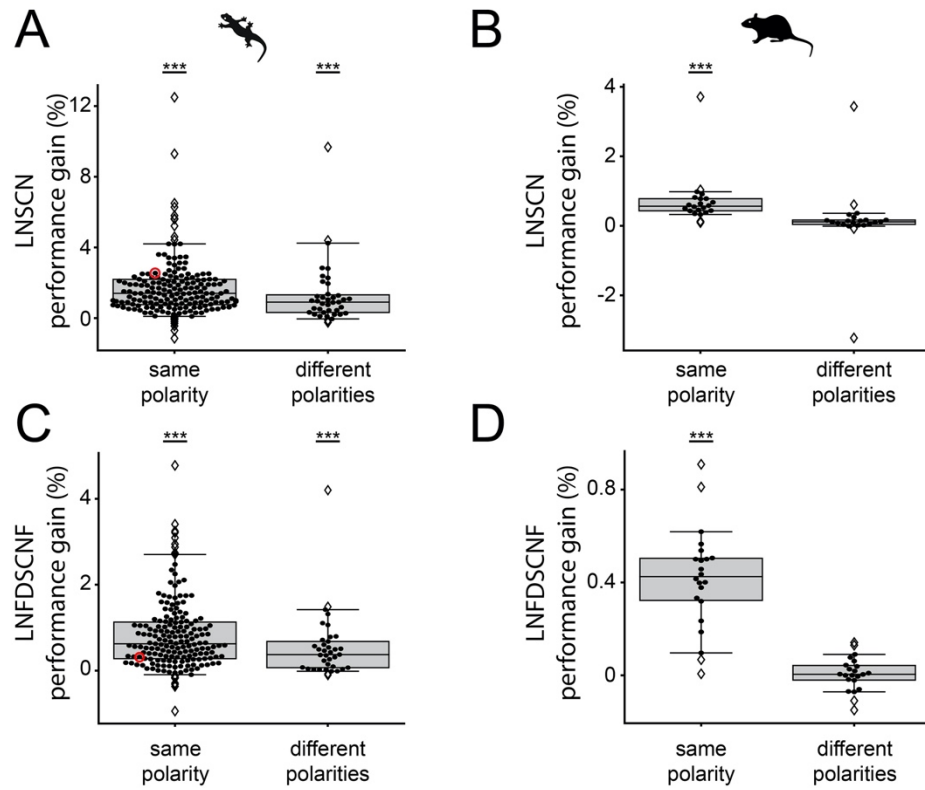


**Figure 2.3** Coupled models outperform non-coupled ones. A, B: Performance gain of the coupled LNSCN model over non-coupled LNSCN defined as difference of the coefficient of determination  $R^2$  (Eq.(5) in Materials and Methods; A – salamander, B - mouse). Each dot of a swarm plot represents a cell. Total number of cells in A: same polarity  $N=185$  OFF cell, different polarity  $N=35$  OFF cells and 4 ON cells; in B: for both, same and different response polarity,  $N=12$  OFF cell and 10 ON cells. Box plot whiskers indicate 5 and 95 percentiles. Stronger model performance increase is observed in salamander cells with same response polarity neighbors ( $\Delta R^2=0.017\pm 0.016$ , mean  $\pm$  standard deviation;  $p<0.001$ , paired t-test) than with different ( $\Delta R^2=0.013\pm 0.017$ ;  $p<0.001$ ). For mouse, coupled model outperforms non-coupled with neighbors of the same response polarity ( $\Delta R^2=0.007\pm 0.007$ ,  $p<0.001$ ) but not with the opposing response polarity neighbors ( $\Delta R^2=0.001\pm 0.010$ ,  $p>0.5$ ). Gain for the example cell #25 from Figure 2.1C is in red circle. C, D: Corresponding figures for the performance gain of the full coupled model, LNFDS CNF, over LNFDSNF. Mean gains for salamander in C: same polarity -  $\Delta R^2=0.0083\pm 0.0083$ ,  $p<0.001$ ; different polarity -  $\Delta R^2=0.0055\pm 0.0074$ ,  $p<0.001$ ; for mouse in D: same polarity -  $\Delta R^2=0.0042\pm 0.0021$ ,  $p<0.001$ ; different polarity -  $\Delta R^2=0.0001\pm 0.0007$ ,  $p>0.5$ . In all figures (\*\*\*) indicate  $p<0.001$ , (\*\*) –  $p<0.01$ , (\*) –  $p<0.05$ .

Cells of opposite response polarity contributed less to the coupled model performance in the salamander retinas (Figure 2.3 A and C;  $R^2 = 0.322\pm 0.095$  versus  $0.309\pm 0.100$ ,  $p<0.001$  for the reduced models;  $R^2 = 0.384\pm 0.100$  versus  $0.378\pm 0.100$ ,  $p<0.001$  for the full models). As no significant contribution was

observed from the cells with different response polarity in the mouse retina (Figure 2.3 B and D;  $R^2 = 0.209 \pm 0.090$  versus  $0.208 \pm 0.087$ ,  $p > 0.5$  for the reduced models;  $R^2 = 0.233 \pm 0.108$  versus  $0.233 \pm 0.108$ ,  $p > 0.5$  for the full models), parameters of this configuration were not included in the further analysis. Cells with the same response polarity in the mouse retina gave a small but significant increase in the coupled models performance gain (Figure 2.3 B and D;  $R^2 = 0.215 \pm 0.088$  versus  $0.208 \pm 0.087$ ,  $p < 0.001$  for the reduced models;  $R^2 = 0.237 \pm 0.109$  versus  $0.233 \pm 0.108$ ,  $p < 0.001$  for the full models).

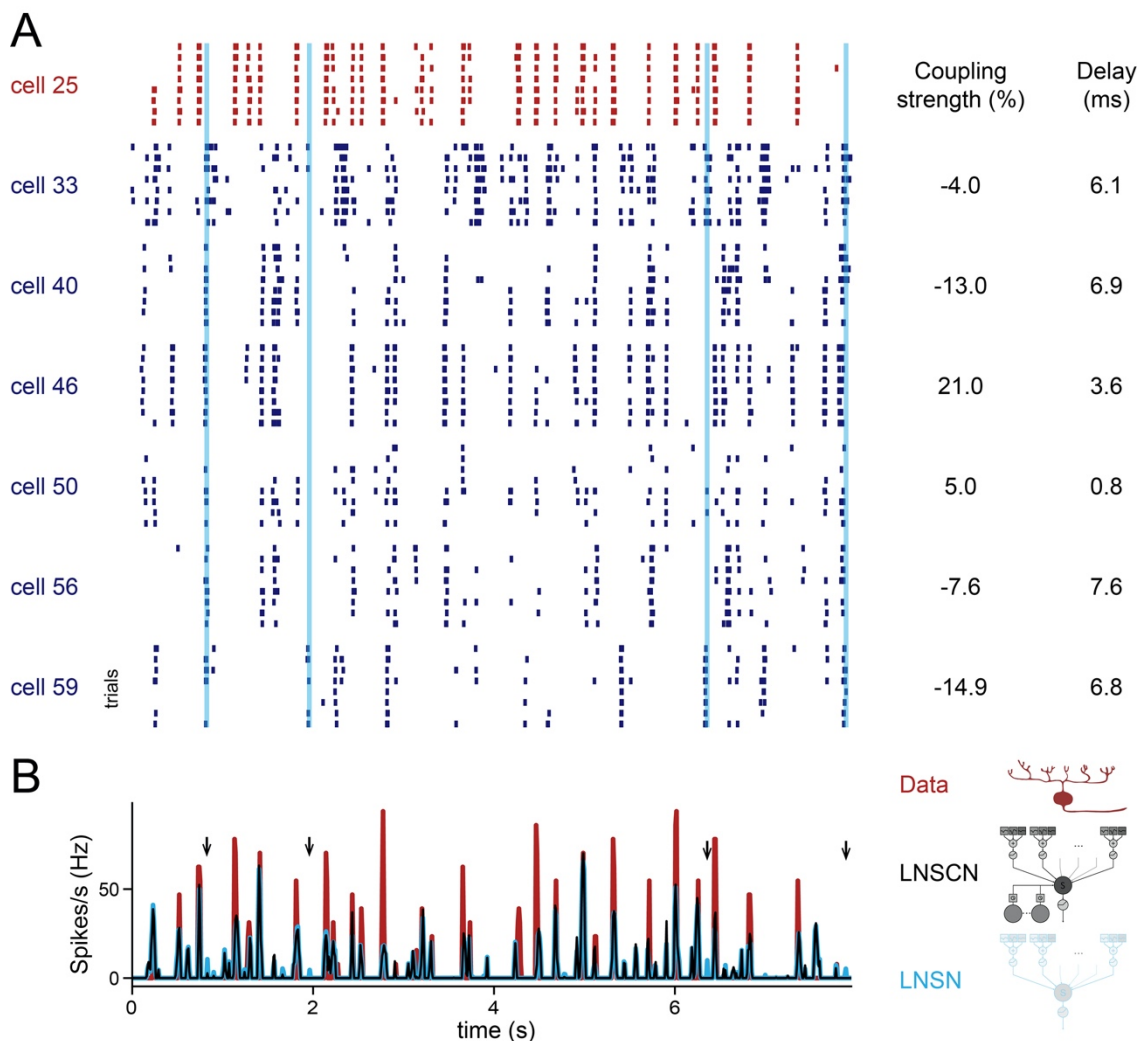


**Figure 2.4** Coupled model suppresses false positive activity. A: Raster graphs (each line is a spike) of the visual responses (8 trials) of the example target cell #25 and its neighbors (same as on Figure 2.1C). For each neighbor, coupling strength and delay parameters of LNSCN model fitted for cell #25 are shown on the right. B: Firing rate of cell #25 recorded in the experiment – red, predicted by LNSN model – cyan and by LNSCN model – black. False positive responses correctly suppressed by coupled model are indicated by black arrows (and cyan line in A).

We examined predicted spike trains produced by coupled and non-coupled models. Model without couplings often predicts RGC responses at the times when no spikes were observed even during repetitions of the same visual stimulus. Addition of couplings to the neighbors eliminates such false positive responses. Spike train investigation suggests that this effect arises from negatively coupled neighbors of the same polarity as a target cell (Figure 2.4). Taken together, results of our coupled models support the contribution of cross-talk between RGCs to their visual responses, as was suggested by the anatomical studies (Völgyl et al., 2009). Particularly, a solid contribution is observed for the cells of the same response polarity.

### **2.2.2 Coupled model predicts both excitatory and inhibitory effects of the RGC cross-talk**

We analyzed parameters of the coupled models for dataset configurations with a significant increase in the model performance over non-coupled ones. These are: OFF salamander cells with OFF neighbors, OFF and ON salamander cells with neighbors of opposite polarity, and OFF and ON mouse cells with neighbors of the same response polarity. Parameters of the last two configurations showed the same trend for ON and OFF cells. Thus they were combined for the analysis. There were only 4 ON salamander cells that passed a selection criterion, 2 per recording, meaning that only 1 neighbor would be available for modeling. Therefore, we did not model ON salamander cells with ON neighbors. Resulting parameters of reduced and full models were very similar. We report in the text the results for the reduced model, while both model results are shown on the figures and in the figure legends.

The final nonlinearity step of the ganglion cell model may attenuate small signals arriving from surrounding cells. Such signals would not influence our objective function, and the coupling parameters would be meaningless. Therefore, we defined a noise level of coupling parameters utilizing a shuffling analysis (see Material and Methods, “Model analysis”). We fitted coupled models for the unchanged target cell responses with randomly shuffled responses of neighboring

cells. Upper and lower thresholds were defined as 0.5 and 99.5 percentiles of the resulting distribution of coupling strength parameters that are expected by chance (indicated in all figures in grey).

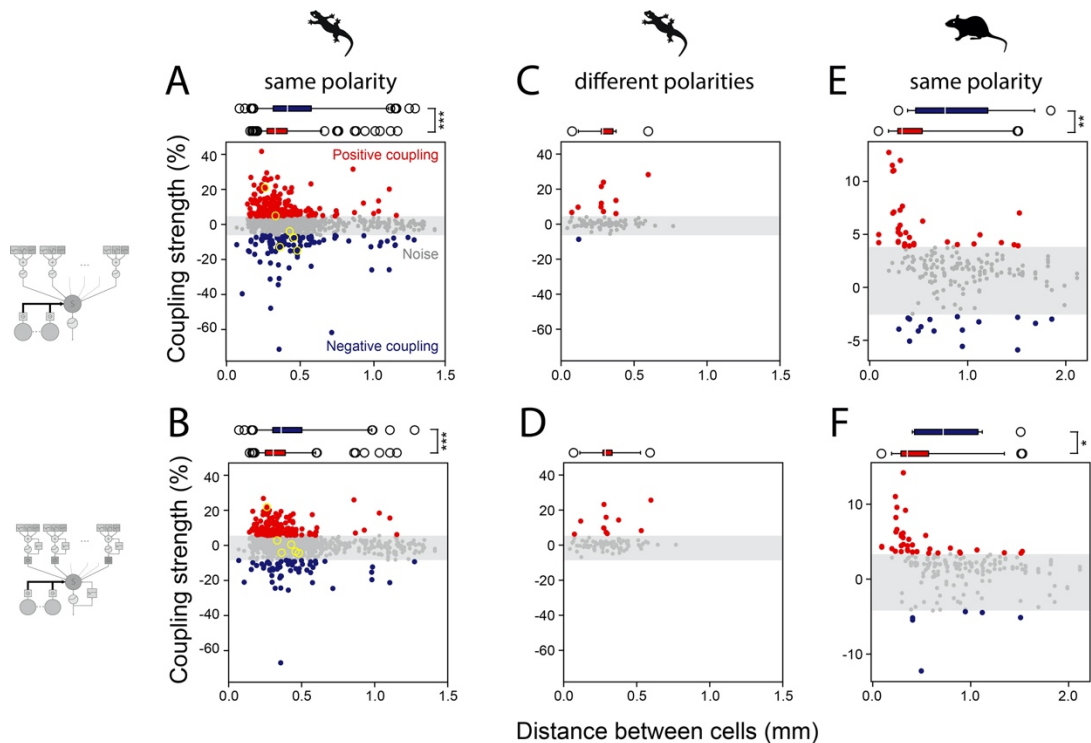


**Figure 2.5** Positive couplings occur among more proximal cells than negative. Coupling strength parameter for each coupled pair of cells are plotted as a function of distance between them for LNSCN model (A, C, E) and for LNFDSCNF model (B, D, F). A, B: For salamander cells of the same polarity mean distance of positively coupled cells (red, A: N=211, B: N=154) is smaller than of negatively coupled cells (blue, A: N=98, B: N=64) (A:  $0.31 \pm 0.14$ mm versus  $0.40 \pm 0.26$ mm,  $p < 0.001$ ; B:  $0.31 \pm 0.14$ mm versus  $0.36 \pm 0.20$ mm;  $p < 0.001$ ; median  $\pm$  interquartile range (box plot), rank-sum test). Parameters for the example cells from Figure 2.1C are in yellow circles. C, D: Salamander cells of different response polarity exhibit mostly (one outlier) positive coupling (C: N=10,  $0.28 \pm 0.08$ mm; D: N=11,  $0.29 \pm 0.06$ mm). E, F: Mouse cells of the same response polarity also show positive couplings (E: N=33, F: N=37) on a shorter distance than negative (E: N=16, F: N=6) (E:  $0.33 \pm 0.25$ mm versus  $0.78 \pm 0.74$ mm,  $p = 0.002$ ; F:  $0.35 \pm 0.28$ mm versus  $0.72 \pm 0.65$ mm,  $p = 0.02$ ). Grey shading indicates excluded parameters within the noise level (see Materials and Methods).

For the cells with the same response polarities, we found both positive and negative couplings (Figure 2.5). We have calculated distances between the receptive field centers of the cells (see Materials and Methods, “Modeling datasets”) and compared them for different coupling polarities. The diameter of the RGC dendritic field is around 0.3 mm (Völgyi et al., 2009; A. J. Zhang & Wu, 2010). We observed positive couplings for the cells at similar distances

( $0.31\pm 0.14\text{mm}$  for salamander and  $0.33\pm 0.25\text{mm}$  for mouse; median $\pm$ interquartile range) indicating their direct connections by gap junctions. Negative couplings occurred at a distance exceeding dendritic tree reach ( $0.40\pm 0.26\text{mm}$  for salamander and  $0.78\pm 0.74\text{mm}$  for mouse) supporting the suggestion that intermediary amacrine cells have to be involved to produce such an inhibitory effect. Our model also found predominantly positive couplings between salamander cells of opposing response polarities (distance of  $0.28\pm 0.08\text{mm}$ ), which is consistent with a recent study (Cooler & Schwartz, 2020).

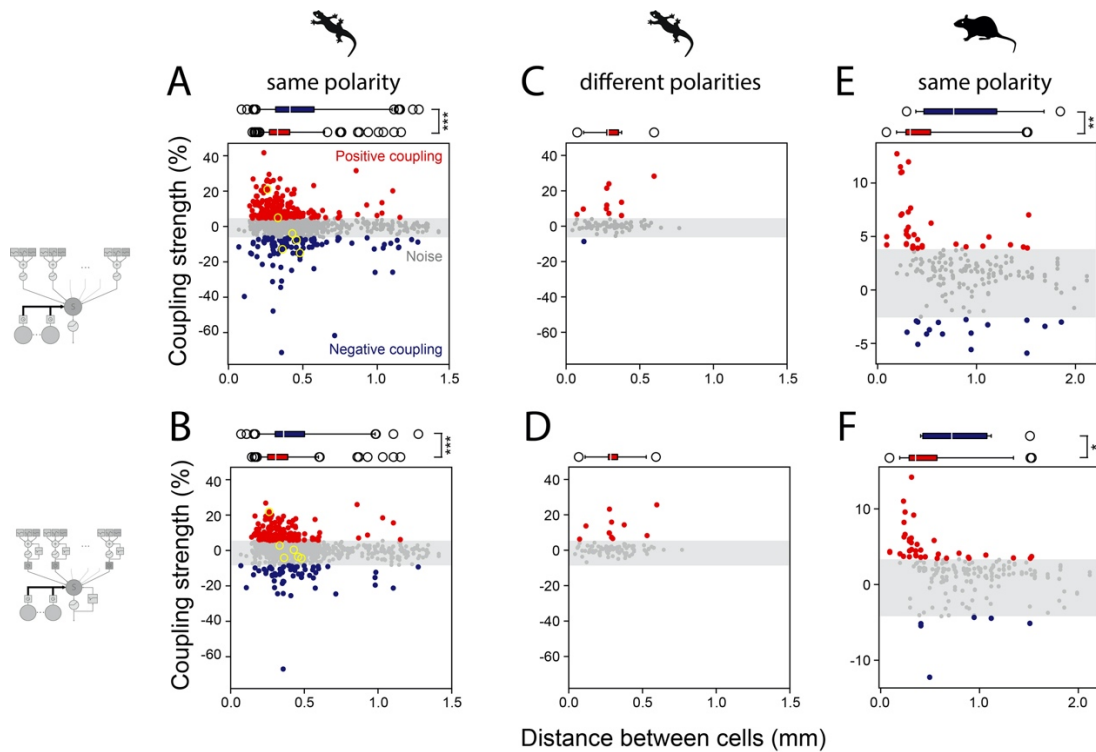


**Figure 2.6** Latency of positive couplings is faster than of negative. Latency (delay) parameter for each coupled pair of cells (same N as in Figure 2.5, red and blue – positive and negative couplings strength) are plotted as a function of distance between them for LNSCN model (A, C, E) and for LNFDSCNF model (B, D, F). A, B: For salamander cells of the same polarity positive couplings occurred faster than negative (A  $3.5\pm 3.6\text{ms}$  versus  $4.6\pm 4.0\text{ms}$ ;  $p<0.001$ ; B:  $2.3\pm 4.7\text{ms}$  versus  $4.7\pm 5.2\text{ms}$ ;  $p<0.001$ ; median $\pm$ interquartile range (box plot), rank-sum test). Parameters for the example cells from Figure 2.1C are in yellow circles. C, D: Delays for salamander cells of different response polarity (C:  $4.2\pm 1.5\text{ms}$ ; D:  $3.8\pm 6.5\text{ms}$ ). E, F: Mouse cells of the same response polarity show much longer delays for negative couplings (E:  $0.0\pm 0.0\text{ms}$  versus  $21.9\pm 13.8\text{ms}$ ;  $p<0.001$ ; F:  $0.00\pm 0.04\text{ms}$  versus  $19.1\pm 7.7\text{ms}$ ;  $p<0.001$ ). Grey dot are excluded parameters within the noise level (see Materials and Methods).

Importantly, signal delays between positively coupled cells were shorter than those of negatively coupled pairs (Figure 2.6;  $3.5\pm 3.6\text{ms}$  versus  $4.6\pm 4.0\text{ms}$ ,  $p<0.0001$  for salamander and  $0.0\pm 0.0\text{ms}$  versus  $21.9\pm 13.8\text{ms}$ ,  $p<0.001$  for

mouse). This further supports biological relevance of the model, confirming that inhibitory signals mediated by amacrine cells require more time to influence connected RGCs. Longer distances and delays between negatively coupled mouse RGCs indicate a possible signal transition through a chain of multiple amacrine cells, while smaller differences in salamander RGCs suggest a single amacrine transition.

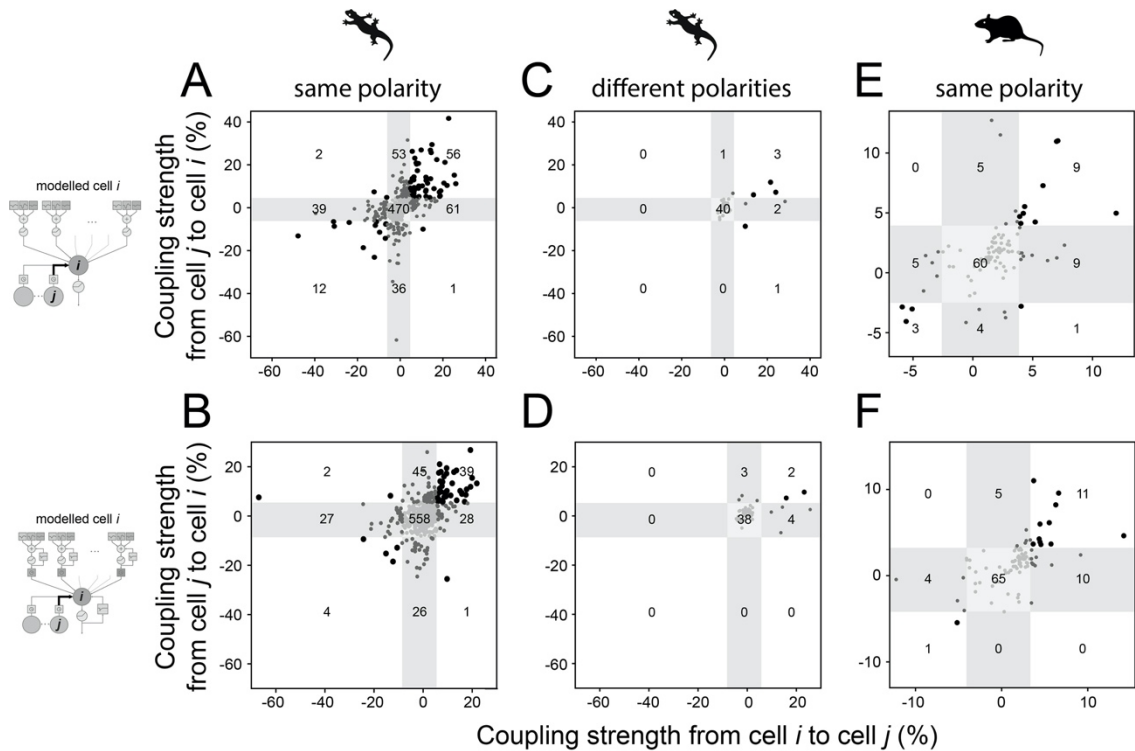


**Figure 2.7** Comparison of couplings bidirectionality. Coupling strength parameter in one direction (from cell  $j$  to cell  $i$ ) is plotted against opposite direction (from cell  $i$  to cell  $j$ ). Figure panels correspond to the same cell configurations as in Figures 2.5 and 2.6 (A,C,E – reduced coupled model, B,D,F – full coupled model). Black dots – coupling strength is above noise level in both directions, dark grey – only in one direction, light grey – both are below noise level. In both, salamander and mouse, coupling is either direction had the same sign (both positive or both negative) more frequently than expected ( $p < 0.001$  in all cases,  $\chi^2$ -test with  $df=4$ ).

For any given coupled cell pair, we analyzed coupling parameters for two coupling directions: when cell  $i$  is a target cell with cell  $j$  being a coupled neighbor, and, the opposite, when target is cell  $j$  and cell  $i$  is coupled as a neighbor (Figure 2.7). Observing a bidirectionality of the couplings, we saw that couplings largely have the same sign in both directions. It also indicates that a single cell can be part of multiple feedback pathways influencing many neighboring cells at the same time.

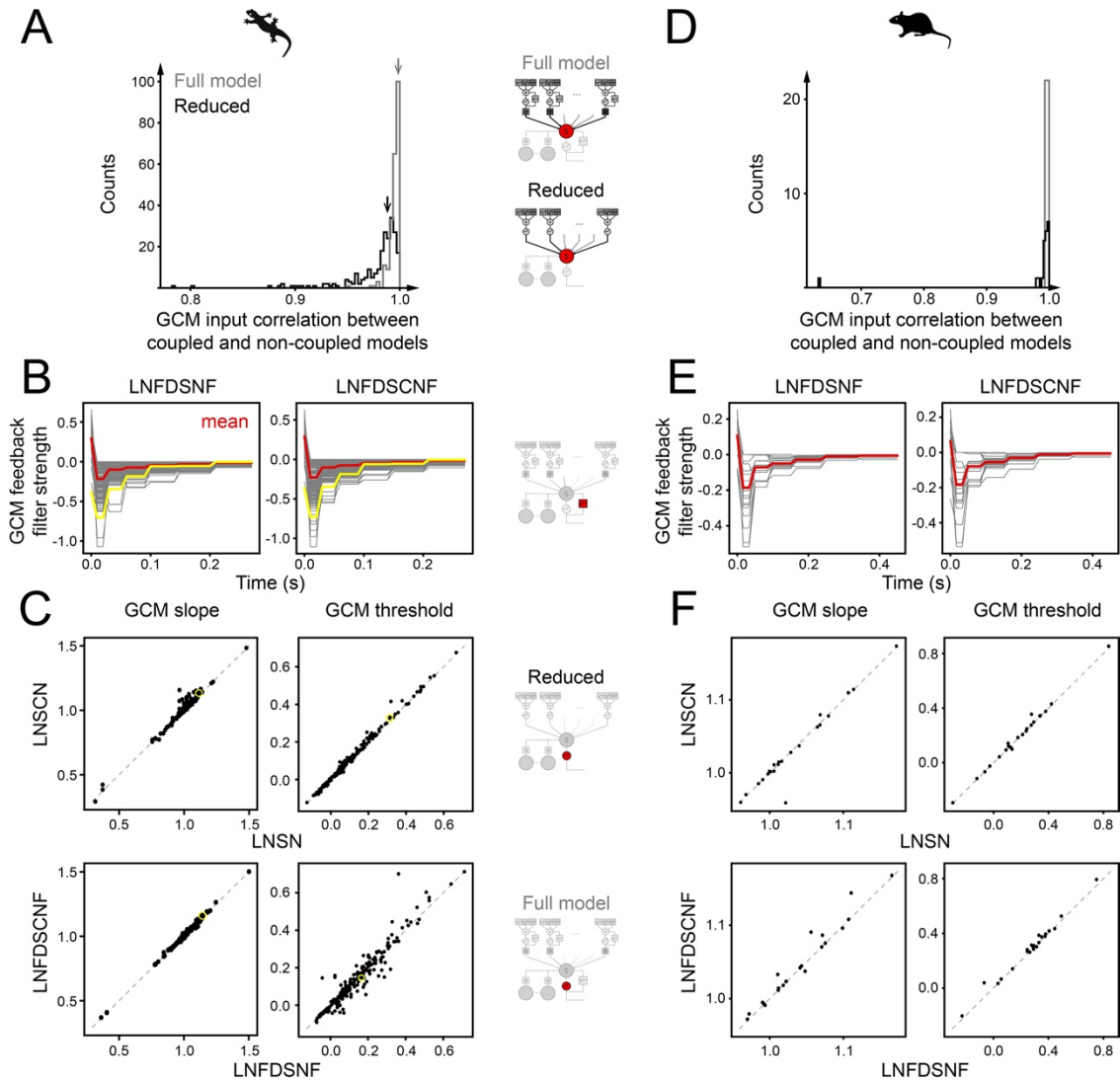


**Figure 2.8** Ganglion cell module processing is not influenced by couplings. A: Inputs to the GCM had very high correlation between coupled and non-coupled models for all salamander RGCs (black – reduced models,  $0.987 \pm 0.020$ , median  $\pm$  interquartile range; grey – full models,  $0.996 \pm 0.005$ ; see Materials and Methods). Arrow indicate example cell #25 from figure 2.1C. B: GCM feedback filters had the same dynamical range (red - mean, yellow - filter of the example cell #25). C: For both, full and reduced, models, GCM nonlinearity parameters were highly correlated (slope – Pearson’s  $R=0.979$  and  $0.997$  for reduced and full model, respectively; threshold –  $R=0.955$  and  $0.997$ ; see Materials and Methods Eq.(S6’)). Data point in yellow circle – example cell #25. D,E,F Corresponding panels for mouse RGCs (D:  $0.994 \pm 0.005$  and  $0.998 \pm 0.003$  for reduced and full models, respectively; F:  $R=0.967$  and  $0.978$  for slope in reduced and full models,  $R=0.991$  and  $0.996$  for threshold).

We have as well investigated whether addition of couplings had any effect on the processing characteristics of the ganglion cell module (Figure 2.8). But we did not find any significant differences neither between GCM inputs, nor between GCM output feedback and nonlinearity. This indicates that couplings do not influence RGC feature selectivity. On the other hand, suppression of the false

positive responses mediated by reciprocal inhibition from neighboring cells suggests that surrounding cells can participate in the ganglion cell output gain control.

To summarize, our model predicts a faster excitation between proximal RGCs and a slower inhibition between distal RGCs. The results are consistent with previous research of the gap-junctional couplings between RGCs. Novel prediction indicates that not only ON, but also OFF RGCs can exert inhibitory effect on each other.

### 2.2.3 RGCs cross-talk upon optic nerve stimulation

Given the modeling results, we examined the possibility of RGCs to indirectly inhibit each other experimentally. We utilized optic nerve stimulation to drive strong activation of as many ganglion cells as possible (Figure 2.9A). For this experiment, retinas were isolated with the intact optic nerve attached. Electrode stimulation was applied to the optic nerve in the dark, while the activity of the RGCs was monitored with the micro-electrode array (see Material and Methods, “Electrophysiology”). Electrical stimulation can elicit spikes that travel antidromically through the axons of the RGCs to the cell soma. Resulting simultaneous spiking of many RGCs is expected to strongly activate the recurrent signaling pathway indicated by the model analysis.

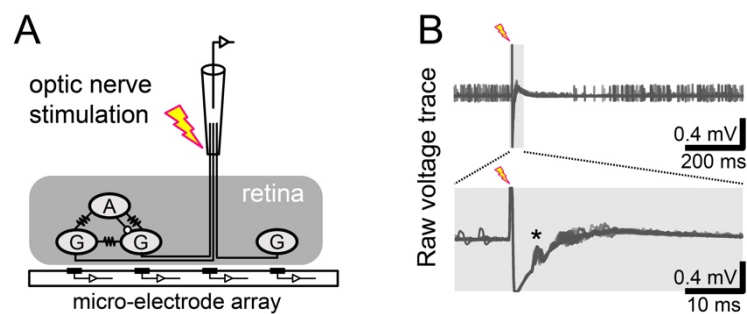


**Figure 2.9** Optic nerve stimulation experimental scheme. A: Retinas isolated with intact optic nerve is stimulated electrically (lightning) with the electrode, while activity of RGCs is recorded with micro-electrode array allowing to detect their cross-talk upon simultaneous activation (A – amacrine cell, G – ganglion cell). B: Raw voltage traces from the micro-electrode array overlaid for multiple trials by matching the time of electrical stimulation. Antidromic spike evoked by nerve stimulation is marked with an asterisk (\*).

In the dark, RGCs exhibit spontaneous spiking that we will call here a baseline activity. Stimulation of the optic nerve evoked antidromic spikes in many RGCs in both salamander and mouse retinas (Figure 2.10A, C). It also perturbed the baseline activity within tens to hundreds of milliseconds after the stimulation. Interestingly, such perturbation could be seen even in cells that did not show antidromic spikes (e.g. Figure 2.10B).

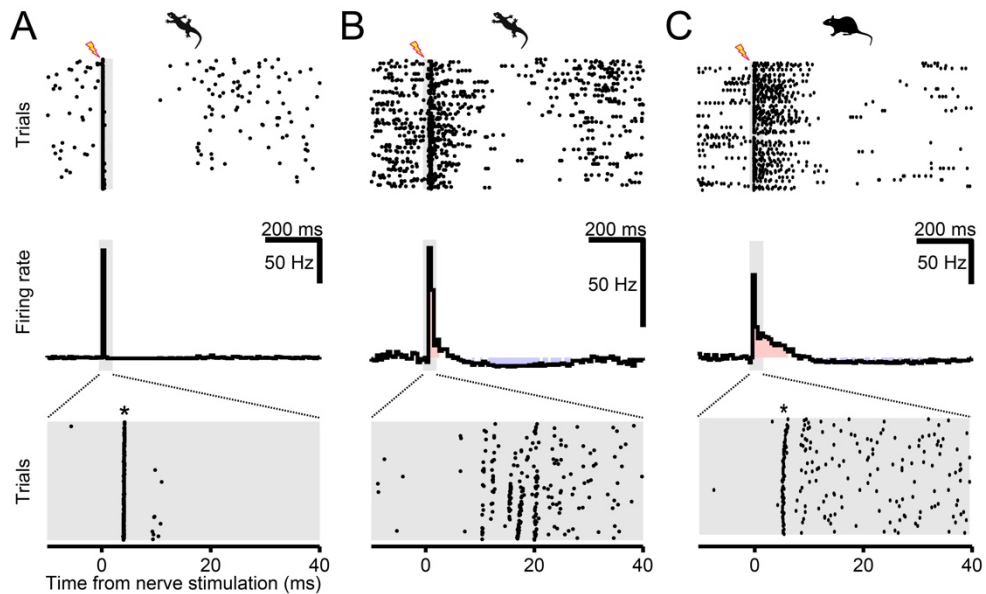


**Figure 2.10** Optic nerve stimulation allows to detect RGC cross-talk. **A:** Antidromic spikes in salamander cell upon electrical stimulus (lightning). Top: Raster graph over multiple trials. Middle: peri-stimulus time histograms (PSTH). Bottom: Magnified grey area from the PSTH showing antidromic spike (asterisk \*) 5 ms after the stimulation. **B:** Example salamander cell without antidromic spike exhibit enhanced activity within tens of milliseconds and suppressed activity within hundreds of milliseconds (significant time in red and blue shading, respectively). **C:** Example mouse cells with antidromic spike and enhanced activity.

To quantify perturbations caused by the optic nerve stimulation, we defined times where significant increase or decrease was observed relative to the baseline activity (Figure 2.11). To allow the comparison, only cells with a baseline firing rate  $>1\text{Hz}$  were analyzed. Bootstrap method with resampling over trials was used to identify the significance (see Materials and Methods). We did observe antidromic spikes in approximately one third of the RGCs (salamander - 75 out of 193 cells, mouse - 41 out of 132 cells, Figure 2.11A). A period of enhanced firing was frequently observed regardless of the antidromic spike presence (59

salamander and 20 mouse RGCs). Such positive activation lasted for tens of milliseconds after optic nerve stimulation.

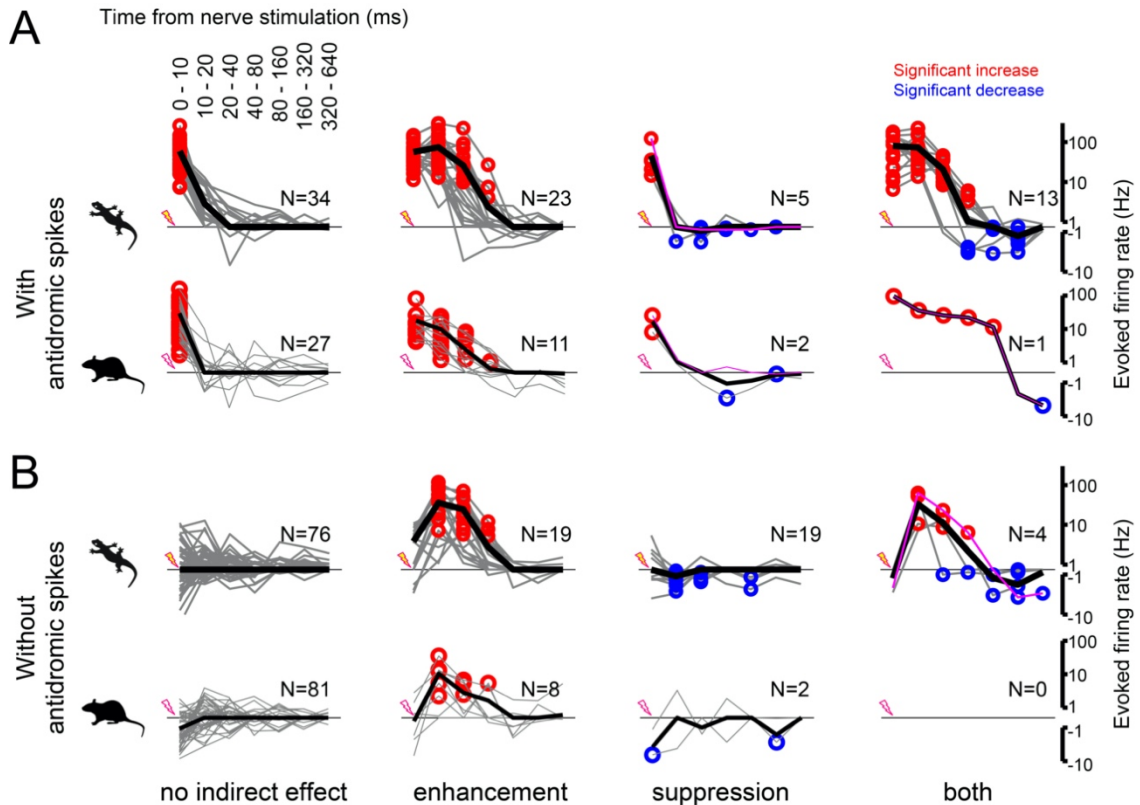


**Figure 2.11** Enhanced and suppressed activity is observed upon optic nerve stimulation in both, mouse and salamander, cells regardless of antidromic spike presence. A: PSTHs over wearying length time bins after stimulation (lightning) with significant increase and decrease of activity (red and blue circles, respectively) relative to the baseline. First and second row show the data for salamander and mouse cells, respectively. The columns separate groups of cells without indirect effect of the electrical stimulation, with enhancement, with suppression and with both indirect effects. Each grey line represents an average trace for a single cell, while black line is an average of a given group of cells. B: Corresponding PSTHs as in A for the cells that did not show antidromic spike.

Considering that RGC do not make any chemical synapses within the retina, enhanced firing has to be mediated by gap-junctional connections between RGCs or through a network of amacrine cells as described previously (Bloomfield & Völgyi, 2009; Brivanlou, Warland, & Meister, 1998a). We have also observed a suppression of the activity in cells with and without antidromic spikes (Figure 2.11A, B, 3<sup>rd</sup> and 4<sup>th</sup> columns). Such cells were less frequent (41 salamander and 5 mouse) and the suppressive affect was more spread in time, up to hundreds of milliseconds. Given that gap junctions are sign-conserving synapses and the only

possible inhibitory cell that can be excited by RGC is amacrine, the inhibition from one RGC to the other can be transferred indirectly through the amacrine cell. Together, results of the experiment confirm modeling predictions that RGCs can spread both positive and negative signals through the inner retina.

## 2.2.4 Amacrine cells and gap junctions are involved in RGC cross-talk

How can RGCs influence each other? As suggested by the previous studies, RGCs can send their signals to amacrine cells, which may in turn excite or inhibit other RGCs by electrical or chemical synapses, respectively (Bloomfield & Völgyi, 2009; Kenyon & Marshak, 1998; Völgyi et al., 2009). Our modeling and experimental results both confirm this suggestion.

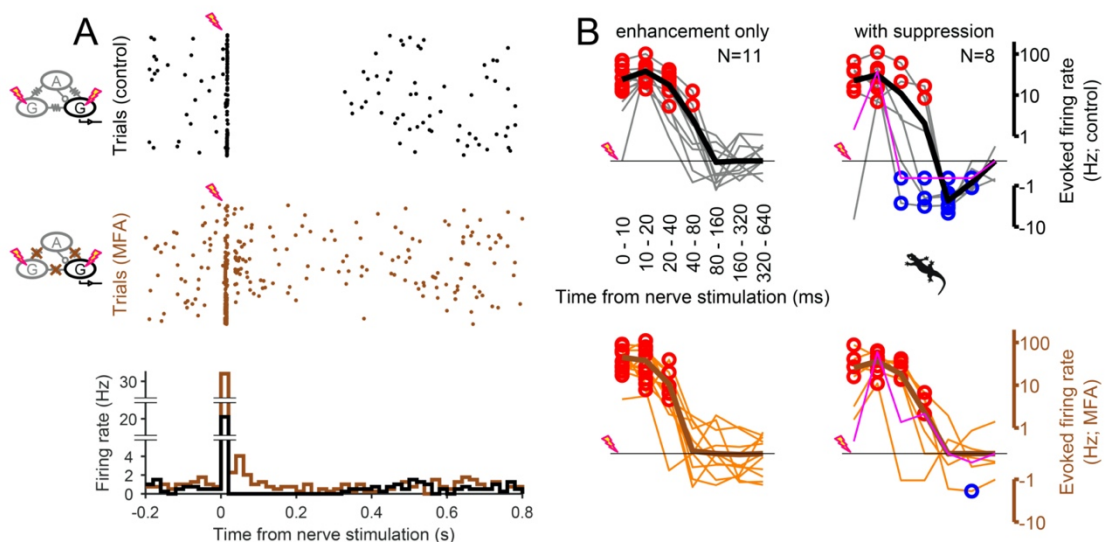


**Figure 2.12** Electrical synaptic transmission is required for negative feedback between RGCs. A: Raster graphs and PSTH of an example cell responding to the optic nerve stimulation before (top, black) and after (middle, brown) application of gap junction blocker (100  $\mu$ M meclofenamic acid, MFA). The suppressive effect was eliminated after MFA application. B: Population analysis analogous to Figure 2.11. The magenta trace is of an example cell in A. Enhancive effect remained (11 out of 11 RGCs), while suppression was abolished (7 out of 8 RGCs,  $p=0.036$ , Fisher's exact test) after MFA application (bottom, orange trances).

To directly test the involvement of gap junctions and amacrine cells, we performed pharmacological experiments. In the salamander retina we used 100 $\mu$ M meclofenamic acid to block gap junctional coupling between cells (Figure 2.12) (A. J. Zhang & Wu, 2009). This resulted in elimination of the delayed

suppressive effect upon optic nerve stimulation in the dark (7 out of 8 RGCs,  $p=0.036$ , Fisher's exact test, Figure 2.12B). But we could still observe fast enhancive effect in most of the RGCs (Figure 2.12B). This suggest that the optic nerve stimulation itself can affect the baseline activity in some RGCs for a short period of time, such as triggering a bursting (Figure 2.10C). Nevertheless, given experimental results confirm that electrical synapses are essential for the spread of inhibition between RGCs.

Second experiment was performed to test whether amacrine cells are necessary for the inhibitory effect. We have blocked inhibitory synaptic transmission from both  $\gamma$ -aminobutyric acid (GABA) and glycine, using a cocktail of 100  $\mu\text{M}$  picrotoxin and 1  $\mu\text{M}$  strychnine. These blockers combination effectively eliminated all inhibitory effects and did not influence enhancive effects (Figure 2.13). Taken together, pharmacological experiments confirm that gap junctions and amacrine cells are essential for inhibitory feedback between RGCs.

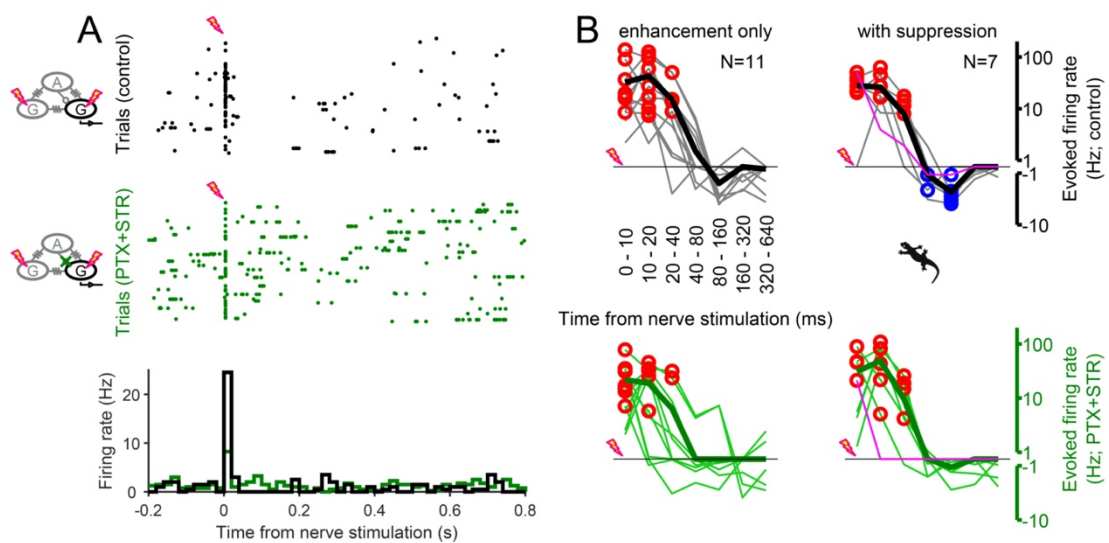


**Figure 2.13** Inhibitory synaptic transmission is required for negative feedback between RGCs. A: Raster graphs and PSTH of an example cell responding to the optic nerve stimulation before (top, black) and after (middle, green) application of inhibitory synaptic transmission blockers (100  $\mu\text{M}$  picrotoxin + 1  $\mu\text{M}$  strychnine; PTX+STR). The suppressive effect was eliminated after blockers application. B: Population analysis analogous to Figure 2.11. The magenta trace is of an example cell in A. Enhancive effect remained (11 out of 11 RGCs), while suppression was abolished (7 out of 7 RGCs,  $p=0.008$ , Fisher's exact test) after blockers application (bottom, green trances).

### **2.2.5 RGC visual response gain is modulated by negative feedback signaling**

Optic nerve stimulation experiments confirmed that negative feedback circuit between RGCs is physiologically functional. Meanwhile, we also want to know how it influences RGC visual responses. Our models predicted that inhibition from neighbors may influence visual response gain (Figure 2.4B). To test this hypothesis, we have performed experiments with simultaneous electric and visual stimulation of the retina (see Materials and Methods). We used full-field white noise visual stimuli instead of spatially structured stimulation due to the distortion of the image coming from the glass electrode that was used to stimulate the optic nerve. To evaluate visual response properties, we have estimated linear filters and nonlinearity gain functions for each RGC using reverse-correlation method (see Introduction) and compared them at different time points relative to the electrical stimulation (Figure 2.14A). Linear filter evaluates feature selectivity of the cell and it was characterized by the ON-OFF index (Eq.(6) in Materials and Methods) which compares the difference between peak and valley values of the filter normalized by their sum (Figure 2.14C). The gain of the cell is expressed by the nonlinearity of its response. The characteristic upper and lower bounds (Figure 2.14D) were calculated by fitting sigmoidal function to the static nonlinearity from the reverse-correlation method (Eq.(7) in Materials and Methods). ON-OFF indexes and upper and lower bounds were compared for the times where suppressed or enhanced firing was observed after the nerve shock relative to the baseline responses to the visual stimulus (Figure 2.14 for salamander and Figure 2.15 for mouse).

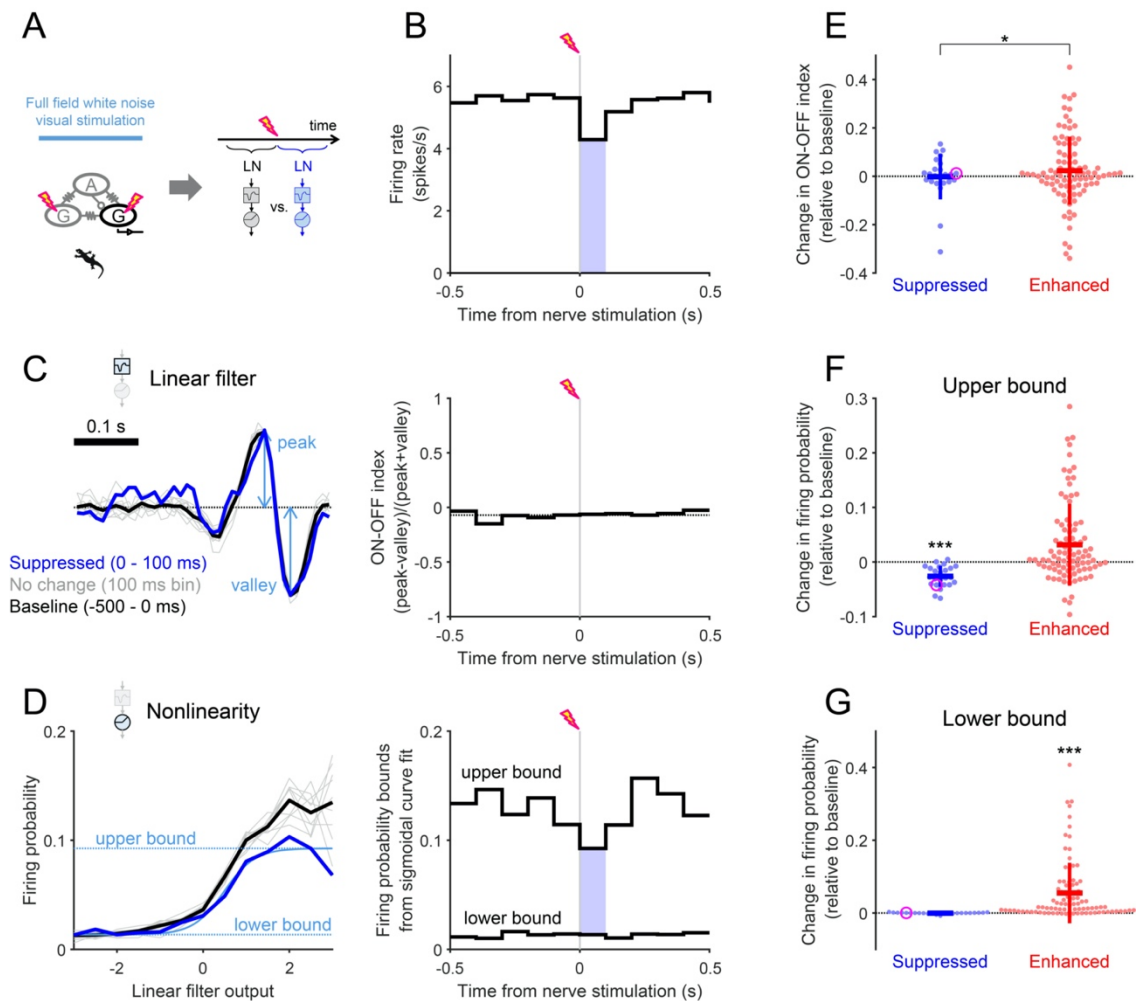


**Figure 2.14** Visual response gain is modulated by the negative feedback in salamander retina. A: Schematic representation of the experiment with simultaneous visual stimulation and optic nerve shock. Linear filter and nonlinearity gain functions are used to assess RGC visual feature selectivity and response gain, respectively. B: PSTH of the example RGC during the visual stimulation, centered at the optic nerve stimulation time. Blue shading marks time bin where significant suppression of the activity relative to the baseline was observed. C: (Left) Example linear filter (STA, reverse-correlation method) calculated at different time bins: blue – 100 ms bin with suppressed activity, black – baseline 500 ms before the nerve shock, grey – 100 ms bins after nerve shock without suppressed activity. (Right) ON-OFF indexes calculated from the linear filters of the corresponding time bins (Eq.(6) in Materials and Methods). D: (Left) Respective nonlinearities calculated with reverse-correlation method using linear filters in C. Upper and lower bounds of the fitted sigmoidal function (Eq.(7) in Materials and Methods) are shown only for the time bin with suppressed activity. (Right) Dynamic change of the nonlinearity function bounds over time of the example RGC. E: ON-OFF index changes during the time with suppressed and enhanced activity relative to the baseline for the population of salamander RGCs (blue – suppression,  $N=25$ ; red – enhancement,  $N=94$ ; magenta – example RGC in A). Mean and standard deviation are shown as vertical and horizontal lines, respectively. Stronger modulation of the feature selectivity was observed at the periods of enhanced activity ( $p=0.03$ , F-test). No significant changes relative to baseline were detected ( $p>0.3$  for both, enhanced and suppressed cases, sign-test) due to modulation taking either polarity. F, G: Analogous to E population results for the changes in response gain function. Within suppressed firing time, upper bounds (F) were significantly decreased (blue,  $p<0.001$ , sign-test), while lower bounds (G) remained unchanged ( $p>0.5$ ). For the enhanced firing times, lower bounds (G) were significantly increased (red,  $p<0.001$ ), while upper bound (F) were considered not affected ( $p=0.08$ ).

Feature selectivity of the RGCs did not change during the period of suppressed firing upon nerve stimulation, as can be seen from largely unchanged linear filter shape and ON-OFF indexes (Figure 2.14-15 C, E). On the other hand, more variability was observed in the linear filter profile during the periods of enhanced firing and the variation of ON-OFF indexes was significantly higher than during suppressed firing times ( $p=0.03$ , F-test; Figure 2.14E and Figure 2.15C, E). This means that positive feedback has more effect on feature selectivity than negative feedback.

Static nonlinearity gain function was significantly changed for periods of suppressed and enhanced firing after the nerve shock (Figure 2.14-15 D, F, G). First, enhanced firing times were characterized by the up-regulation of the gain. In particular, in salamander RGCs, a significant increase of the lower bound of spike probability was observed ( $p<0.001$ , sign-test; Figure 2.14G). Population of mouse RGCs was too small to see the trend, but examples of up-regulated gains were present (Figure 2.15D, G). Second, suppressed firing times showed a down-regulation of the gain function. Specifically, the upper bound of spike probability was significantly decreased in the population of salamander RGCs ( $p<0.001$ , Figure 2.14D, G). Again, the same trend was present in the small population of mouse RGCs (Figure 2.15D, F).

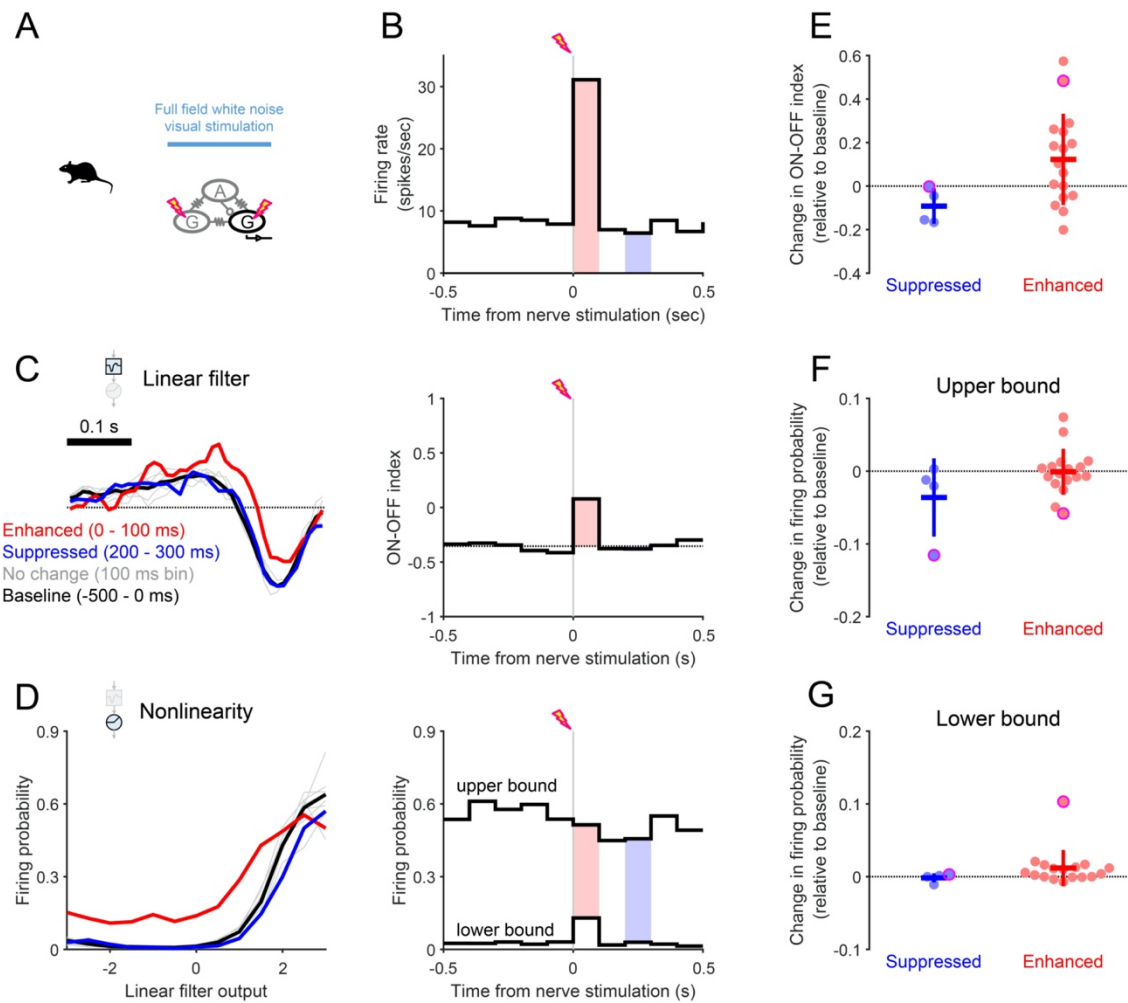


**Figure 2.15** Visual response properties are modulated by the negative feedback in mouse retina. Corresponding data as in Figure 2.14 for the mouse RGC. A: Circuit schematic. B: PSTH of the example RGC during the visual stimulation, centered at the optic nerve stimulation time. Blue and red shading marks time bins where significant suppression and enhancement, respectively, of the activity relative to the baseline was observed. C: (Left) Example linear filter (STA, reverse-correlation method) calculated at different time bins (red – 100 ms bin with enhanced activity). (Right) ON-OFF indexes calculated from the linear filters of the corresponding time bins (Eq.(6) in Materials and Methods). D: (Left) Respective nonlinearities calculated with reverse-correlation method using linear filters in B. (Right) Lower bound was increased during enhanced activity and upper bound was decreased during suppressed activity (Eq.(7) in Materials and Methods). E, F, G: Population summary of the visual response parameters change analogous to Figure 2.13 E,F,G, respectively (blue - suppression N=4; red – enhancement N=17).

Together, these results indicate that positive feedback between RGCs may dynamically change the feature selectivity of a given cell and increase its response probability while negative feedback circuitry with the inner retina can modulate the response gain of the RGC.

## **2.3 Discussion**

Modeling of neural circuits allows us to connect anatomical and physiological knowledge for a better functional understanding of brain computations at each level. Biologically relevant circuit models parametrize each neuron in the circuit according to its known or hypothetical function and connect these neurons together according to anatomical evidence. Results of such models, in turn, provide new predictions about given circuitry that can be tested experimentally (Real et al., 2017). We have utilized this approach to study interactions between retinal ganglion cells and inner retina. First, considering anatomical evidence of gap junctional connections between RGC and amacrine cells (Völgyi et al., 2009), we have extended a cascade modeling framework (Real et al., 2017) to include such couplings (Figure 2.1). Model parameter analyses showed that RGC of the same response polarity can inhibit each other's activity reciprocally over long distances and such inhibition is responsible for the response gain modulation (Figures 2.4-7). Then, testing the prediction experimentally, we have detected inhibition between RGCs and showed that these signals are spreading through gap junctions to amacrine cells that in turn inhibit the neighboring RGC (Figures 2.11-13). Lastly, our experiments also confirmed that inhibitory interactions do modulate the gain of RGC visual responses without affecting the feature selectivity as was suggested by the modeling results (Figures 2.14-15). The discovery of such gain control mechanism signifies the role of electrical synapses for RGC processing as well as highlights the power of a theory-driven approach to reveal new functional properties of the neural circuits.

### **2.3.1 Evolutionary conserved mechanism**

Gap junctional couplings is an evolutionarily conserved feature of the retina found in virtually all vertebrate species (Völgyi et al., 2013). Our modeling results were highly consistent in predicting positive and negative couplings between RGCs in salamander and mouse retinas. The special distribution of excitation between proximal cells and that of inhibition between distal cells are as well in accordance with previous research in salamander (Cocco, Leibler, &

Monasson, 2009) and primate retinas (Greschner et al., 2016; Pillow et al., 2008). Furthermore, the suppression of the activity upon optic nerve stimulation was also detected between the RGC of both salamander and mouse retinas under the *ex vivo* condition. A similar suppressive effect was shown in the catfish (Sakai & Naka, 1988, 1990) and primate (Gouras, 1969) retinas, though it was observed on a shorter time scale than in our study. Other concern was that antidromic spikes upon optic nerve stimulation may evoked cell-intrinsic effects, such as a bursting or prolonged hyperpolarization of the RGCs. But, on the one hand, it is overruled by our pharmacological experiments and, on the other hand, feedback circuitry involving signal transfer to amacrine cell via electrical synapses is supported by other modeling (Kenyon & Marshak, 1998) and spike-correlation analysis (Greschner et al., 2016) studies. Our data together with previous studies suggest that such inner retina feedback circuitry is also conserved across many species.

### **2.3.2 Dopamine regulation**

The stimulation of the optic nerve was first performed in the dark to drive ganglion cells activity without driving the upstream visual signaling cascade. We did observe simultaneous activation of many RGCs and got confirmation of the modeling predictions about RGCs cross-talk. One concern is that optic nerve stimulation may excite retinopetal projections (Koves & Csaki, 2016; Repérant et al., 2006). These are efferent axons projecting from the brain onto the retina that are suggested to activate dopaminergic amacrine cells in accordance with circadian rhythms (Gastinger, Tian, Horvath, & Marshak, 2006). As was discussed in the introduction, dopamine is vastly involved in the regulation of the gap junctional couplings in the outer half of the retina. We argue that dopamine effects have much slower kinetics compared to the one observed in this study (Pereda et al., 2013; S. Roy & Field, 2019; Witkovsky & Deary, 1991). Therefore, even if there is some activation of the retinopetal projections, their influence on the activity driven by the nerve shock should be negligible.

### 2.3.3 Future directions

The inhibitory feedback between ganglion cells was predicted by the model to be in the order of tens of millisecond, while experimental results showed activity suppression over hundreds of milliseconds. This discrepancy could have been caused by the overexcitation upon optic nerve stimulation when synchronous firing was observed over a large population of RGCs. On the other hand, stimulation of a single cell can be not sufficient to detect indirect negative coupling between RGCs of the same response polarity (Mastrorarde, 1983; Trong & Rieke, 2008), though some evidence was given in the catfish retina between cells of different response polarities (Sakai & Naka, 1988). It remains a further challenge to probe functionality of indirect negative feedback circuit under more physiological conditions, as well as to test remaining model prediction that such feedback is reciprocal for the cells of the same response polarity.

Regulation of neural output gain is an important functional mechanism found in many brain regions (Carandini & Heeger, 2012). Our modeling and experimental results both showed that negative feedback between RGCs is regulating their visual response gain in salamander and mouse retina. These results are consistent with previous research in the primate retina (Greschner et al., 2016). What could be a possible general function of such gain modulation in the inner retina? First, we have observed negative couplings even between cells that are widely separated from each other (~1mm). Such distance is out of the dendritic tree reach of the RGC (Völgyi et al., 2009; A. J. Zhang & Wu, 2010). Second, very slow timing (~100 ms) of such gain modulation exceeds other adaptation mechanisms in the inner retina. Specifically, faster adaptation was described at the synaptic terminals of the bipolar cell (Euler et al., 2014; Matthews, 1999) as well as in the negative feedback from amacrine cells to bipolar cells (Cun Jian Dong & Werblin, 1998; Nirenberg & Meister, 1997; Tachibana & Kaneko, 1988). As a result, negative RGC cross-talk cannot contribute to the precise timing of spikes that convey visual information. We suggest that observed negative feedback can be responsible for slow, wide-range equilibration of gain over

population of RGCs. The important next step is to dissect RGC type specificity of such connections.

Biologically driven cascade modeling does provide robust estimates of the RGC firing times, yet fails to reach the exact amplitude of the firing (Figure 2.4B). It suggests that other gain modulation mechanisms participate in the visual circuit processing. To uncover such mechanisms, we were also working on the novel experimental approach to record all retinal cells simultaneously. The progress and challenges of this side project are described in the last chapter.

## **2.4 Publication**

This work is under revision. Preprint published on BioRxiv:

Anastasiia Vlasiuk, Hiroki Asari, (2020). Feedback from retinal ganglion cells to the inner retina. *BioRxiv*. <https://doi.org/10.1101/2020.08.30.274514>

# 3 NERVE GROWTH FACTOR EFFECT ON DEVELOPING RETINA

## 3.1 Introduction

### 3.1.1 Retinal waves refine circuit formation

Development of the retina has been extensively studied. Common process involved in guiding retina maturation is a spontaneous bursting activity of retinal ganglion cells that occurs before visual circuitry is fully functional. It was first shown in neonatal rabbit retina back in the 70<sup>th</sup> (Masland, 1977). Later, *in vivo* recordings in fetal rat retina confirmed that such bursts are synchronous in the neighboring RGCs (Maffei & Galli-Resta, 1990). Shortly after, *in vitro* electrophysiological recordings of many RGCs in neonatal ferret confirmed that these bursts are spreading across the retina in unpredictable random directions as waves (Meister, Wong, Baylor, & Shatz, 1991). Retinal waves are crucial for the refinement of retinofugal projections from the retina to the superior colliculus, (Ackman, Burbridge, & Crair, 2012), dorsal lateral geniculate nucleus (Mooney, Penn, Gallego, & Shatz, 1996) and primary visual cortex (Colonnese & Khazipov, 2010). In the superior colliculus and dorsal lateral geniculate nucleus, RGC axonal terminals form retinotopic maps where spatial segregation of projections corresponds to the RGC locations in the retina. Such retinotopy is disrupted without synchronous bursting activity, retinal waves, during development (Constantine-Paton, Cline, & Debski, 1990; Kobayashi, Nakamura, & Yasuda, 1990; Simon, Prusky, O’Leary, & Constantine-Paton, 1992).

Retinal waves are present in mice starting from several days before birth and continuing for about 2 weeks before eye opening at postnatal day 14 (P14) (Mooney et al., 1996). At this time retinal cells finish to differentiate, migrate and form a laminar structure (Young, 1985). The time course of cell differentiation is different for each major cell type and is finishing earlier in the central retina and later at the periphery. Generally, at the time of birth of the mouse pup, horizontal

and retinal ganglion cells are already established, amacrine cells and cones are exiting neurogenesis while rods, bipolar and Müller glia cells are in the first half of their development. This means that connections between photoreceptors and ganglion cells at P0 are not yet established and the retina is largely irresponsive to light, with the exception of intrinsically-photosensitive RGCs (Sekaran et al., 2005). As circuitry develops, retinal waves are generated via different mechanisms in three stages. First, from embryonic day 17 (E17) to P1, they are mediated by gap junctional couplings between RGCs (Blankenship & Feller, 2010). Second stage is characterized by cholinergic waves lasting from P1 to P10 while in the last stage (P10-P14) the waves are driven by glutamatergic influence (Bansal et al., 2000; Maccione et al., 2014; Wong, Myhr, Miller, & Wong, 2000).

### **3.1.2 Microglia in the developing retina of a mouse**

Microglia, the resident immune cells in the central nervous system, actively participate in the neural circuits development, including retina (F. Li, Jiang, & Samuel, 2019; Silverman & Wong, 2018). They are present in the mouse retina starting from E11.5 and localize in the retinal synaptic layers upon their formation (Santos et al., 2008). The number of microglia cells is increasing postnatally up to P7, the most active circuit refinement time. These findings suggest that microglia may regulate synaptic pruning in the retina, much as it does in other brain regions (Paolicelli et al., 2011). Synaptic pruning by microglia was also shown to be guided by neuronal activity in RGC terminals in lateral geniculate nucleus (Schafer et al., 2012) and synapses in the visual cortex (Tremblay, Lowery, & Majewska, 2010). It is known that retinal cells are born in excess amount and are subject to subsequent programmed cell death (Young, 1984). Microglia-mediated phagocytosis was implicated in such natural reduction of RGCs (S. R. Anderson et al., 2019) and amacrine cells (Puñal et al., 2019). On the other hand, microglia supply neurotrophic factors supporting neural survival (Ferrer-Martín et al., 2015). Therefore, it is proposed that microglia can help shape the retinal circuitry by supporting both the maturation and removal of the early cells and synapses in an activity dependent manner.

In pathological conditions where inflammation process takes place, microglial activation can lead to opposing effects depending on the type of injury (Rashid, Akhtar-Schaefer, & Langmann, 2019). Anti-inflammatory cascade of reaction mediated by microglia upon acute injury results into neuroprotective effect that restores tissue homeostasis (Bellver-Landete et al., 2019). On the other hand, chronic activation of the microglia in neurodegenerative disorders has pro-inflammatory effect leading to neural cells apoptosis (Zhao et al., 2015). Thus, microglia are actively studied as a target for various therapies.

### **3.1.3 Aim of the experiments**

Nerve growth factor (NGF) is a neurotrophic factor that promotes growth, proliferation and survival of neurons (Levi-Montalcini, 1987). Big varieties of NGF actions are translated via different signaling pathways upon its binding to high-affinity tyrosine kinase receptor A (TrkA) and low affinity p75 neurotrophin receptor (Aloe, Rocco, Balzamino, & Micera, 2015; Huang & Reichardt, 2003; Reichardt, 2006). Since the discovery, a therapeutic potential of NGF is extensively studied, including vision impairment (Aloe et al., 2015). It was shown that RGCs are not able to regrow their axons upon optic nerve injury regardless of the increase in endogenous NGF presence (Mesentier-Louro et al., 2017). Though, application of exogenous NGF was able to reduce the loss of RGCs after optic nerve section (Carmignoto, Maffei, Candeo, Canella, & Comelli, 1989) and in glaucoma model (Colafrancesco et al., 2011; Lambiase et al., 2009) in adult rats. RGC survival was suggested to be mediated by inhibition of astrocyte activity in the optic nerve, which is responsible for secondary degeneration process (Guo et al., 2020). Exact molecular mechanisms, however, remain to be elucidated.

Recent evidence from Antonino Cattaneo and Silvia Marinelli labs has shown that exogenous NGF modulates microglial cells to steer microglia towards a neuroprotective and anti-inflammatory phenotype (Rizzi et al., 2018). Notably, in this study they observed that TrkA receptors are selectively expressed in the microglia of cortex and hippocampus and their activation by NGF increased the frequency and amplitude of miniature excitatory postsynaptic currents in

pyramidal neurons. This microglia-to-neuron communication was abolished by TrkA and microglia blockers, suggesting that NGF modulates glutamatergic neurotransmission by microglia cells (Marinelli, Basilico, Marrone, & Ragozzino, 2019). Based on these observations they hypothesized that NGF exerts neuroprotective effect in the retina through microglial cells. Their unpublished data on neonatal retinas reveal that (1) TrkA is expressed in retinal microglia but not in RGC and (2) NGF rescues RGC death in lesioned retinas in parallel to a modulation of microglia morphology.

As a part of Silvia Marinelli's investigations of NGF therapeutic capacity, we have studied the potential functional effects of NGF on neonatal retina electrophysiological properties. The main focus of the experiments was to test in the intact retinas whether (1) NGF can influence RGC spiking activity and (2) whether microglia take part in the process.

## **3.2 Materials and methods**

### **3.2.1 Electrophysiology**

Multi-electrode recordings of retinal waves were performed under the license 233/2017-PR from Italian Ministry of Health. In short, the retina of a mouse pup (*Mus Musculus*; C57BL/6J strain, P2-P3) was isolated and placed on a flat array of 120 extracellular electrodes (Multichannel Systems, 120MEA30/10iR-ITO) with the ganglion cell side down. The retina was superfused with oxygenated Ames's medium (Sigma-Aldrich, A1420; equilibrated with 95% O<sub>2</sub> and 5% CO<sub>2</sub> gas) at a flow rate of 2 ml/min at 37 °C. Before the recording the retina was left on the electrode array for at least 15 minutes to settle down. Signals from each electrode were sampled at 25 kHz for 70-150 minutes continuously (Multichannel Systems, MEA2100-System). Further offline processing with SpyKING CIRCUS extracted the spike trains for the individual ganglion cells (Yger et al., 2018).

In total, recordings were made from 28 retinæ, each with 30-126 ganglion cells. Of these, 10 retinæ were examined with the bath-application of the nerve-growth factor (NGF; 100 ng/ml) for 25-30 minutes in the middle of the recordings.

Six retinae were incubated with the microglia activation blocker (100 nM minocycline) for at least 1 hour and then tested with NGF for 30 minutes in the presence of the blocker throughout the recording (Plane, Shen, Pleasure, & Deng, 2010). Analogous experiments were performed for 4 retinae incubated with anti-TrkA antibody (1 mg/ml MNAC13) for at least 2.5 hours and tested with NGF for 30 minutes under constant flow of the antibody (Cattaneo et al., 1999). As a control condition, 8 retinae were recorded without NGF, minocycline, or MNAC13. NGF, minocycline and MNAC13 were provided by Silvia Marinelli and Antonino Cattaneo.

### **3.2.2 Data Analysis**

Electrophysiology data analysis was done in Matlab (Mathworks) and Python. For each recording, we first computed the time histogram of population firing rates (1 s bin width) and identified individual retinal waves by setting a threshold at 1 spike/s/cell. We then calculated (a) the inter-wave intervals between the peaks; and (b) the peak firing rate averaged over the cells involved in each retinal wave. For each recording condition, we compared these parameters across the following three epochs: 1) 20 minutes window just before the onset of the NGF bath-application, 2) the last 20 minutes of the NGF application period, and 3) 20 minutes window starting 10 minutes after the offset of the NGF application. For the control data sets, the corresponding three epochs (10-30, 40-60, and 70-90 minutes from the recording onset) were used. One-way analysis of variance (ANOVA) was used for a statistical test with the significance level of 0.05. No statistical method was used to predetermine the sample size.

## **3.3 Results**

### **3.3.1 Nerve growth factor facilitates retinal waves**

To investigate NGF action on premature retina, we performed *in vitro* electrophysiological recordings of the RGCs activity in the neonatal mouse (P2-P3) retina using a multi-electrode array. As described in the background, retinal circuitry of the newborn mice is incomplete and undergoes active development.

We have successfully observed the typical correlated bursting of RGCs, retinal waves (Figure 3.1A). The spatiotemporal properties of the waves were random, as expected, meaning that we could observe retinal waves traveling in different directions where a various number of RGCs was activated. NGF was added to the perfusion media in the middle of the experiment for 25-30 minutes with a following 1-hour wash-out time (see Materials and Methods, Figure 3.1B).

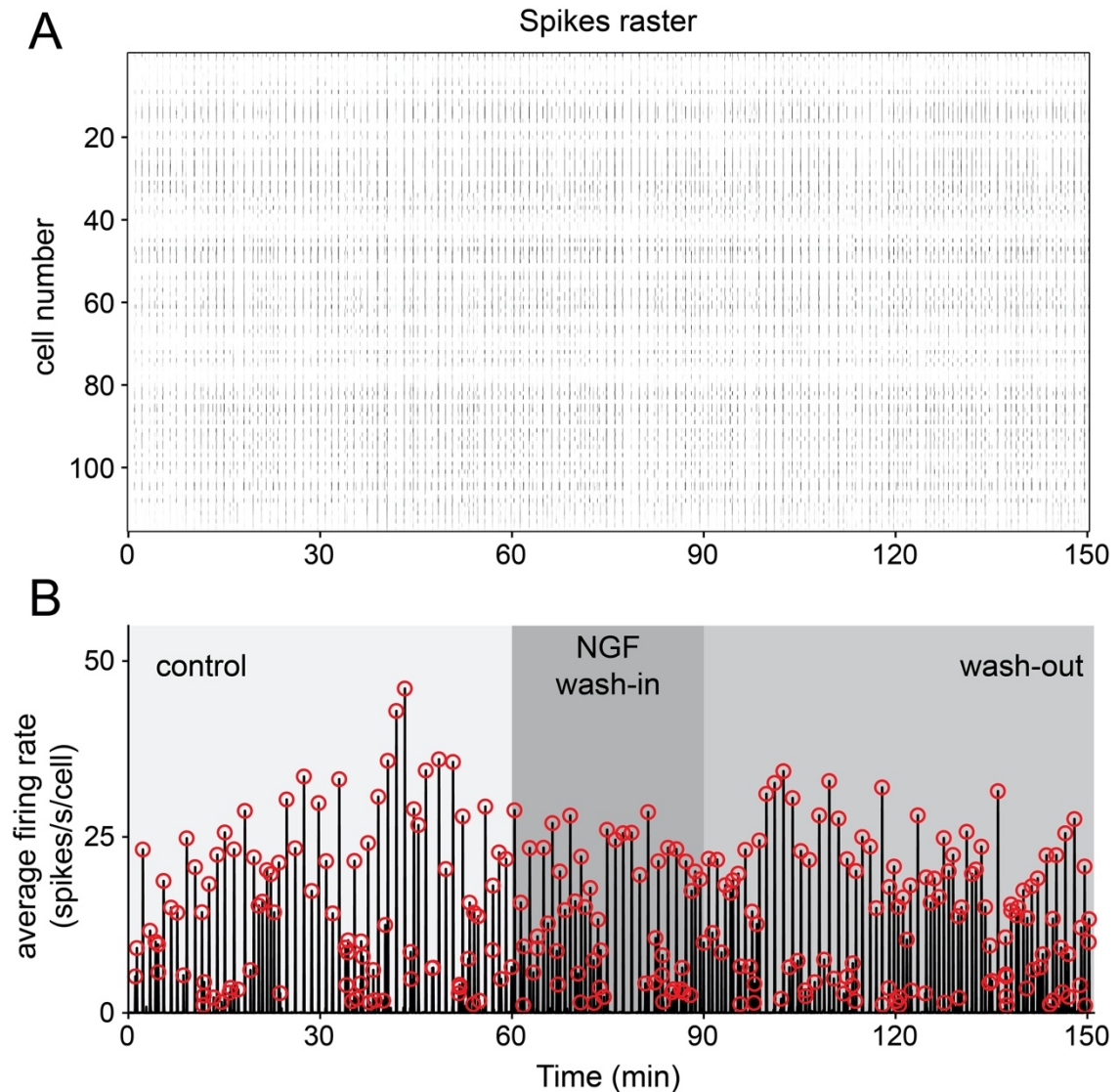


**Figure 3.1** Example recording of retinal waves with NGF application. A: Spike raster of 116 RGC activity (spike counts binned in 1 second time window) over 150 minutes of recording. Highly correlated activity was observed as expected. B: Average firing rate over all cells in A with retinal waves peaks marked in red circles. Waves were first observed in Ames's media for 60 minutes as a control, then NGF was added to the perfusion media for 40 minutes followed by 60 minutes of the NGF wash-out time.

We have compared inter-wave intervals and peak firing rates (red circles in Figure 3.1B) between retinal waves recorded before, during and after the NFG application. Retinal waves were defined as events with an average firing rate above the threshold of 1 spike per second per cell. For each condition, typical 20 minutes time window was selected to evaluate wave parameters (see Materials and Methods).

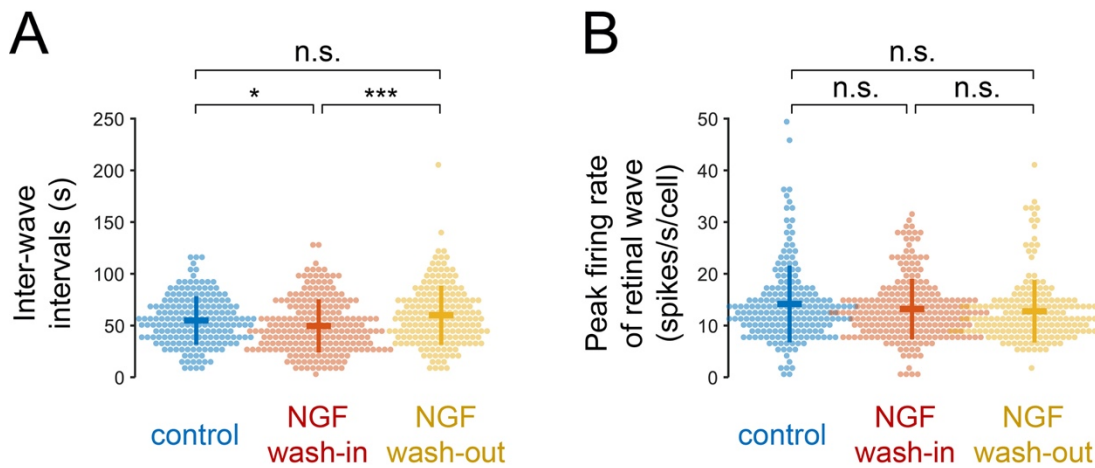


**Figure 3.2** NGF increases wave frequency without affecting peak firing rate. A: Inter-wave intervals before (N = 191 cells), during (N = 229 cells) and after (N = 187 cells) NGF application (54.9±23.4 s, 49.6±25.7 s, 60.0±28.7 s, respectively; mean ± standard deviation marked in bold horizontal and vertical lines, respectively; N = 10 retinae). B: Peak firing rate of the retinal waves for the same dataset as in A (in spikes/s/cell for the three condition: 14.2±7.4, 13.2±5.6, 12.8±6.1). Here and thereafter: (\*) - p<0.05, (\*\*) – p<0.01, (\*\*\*) – p<0.001, n.s. – not significant.

Retinal waves became more frequent upon addition of exogenous NGF as can be seen from the reduction of inter-wave intervals on the Figure 3.2A (54.9±23.4 s vs 49.6±25.7 s, mean ± standard deviation; p<0.05, one-way analysis of variance). It was followed by the decrease of the frequency during NGF wash-out time (49.6±25.7 s vs 60.0±28.7 s) which was not significantly different from the control condition. No variation in the inter-wave intervals was present in the control drug-free recording over 2.5 hours (data not shown). Looking at the Figure 3.1B, it may seem that the wave frequency is increasing due to the addition of “smaller” waves with less RGCs involved characterized by smaller peak firing rates. But, as you can see in the Figure 3.2B, no significant differences were found

between peak firing rates over distribution of retinal waves. These experiments demonstrate that NGF can facilitate retinal wave generation.

### 3.3.2 NGF acts through binding to TrkA receptor

Considering that NGF action requires binding to one of the two receptors, TrkA or p75, we have repeated the experiments in the constant presence of anti-TrkA antibody (1 mg/ml MNAC13) (Cattaneo et al., 1999). No significant changes were observed for both inter-wave interval and peak firing rate in the presence of NGF (Figure 3.3). Interestingly, waves became less frequent (inter-wave interval of  $75.4 \pm 25.4$  s vs  $60.2 \pm 30.6$  s,  $p < 0.01$ ) and the peak firing rate decreased (in spikes/s/cell:  $10.2 \pm 3.9$  vs  $8.1 \pm 2.5$ ,  $p < 0.001$ ) over the course of the recording. This indicates that anti-TrkA antibody is also blocking the effect of endogenous NGF. We can also notice that overall waves were more frequent with higher average firing rates in the control condition without anti-TrkA antibody (Figure 3.2); however, high inter-wave variability does not allow for comparison between the two conditions. To this point, we can claim that TrkA receptor is required for NGF action.

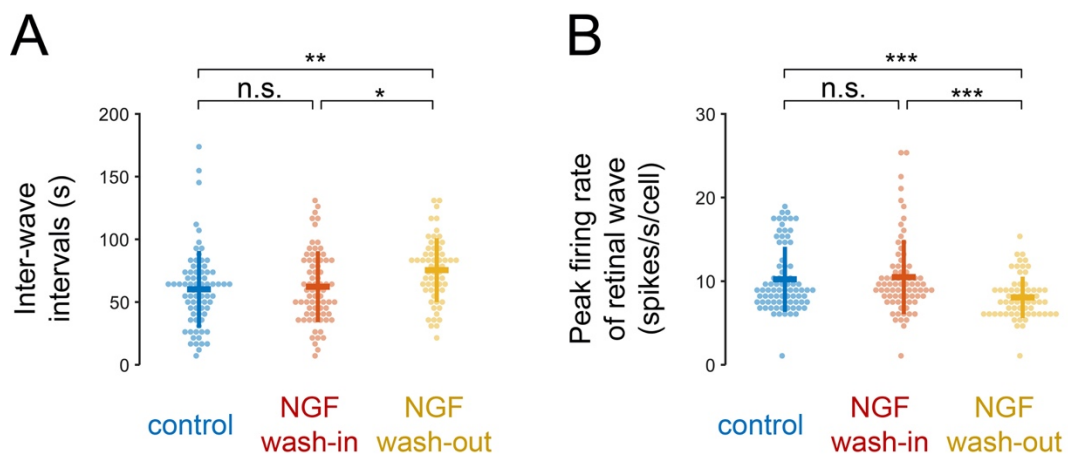


**Figure 3.3** Blocking TrkA receptor attenuates NGF effect. A: Inter-wave intervals in the continuous presence of anti-TrkA antibody (1 mg/ml MNAC13) before ( $N = 75$  cells), during ( $N = 73$  cells) and after ( $N = 60$  cells) NGF application ( $60.2 \pm 30.6$  s,  $62.3 \pm 28.3$  s,  $75.4 \pm 25.4$  s, respectively; mean  $\pm$  standard deviation marked in bold horizontal and vertical lines, respectively;  $N = 4$  retinæ). B: Peak firing rate of the retinal waves for the same dataset as in A (in spikes/s/cell for the three condition:  $10.2 \pm 3.9$ ,  $10.5 \pm 4.4$ ,  $8.1 \pm 2.5$ ).

### 3.3.3 Microglia effect on retinal waves

Downregulation of RGC activity was observed in the presence of a microglia activation blocker (100 nM minocycline) (Plane et al., 2010) regardless of the NGF addition to the media (Figure 3.4). Peak firing rate significantly dropped in the second part of the experiment when NGF was applied (Figure 3.4B, in spike/s/cell:  $8.6 \pm 2.0$  vs  $7.8 \pm 1.7$ ,  $p < 0.001$ ). Wave frequency decreased gradually from the beginning to the end of the experiment (Figure 3.4A, inter-wave intervals:  $57.5 \pm 29.2$  s vs  $75.0 \pm 44.8$  s,  $p < 0.01$ ). This does support the hypothesis that NGF wave facilitation is mediated by the TrkA selectively expressed by microglia. As well, it indicates the importance of microglia support of the immature retina.

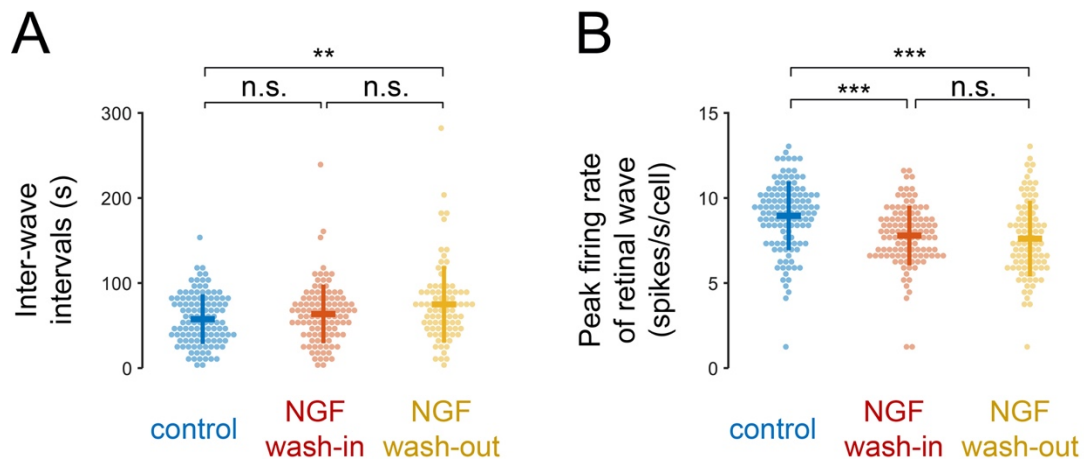


**Figure 3.4** Blocking microglial cells attenuates NGF effect. A: Inter-wave intervals in the continuous presence of microglia activation blocker (100 nM minocycline) before ( $N = 115$  cells), during ( $N = 106$  cells) and after ( $N = 85$  cells) NGF application ( $57.5 \pm 29.2$  s,  $63.6 \pm 34.4$  s,  $75.0 \pm 25.4$  s, respectively; mean  $\pm$  standard deviation marked in bold horizontal and vertical lines, respectively;  $N = 6$  retinæ). B: Peak firing rate of the retinal waves for the same dataset as in A (in spikes/s/cell for the three condition:  $8.6 \pm 2.0$ ,  $7.8 \pm 1.7$ ,  $7.6 \pm 2.2$ ).

## 3.4 Discussion

We have investigated the effects of exogenous NGF on the activity of RGCs in the immature retina. The typical developmental retinal waves were compared with and without NGF bath-application. Retinal waves were significantly more frequent in the presence of NGF with a stable bursting intensity of RGCs lasting even after NGF was removed (Figure 3.2). Blocking high-affinity

NGF receptor TrkA abolished NGF-mediated wave facilitation effect, and RGC bursting and wave frequency decreased by the end of the recording (Figure 3.3). Inhibiting microglia had a similar, but more pronounced effect on retinal waves downregulation (Figure 3.4). We suggest that exogenous NGF exerts neurotrophic action on retinal waves through its binding to TrkA receptor on microglial cells. In addition, our data clearly suggest that both microglia and TrkA-receptor activation by endogenous NGF play a key role in maturation of retinal circuitry.

Microglia actively participate in the retinal circuit development, as described in the background section. Minocycline is known for its anti-inflammatory properties that include inhibition of microglia and attenuation of apoptosis (Plane et al., 2010). Considering that some RGCs undergo programmed cell death in the immature retina with microglia involvement, minocycline may attenuate this process. In this case more RGCs should survive and we would not expect to see retinal wave downregulation over time *in vitro* (Figure 3.4). This signify the importance of neurotrophic rather than phagocytic effects of the microglia on the immature retina (Ferrer-Martín et al., 2015).

# 4 SIMULTANEOUS RECORDING OF ALL RETINAL CELL LAYERS

To fill the gaps in our understanding of how retina is processing visual information, we decided to establish the technique to monitor signal flow through all retinal layers. Great varieties of ganglion cell properties were described using micro-electrode recordings (Meister et al., 1994), while interactions between different retinal cell types were effectively probed with dual-patch recordings (Stuart, Dodt, & Sakmann, 1993). The development of calcium indicators allowed to investigate the activity of many more neurons at the same time (Baden et al., 2016; Grienberger & Konnerth, 2012; Stringer et al., 2018). Retinal circuits are densely packed with neurons of different types that provide us with a unique capacity to observe timely activation of each cell in the visual signal processing path. Establishing a signal flow recording technique would eliminate the need to infer upstream processing steps in understanding RGC function. This chapter is a report of the side project with current progress and challenges in setting up retinal cross-section recording.

## 4.1 Materials and methods

### 4.1.1 Viruses

Following adeno-associated viruses (AAVs) were made in the EMBL Rome Genetic and Viral Engineering Facility by James Sawitzke:

rAAV7m8::CAG-jGCaMP7f ( $6.0 \times 10^{11}$  vg/ml)

rAAV7m8::CAG-jGCaMP6s ( $3.1 \times 10^{12}$  vg/ml)

rAAV7m8::EF1 $\alpha$ -jGCaMP7f ( $2.3 \times 10^{12}$  vg/ml)

rAAV7m8::EF1 $\alpha$ -Cre ( $2.3 \times 10^{12}$  vg/ml)

rAAV7m8::CAG-FLEX-jGCaMP7f ( $1.7 \times 10^{13}$  vg/ml)

rAAV2(PHP.eB)::CAG-iCre ( $2.7 \times 10^{13}$  vg/ml)

The 7m8 variant of AAV2 is able to infect all retinal cells upon intravitreal injection (Dalkara et al., 2013).

### **4.1.2 Mouse lines**

Transgenic mice Ai95D were rederived from 3 males purchased from Jackson Laboratory (Ai95(RCL-GCaMP6f)-D, JAX 028865, The Jackson Laboratory) by Alessandra Pisaniello and mouse facility staff at EMBL, Rome. Frozen sperm of the Rax-Cre mice was purchased from Infrafrontier (C57BL/6-Tg(mRx-Cre)1Zkoz, EM:06880, EMMA mouse repository); *in vitro* fertilization was performed by Alessandra Pisaniello. Ai95D mice were crossed with Rax-Cre mice in house by Alessandra Pisaniello and mouse facility staff.

### **4.1.3 Intravitreal injection**

All the animal procedures were performed under the license 233/2017-PR from Italian Ministry of Health and in accordance with current EU directives. Wild-type (*Mus Musculus*; C57BL/6J strain) and transgenic mouse line Ai95D of either sex received bilateral intravitreal injections of different virus particles in the age of 4-5 weeks.

Mouse was anesthetized with isoflurane (4% for induction, 2% during the procedure; IsoFlo, Ecuphar Italia S.r.l.) and placed on the isothermal pad (37 °C). Glass capillary tip (50-70 µm) with a virus solution was placed into the vitreous space under stereo microscope (WPI); injection site was dried with tissue to ensure sealing of the contact and avoid virus solution loss during the injection; 1 µl of the virus solution per eye was injected by the microinjector at the rate of 10 nl/s (SMARTouch syringe pump controller MICRO-2T, WPI). To ensure good spreading of the viral particles in the vitreous space, glass capillary was retrieved from the eye after 10 minutes waiting time. To prevent infection, the eye was washed with a saline solution (0.9% sodium chloride) and eye ointment (VitA-POS) was applied. Imaging was performed 3-6 weeks after the injection.

#### **4.1.4 Systemic injection**

The mice from the line Ai95D received systemic injection of the rAAV2(PHP.eB)::CAG-iCre virus (80  $\mu$ l, diluted 1:1 with phosphate-buffered saline) into tail vein performed by our lab technician Dmitry Molotkov. Prior to injection, mice were anesthetized with isoflurane (4% for induction, 2% during the procedure).

#### **4.1.5 Retina dissection**

All retina dissection procedures were performed under very dim red light to avoid photoreceptor light excitation. Mice were dark adapted for a minimum of 45 minutes and euthanized with cervical dislocation. The eyes were immediately enucleated and placed in the oxygenated Ames's medium (Sigma-Aldrich, A1420; equilibrated with 95% O<sub>2</sub> and 5% CO<sub>2</sub> gas, at room temperature of 21°C) where retinas was dissected.

For the whole-mount retina recordings, the retina cup was cut into two halves. Retina piece was flattened onto the filter paper (13 mm diameter, 0.22  $\mu$ m MCE Membrane, MF-Millipore) on top of a 0.5-by-1 mm square hole in the middle to allow imaging. The retinal tissue on the filter paper was quickly transferred to the flow chamber with a ganglion cell side up facing the microscope objective. The tissue was perfused at 2ml/min flow rate with the oxygenated Ames's medium (37 °C) with red fluorescent dye sulphorhodamine-101 (SR101, 1  $\mu$ M, Sigma-Aldrich, S7635) that allowed to detect blood vessels and damaged cells.

For the retinal slice recordings, the isolated retina was placed on the intact filter paper with a ganglion cell side down and sliced fast with a cutter in 200  $\mu$ m pieces.

#### **4.1.6 Electroporation and bulk loading**

Experiments with these techniques were performed by our former master student Harsh Kanodia.

Previously established electroporation technique (Briggman & Euler, 2011) was used to deliver synthetic calcium indicators, Oregon Green 488 BAPTA-1 hexa-potassium salt (OGB1; Invitrogen, 06806) and Fluo-4 penta-potassium salt (Fluo-4; Invitrogen, F14200), to the retinal cells in the slice preparation. Voltage pulse duration was shortened from 10 to 5 ms for the retinal slices, while other parameters remained the same (1 Hz frequency, 13 V pulse amplitude, 10 pulses).

Bulk loading procedures were adapted from (Cameron et al., 2016) to stain retinal slices with calcium OGB1 acetoxymethyl ester (AM) dye (Invitrogen, 06807). Shortly, AM dye was dissolved in dimethyl sulfoxide (DMSO) containing 1% plurionic acid that allows lipophilic dye to form micelles and ensures solubilization. Dye solution was sonicated for 15 minutes and added to the oxygenated Ames's medium with a retinal slice on the filter paper to a final dye concentration of 20  $\mu$ M. Then, the retinal slice was incubated in the dye solution for 75 minutes at 37 °C; transferred to the dye free Ames's media for 30 minutes and imaged.

#### **4.1.7 Two-photon imaging**

Whole-mount retinas or retinal slices were imaged *in vitro* using a two-photon microscope (Scientifica) equipped with a mode-locked titanium:sapphire laser tuned to 920 nm (InSight DeepSee+, Spectra-Physics) with an Olympus XLUMPLFLN 20 $\times$  water immersion objective (NA 1, Olympus). Emitted fluorescence was captured through the objective and spitted into green and red channels for detection of the calcium transients and SR101 staining, respectively. Scanning and image acquisition were controlled under custom software written in LabView. For the z-scanning acquisition mode, electrically focus tunable lens (EL-16-40-TC, Optotune) was added to the light pass before the objective.

#### **4.1.8 Visual stimulation**

Retinal photoreceptors were stimulated with light from the bottom and cell responses were imaged with the objective on the top. Visual stimuli were prepared with customized QDSpy software (developed by Thomas Euler and implemented

and supported in our lab by PhD student Tom Boissonnet) (Euler, 2019; Franke et al., 2019). The stimulus was projected onto the retina through a custom-built lens system using digital light processing projector (DLP LightCrafter Display 3010, Texas Instruments). In the DLP, the original green light-emitting diode (LED) was replaced by a ultra-violet LED (365 nm; LZ1-00UV00, LED Engine) to effectively stimulate S-opsins and partially stimulate M-opsins and rhodopsin; the original blue LED (454 nm) was off due to the leak into the fluorescence detection channel; the original red LED was replaced by an infra-red LED (950 nm, SFH 4725S, Osram) that was not stimulating photoreceptors, but was detected separately by a photodiode to synchronize the timing of visual stimulation and image acquisition.

The presented stimuli were: (1) random binary full-field stimulation with different refresh rate (2, 4 and 6 Hz, 5 minutes long), (2) random binary checkerboard (4 Hz, 129×137.6  $\mu\text{m}$  checker size, 20 minutes), (3) random binary flickering bars (4 Hz, 21.5  $\mu\text{m}$  bar width, 25 minutes).

### **4.1.9 Analysis**

Signal extraction from the image timeseries was performed in Calcium Imaging Analysis tool (CaImAn) written in Python (Giovannucci et al., 2019). Shortly, the movies were first corrected for motion; then neutrophil noise and sources of activity were separated into single components using constrained nonnegative matrix factorization technique; resulting fluorescent traces were deconvolved to remove decay signals of the GCaMP slow inactivation and obtain the final estimate of the spiking activity of the cell. Spike timeseries were synchronized with the visual stimulation using the pipeline written in Python developed by Tom Boissonnet.

## **4.2 Results and discussion**

### **4.2.1 Monitoring retinal slices**

To get a clear access to all retinal cell layers, we first decided to use retinal slice preparation and monitor calcium signals as a proxy of neural activity. To

deliver calcium indicators to all retinal cell types, we have experimented with electroporation technique optimized from (Briggman & Euler, 2011) in 200  $\mu\text{m}$  thick retinal slices (Figure 4.1).

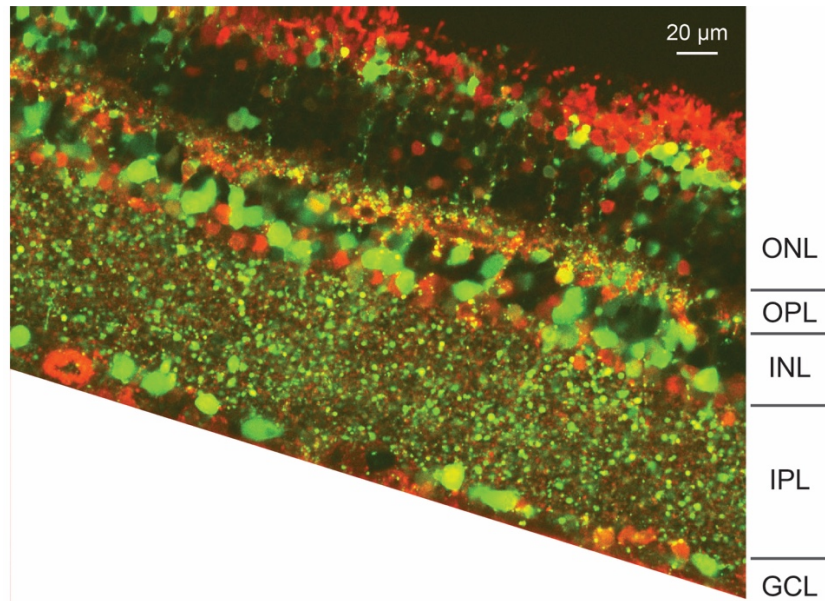


**Figure 4.1** Retinal slice electroporated with calcium indicator OGB1 (green) in the presence of SR101 (red) indicating dead cells. Many cells were successfully loaded with calcium indicator, but no calcium signals were observed. ONL – outer nuclear layer, OPL – outer plexiform layer, INL – inner nuclear layer, IPL – inner plexiform layer, GCL – ganglion cell layer.

Two types of calcium indicators (OGB1, Fluo-4, see Materials and Methods) were used for electroporation and tissue health was monitored with red dye (SR101) that enters blood vessels and damaged cells (Euler et al., 2009). Voltage pulses parameters were adjusted for a slice preparation by minimizing the number of red-labelled cells. Yet, even after achieving prevailing labeling of the cells with calcium indicator (Figure 4.1), no activity was observed in any of the cellular layers.

Possible reason for the lack of activity could be photoreceptor damage. On the most upper part of the Figure 4.1 (above ONL) we can see a lot of red-labeled outer segments of the photoreceptor cells where phototransduction should occur. Thus, if all of the photoreceptors have damaged outer segments, they would not be responsive to light. Nevertheless, we should have been able to see typical spontaneous activity of the retinal ganglion cells (RGCs) which was shown to be present in the retina with degenerated photoreceptors (Cameron et al., 2016). We

should also be able to observe light responses of the intrinsically photosensitive RGCs. As no signals were detected, we suggested that electroporation together with slicing is too damaging for the retinal tissue and decided to try more mild technique of the calcium indicator delivery – bulk loading.

Retinal slices were stained with the OGB1 AM calcium indicator dye following procedure described in (Cameron et al., 2016) where whole-mount retinas were used (see Materials and Methods). Retinal slices were often unrecoverable due to detachment from the filter paper caused by bubbling during incubation time (75 minutes). The recovered samples (~20%) showed low and punctuated fluorescence without any calcium signals (data not shown). Therefore, the technique was not considered for further optimization.

Slicing the retina removes a lot of long-range connections between the cells. As well, it appeared challenging to deliver calcium indicators and keep retinal slices viable. Therefore, we have abandoned such an approach and decided to access retinal signal flow in the whole-mount preparation as described below.

#### **4.2.2 Calcium indicators delivery**

The first critical step is to efficiently deliver calcium indicators to the retinal cells in all layers. We decided to use genetically encoded calcium indicators (GCaMP) that are expressed in the retinal cells upon virus infection via intravitreal injection. Dalkara and Byrne with colleagues have developed a 7m8 variant of adeno-associated virus 2 (AAV2) which leads to pan-retinal expression of the green fluorescent protein (Dalkara et al., 2013). We have tested this virus serotype with two different promoters, CAG and EF1 $\alpha$ , and two types of calcium indicators, GCaMP6s and GCaMP7f.

The first tested virus, rAAV7m8::CAG-jGCaMP7f, has shown a sparse, punctuated expression solely in the ganglion cell layer, most probably due to the low titer ( $6.0 \times 10^{11}$  vg/ml). The second virus, rAAV7m8::CAG-jGCaMP6s ( $3.1 \times 10^{12}$  vg/ml), was expressed well in the ganglion cell layer (Figure 4.2A), but sparsely in the inner nuclear layer (Figure 4.2B).

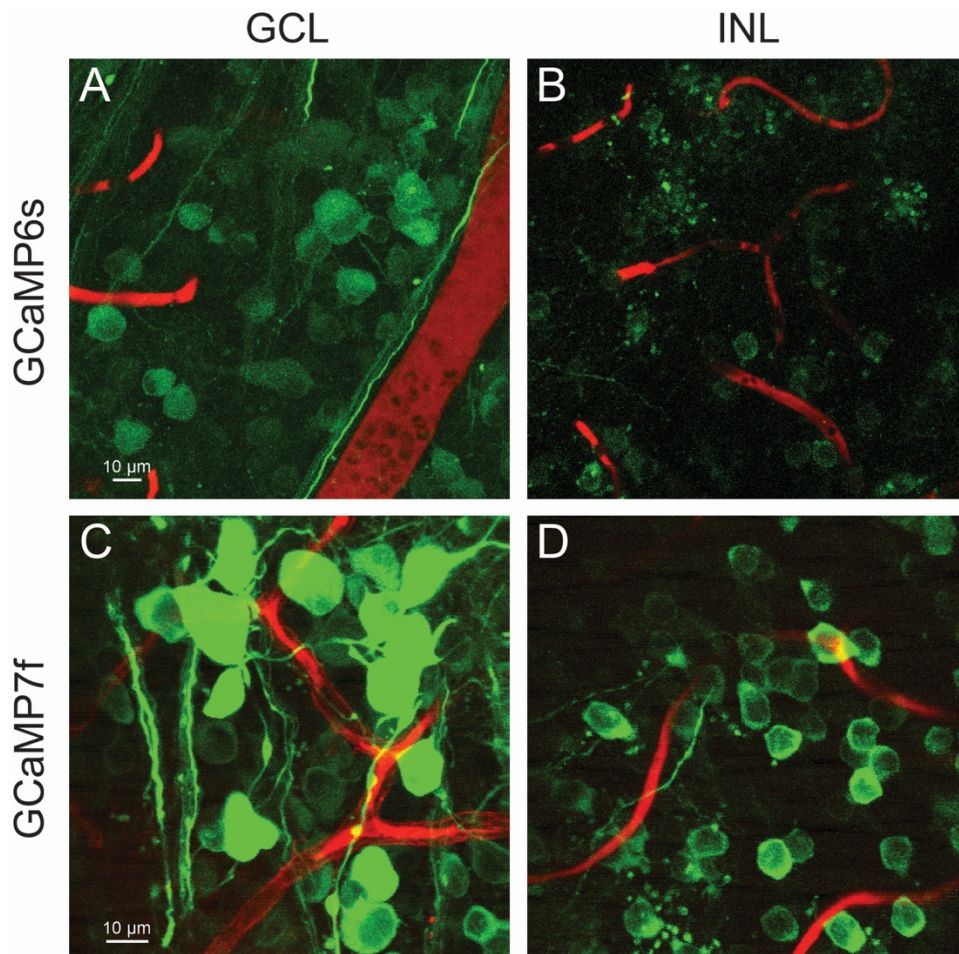


**Figure 4.2** GCaMP expression pattern in the retina explants. A, B: Maximum intensity projection of the ganglion cell layer (GCL) and inner nuclear layer (INL) z-stacks, respectively, acquired with two-photon microscope upon retina infection with rAAV7m8::CAG-jGCaMP6s. C, D: Corresponding panels as A, B for the retinas infected with rAAV7m8::CAG-FLEX-jGCaMP7f and rAAV7m8::EF1 $\alpha$ -Cre. Denser expression was observed in the INL.

Looking for more dense expression of the GCaMP in all retinal cells, we have tested the virus encoding GCaMP7f under more potent promoter EF1 $\alpha$ , rAAV7m8::EF1 $\alpha$ -jGCaMP7f. As well, considering efficiency of Cre recombinase in driving gene expression, we also used double infection strategy to deliver the virus encoding for GCaMP7f in Cre-dependent manner, rAAV7m8::CAG-FLEX-jGCaMP7f, and the second virus that promotes Cre recombinase expression, rAAV7m8::EF1 $\alpha$ -Cre. Due to delays in production of rAAV7m8::EF1 $\alpha$ -jGCaMP7f virus, we have first tested double infection technique. It resulted in more dense expression of GCaMP7f (Figure 4.2C, D), that as well appeared brighter than GCaMP6s. Later experiments with a single virus encoding GCaMP7f showed identical expression pattern.

We have tested light responses in the ganglion cell layer using random binary full-field stimulus with different refresh rates (2, 4 and 6 Hz, Figure 4.3). Due to the slow inactivation of GCaMP calcium signals, there is a temporal limitation of the stimulus frequency that allows to evaluate cell response properties. Ideally, we would like to keep the stimulus refresh rate as high as possible, but at least twice less frequent than image acquisition time of the responses (15.26 frames/s). Exploring spike-triggered averages (STA) of the same RGCs responding to full-field stimulus flickering at three frequencies (Figure 4.3C), we have chosen 4 Hz stimulation frequency to be optimal as 6 Hz stimulation often resulted in noisy STA and 2 Hz stimulation did not always match cell response dynamic. Different temporal properties of the ON and OFF RGCs responses could be observed.

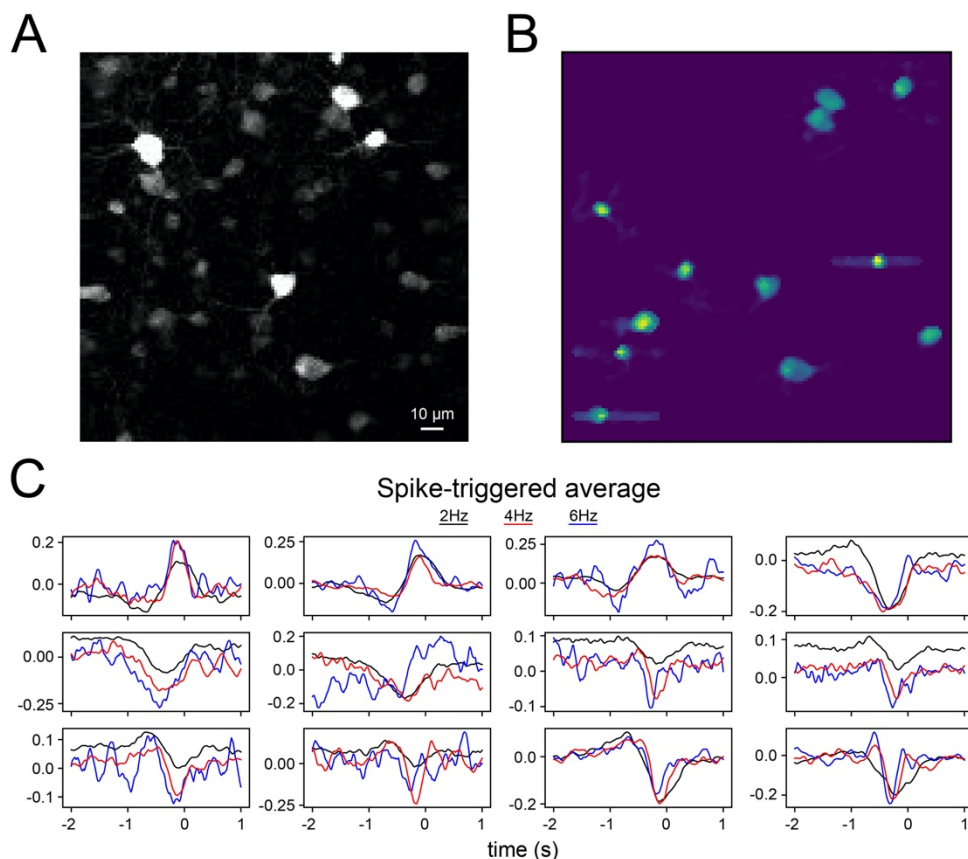


**Figure 4.3** Example recording with RGC visual responses estimated from calcium imaging. Retina upon virus double injection. A: Maximum intensity projection of the raw image timeseries. B: Regions of interest (ROI) identified with CaImAn that showed typical RGC spike-triggered average responses in C. C: For each of 12 ROIs, spike-triggered average was calculated in response to 2, 4 and 6 Hz (black, red and blue, respectively) random full-field flickering stimulus; cell response time is 0.

### 4.2.3 Z-scanning technique

For the whole-mount imaging of the signal flow in the retina, we envisioned monitoring calcium activity scanning the retina not in the common XY plane, but in the retinal cross-section XZ plane (Figure 4.4). The Z-scanning mode was enabled by adding electrically focus tunable lens to the two-photon microscope setup (see Materials and Methods). Switching between XY- and XZ-scanning mode allows us to record signals from a single cell layer, e.g. RGCs, or from single cross-section of all cell layers, respectively.

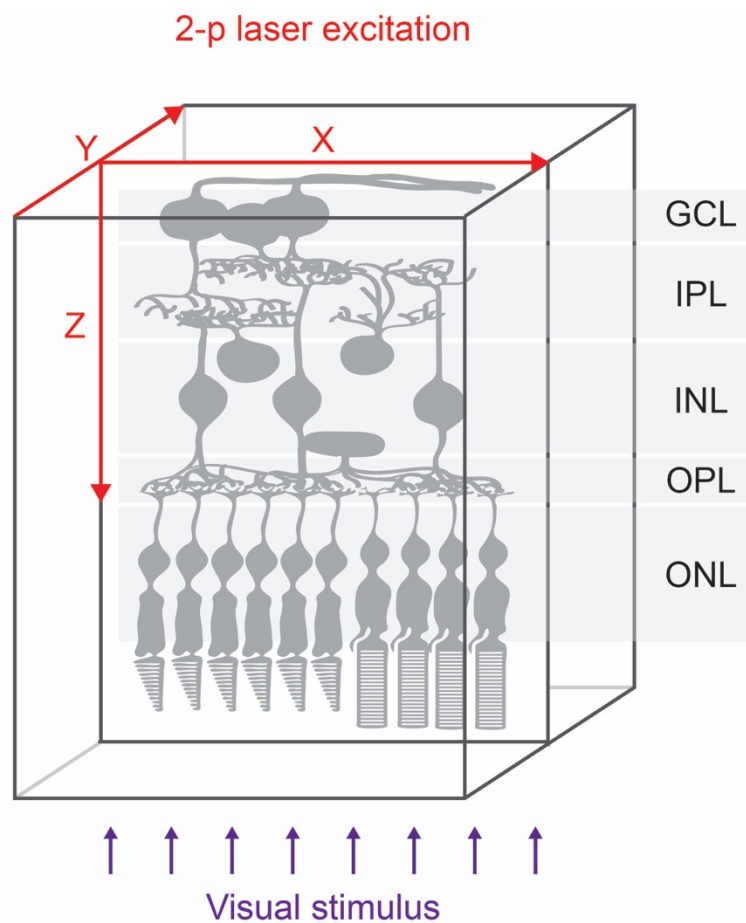


**Figure 4.4** Schematic diagram of the imaging planes in the whole-mount retina preparation. Visual stimulus is presented to the retina from below, while calcium indicators are excited from above in either XY- or XZ-mode. Retinal layers are marked on the side, same as in Figure 4.1.

We have successfully acquired signals from the cross-sections of the whole-mount retinas upon infection with rAAV7m8::EF1 $\alpha$ -jGCamP7f (Figure

4.5). Unfortunately, we noticed that there are little cells expressing GCaMP in the middle of the inner nuclear layer (INL) (Figure 4.5A, left). Horizontal cell somas are located at the top of the (INL), amacrine cell somas are close to the inner plexiform layer (IPL) and bipolar cell somas occupy top and center of the INL. The example cell on the Figure 4.5A (red) showed very slow calcium transients (Figure 4.5A, right) that were not correlated with light stimulus and typical for Müller glial cell (Newman, 2005). Rarely we could observe bipolar cell like light-evoked activity in the INL (Figure 4.5B-D). Figure 4.5C shows spike-triggered average response (STA) of the putative bipolar cell (Figure 4.5B, red) to the checkerboard stimulus. Because checkers of the stimulus were bigger ( $129 \times 137.6 \mu\text{m}$ ) than cell's receptive field, we can see only single checker changing intensity over time (Figure 4.5C, right). From the STA of the same cell responding to the flickering bars stimulus we can estimate the receptive field size to be around  $60 \mu\text{m}$ , which is typical for a bipolar cell (Berntson & Taylor, 2000). Consistent ON response polarity was observed from the positive peak in both STAs (Figure 4.5C, D). These preliminary XZ-scanning experiments also show that we can stably observe calcium transients for at least 1 hour.

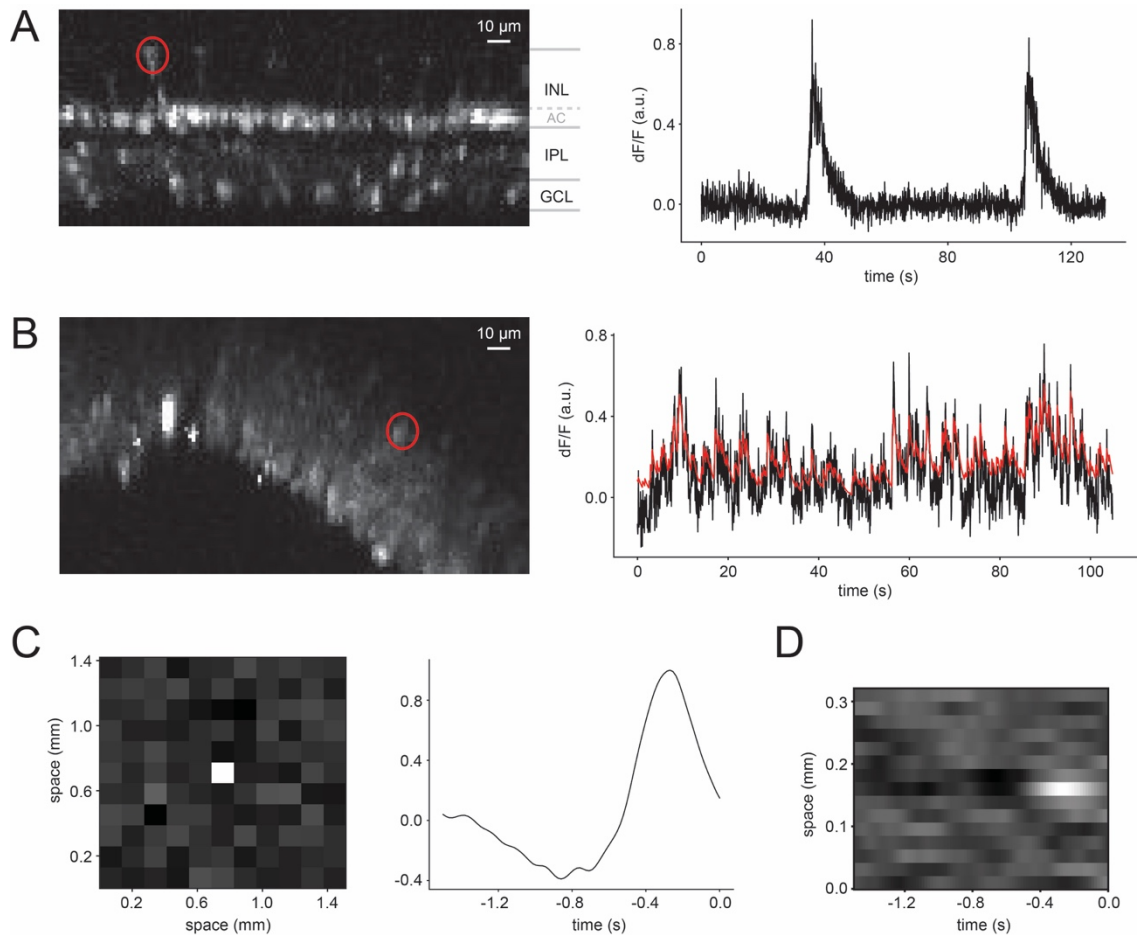


**Figure 4.5** Example XZ-scanning recordings of the whole-mount retinas infected with rAAV7m8::EF1 $\alpha$ -jGCaMP7f. A, left: Maximum intensity projection of the retina cross-section recorded during checkerboard stimulus presentation. No bipolar cells could be observed. INL – inner nuclear layer, AC – amacrine cells, IPL – inner plexiform layer, GCL – ganglion cell layer. A, right: Normalized fluorescence trace from the cell in the inner nuclear layer (red circle on the left) shows slow calcium transients. B: Same panels as in A. Red trace on the right is denoised signal produced in CaImAn. C: Spike-triggered average (STA) of the stimulus from the example bipolar cell (red circle in B) calculated from the activity during random checkerboard stimulus presentation: left – spatial STA, right – normalized temporal change of intensity of the central pixel on the left; time before the spike is indicated. D: STA of the same cell calculated from the activity during flickering bars stimulus presentation.

#### 4.2.4 Transgenic mouse lines

Bipolar cells relay visual signals from the outer to the inner retina, and having little to no signal from these cells will make it difficult to fully investigate signal flow in the retina. We continued to experiment with dense labelling of all retinal cells utilizing a transgenic mouse line Ai95D (see Materials and Methods). This line has a floxed-STOP cassette upstream of the GCaMP gene that can be removed by Cre recombinase. We have first tried systemic delivery of the Cre

recombinase encoding virus, rAAV2(PHP.eB)::CAG-iCre, in 4 mice. This systemic infection had severe side effects on the mouse health leading to death of 2 mice, while the other 2 mice were sacrificed to prevent suffering. The retina of one mouse was checked, but no expression was found. More targeted virus delivery was attempted with intravitreal injection of rAAV7m8::EF1 $\alpha$ -Cre into the eye. Yet, very little signal was observed in the RGC layer and no signal in the inner nuclear layer.

The most recent attempt to get dense labeling in the retina was initiated by crossing Ai95D mouse line with Rax-Cre mouse line (see Materials and Methods) which express Cre recombinase in the retinal cell progenitors. Retinal waves were recently recorded *in vivo* from the RGC axon terminals in the superior colliculus using such conditional expression of the GCaMP in RGCs (Gribizis et al., 2019). We expected that not only RGC, but all retinal cells should be GCaMP positive. In first preliminary experiments, we saw very dense expression in all retinal layers. Yet, instead of light responses, retinal wave like signals were observed in the retina from 1- and 2-month-old mice when waves should not occur. We suspect that an overexpression of GCaMP early in development may not allow final formation of the functional circuit. Other possibility is that very dense expression of GCaMP lead to laser evoked responses when photoreceptors are indirectly excited by scattered light (Euler et al., 2009). We also observed regions with only several cells expressing GCaMP that were responsive to light. Therefore, further investigations will be made when more mice will be available for experiments.

#### **4.2.5 Future directions**

Up to date we have a functional XZ-scanning two photon microscope setup where light responses across retinal cells can be monitored (Figure 4.5). The remaining challenge is to ensure dense labeling of the retinal cells without tissue damage. Virus infection with GCaMP showed promising results regarding tissue health, while dense population expression was observed in the Rax-Cre mice. Therefore, the next step is to combine these two approaches: infect retinal cells

using intravitreal injection of a virus encoding Cre-dependent GCaMP in the Rax-Cre mouse line, or, alternatively, activate Cre recombinase in the Cre inducible mouse line Rax-CreER(T2) crossed with Ai95D line (Pak, Yoo, Miranda-Angulo, Wang, & Blackshaw, 2014). We suggest that this combination will not interfere with retinal development and ensure expression of the virus in all different retinal cell types.

Resulting datasets of retinal processing cross-sections will require thorough analysis. A big variety of visual stimuli can be tested to differentially excite retinal cell and probe its vast functionality. In case of successful acquisition, these recordings will be shared with the computational neuroscience community to foster development of the new circuit models that ultimately expand our understanding of retinal computations.

## Bibliography

- Ackman, J. B., Burbridge, T. J., & Crair, M. C. (2012). Retinal waves coordinate patterned activity throughout the developing visual system. *Nature*, *490*(7419). <https://doi.org/10.1038/nature11529>
- Akopian, A., & Witkovsky, P. (1996). D2 dopamine receptor-mediated inhibition of a hyperpolarization-activated current in rod photoreceptors. *Journal of Neurophysiology*, *76*(3). <https://doi.org/10.1152/jn.1996.76.3.1828>
- Aloe, L., Rocco, M., Balzamino, B., & Micera, A. (2015). Nerve Growth Factor: A Focus on Neuroscience and Therapy. *Current Neuropharmacology*, *13*(3). <https://doi.org/10.2174/1570159x13666150403231920>
- Anderson, J. R., Jones, B. W., Yang, J. H., Shaw, M. V., Watt, C. B., Koshevoy, P., ... Marc, R. E. (2009). A computational framework for ultrastructural mapping of neural circuitry. *PLoS Biology*, *7*(3), 0493–0512. <https://doi.org/10.1371/journal.pbio.1000074>
- Anderson, S. R., Zhang, J., Steele, M. R., Romero, C. O., Kautzman, A. G., Schafer, D. P., & Vetter, M. L. (2019). Complement targets newborn retinal ganglion cells for phagocytic elimination by microglia. *Journal of Neuroscience*, *39*(11). <https://doi.org/10.1523/JNEUROSCI.1854-18.2018>
- Asari, H., & Meister, M. (2012). Divergence of visual channels in the inner retina. *Nature Neuroscience*, *15*(11). <https://doi.org/10.1038/nn.3241>
- Asari, H., & Meister, M. (2014). The projective field of retinal bipolar cells and its modulation by visual context. *Neuron*, *81*, 641–652.
- Awatramani, G. B., & Slaughter, M. M. (2000). Origin of transient and sustained responses in ganglion cells of the retina. *Journal of Neuroscience*, *20*(18), 7087–7095. <https://doi.org/10.1523/jneurosci.20-18-07087.2000>
- Azeredo da Silveira, R., & Roska, B. (2011). Cell Types, Circuits, Computation. *Current Opinion in Neurobiology*. <https://doi.org/10.1016/j.conb.2011.05.007>
- Baden, T., Berens, P., Franke, K., Román Rosón, M., Bethge, M., & Euler, T. (2016). The functional diversity of retinal ganglion cells in the mouse. *Nature*, *529*(7586), 345–350. <https://doi.org/10.1038/nature16468>

- Baden, T., Schubert, T., Berens, P., Euler, T., Baden, T., Schubert, T., ... Euler, T. (2018). *The Functional Organization of Vertebrate Retinal Circuits for Vision*. *Oxford Research Encyclopedia of Neuroscience*. <https://doi.org/10.1093/acrefore/9780190264086.013.68>
- Baden, T., Schubert, T., Chang, L., Wei, T., Zaichuk, M., Wissinger, B., & Euler, T. (2013). A tale of two retinal domains: Near-Optimal sampling of achromatic contrasts in natural scenes through asymmetric photoreceptor distribution. *Neuron*, *80*(5), 1206–1217. <https://doi.org/10.1016/j.neuron.2013.09.030>
- Bae, J. A., Mu, S., Kim, J. S., Turner, N. L., Tartavull, I., Kemnitz, N., ... Seung, H. S. (2018). Digital Museum of Retinal Ganglion Cells with Dense Anatomy and Physiology. *Cell*, *173*(5), 1293-1306.e19. <https://doi.org/10.1016/j.cell.2018.04.040>
- Bansal, A., Singer, J. H., Hwang, B. J., Xu, W., Beaudet, A., & Feller, M. B. (2000). Mice lacking specific nicotinic acetylcholine receptor subunits exhibit dramatically altered spontaneous activity patterns and reveal a limited role for retinal waves in forming ON and OFF circuits in the inner retina. *Journal of Neuroscience*, *20*(20). <https://doi.org/10.1523/jneurosci.20-20-07672.2000>
- Baylor, D. (1996). How photons start vision. *Proceedings of the National Academy of Sciences of the United States of America*, *93*(2), 560–565. <https://doi.org/10.1073/pnas.93.2.560>
- Bellver-Landete, V., Bretheau, F., Mailhot, B., Vallières, N., Lessard, M., Janelle, M. E., ... Lacroix, S. (2019). Microglia are an essential component of the neuroprotective scar that forms after spinal cord injury. *Nature Communications*, *10*(1). <https://doi.org/10.1038/s41467-019-08446-0>
- Berntson, A., & Taylor, W. R. (2000). Response characteristics and receptive field widths of on-bipolar cells in the mouse retina. *Journal of Physiology*, *524*(3). <https://doi.org/10.1111/j.1469-7793.2000.00879.x>
- Blankenship, A. G., & Feller, M. B. (2010). Mechanisms underlying spontaneous patterned activity in developing neural circuits. *Nature Reviews Neuroscience*. <https://doi.org/10.1038/nrn2759>
- Bloomfield, S. A., & Völgyi, B. (2009). The diverse functional roles and regulation

- of neuronal gap junctions in the retina. *Nature Reviews Neuroscience*.  
<https://doi.org/10.1038/nrn2636>
- Bloomfield, S. A., Xin, D., & Osborne, T. (1997). Light-induced modulation of coupling between AII amacrine cells in the rabbit retina. *Visual Neuroscience*, *14*(3). <https://doi.org/10.1017/S0952523800012220>
- Bloomfield, S. A., Xin, D., & Persky, S. E. (1995). A comparison of receptive field and tracer coupling size of horizontal cells in the rabbit retina. *Visual Neuroscience*, *12*(5). <https://doi.org/10.1017/S0952523800009524>
- Brien, J. O., & Bloomfield, S. A. (2018). Plasticity of Retinal Gap Junctions : Roles in Synaptic Physiology and Disease.
- Briggman, K. L., & Euler, T. (2011). Bulk electroporation and population calcium imaging in the adult mammalian retina. *Journal of Neurophysiology*, *105*(5), 2601–2609. <https://doi.org/10.1152/jn.00722.2010>
- Briggman, K. L., Helmstaedter, M., & Denk, W. (2011). Wiring specificity in the direction-selectivity circuit of the retina. *Nature*, *471*(7337), 183–190. <https://doi.org/10.1038/nature09818>
- Brivanlou, I. H., Warland, D. K., & Meister, M. (1998a). Mechanisms of concerted firing among retinal ganglion cells. *Neuron*, *20*(3). [https://doi.org/10.1016/S0896-6273\(00\)80992-7](https://doi.org/10.1016/S0896-6273(00)80992-7)
- Brivanlou, I. H., Warland, D. K., & Meister, M. (1998b). Mechanisms of Concerted Firing among Retinal Ganglion Cells, *20*, 527–539.
- Bukauskas, F. F., Angele, A. B., Verselis, V. K., & Bennett, M. V. L. (2002). Coupling asymmetry of heterotypic connexin 45/connexin 43-EGFP gap junctions: Properties of fast and slow gating mechanisms. *Proceedings of the National Academy of Sciences of the United States of America*, *99*(10). <https://doi.org/10.1073/pnas.032062099>
- Cameron, M., Kekesi, O., Morley, J. W., Tapson, J., Breen, P. P., Van Schaik, A., & Buskila, Y. (2016). Calcium imaging of am dyes following prolonged incubation in acute neuronal tissue. *PLoS ONE*, *11*(5), 1–13. <https://doi.org/10.1371/journal.pone.0155468>
- Carandini, M., & Heeger, D. J. (2012). Normalization as a canonical neural

- computation. *Nature Reviews Neuroscience*, *13*(1), 51–62.  
<https://doi.org/10.1038/nrn3136>
- Carmignoto, G., Maffei, L., Candeo, P., Canella, R., & Comelli, C. (1989). Effect of NGF on the survival of rat retinal ganglion cells following optic nerve section. *Journal of Neuroscience*, *9*(4). <https://doi.org/10.1523/jneurosci.09-04-01263.1989>
- Cattaneo, A., Capsoni, S., Margotti, E., Righi, M., Kontsekova, E., Pavlik, P., ... Novak, M. (1999). Functional blockade of tyrosine kinase A in the rat basal forebrain by a novel antagonistic anti-receptor monoclonal antibody. *Journal of Neuroscience*, *19*(22). <https://doi.org/10.1523/jneurosci.19-22-09687.1999>
- Chaya, T., Matsumoto, A., Sugita, Y., Watanabe, S., & Kuwahara, R. (2017). Versatile functional roles of horizontal cells in the retinal circuit. *Scientific Reports*, (May), 1–15. <https://doi.org/10.1038/s41598-017-05543-2>
- Chichilnisky, E. J. (2001). A simple white noise analysis of neuronal light, *12*, 199–213.
- Cocco, S., Leibler, S., & Monasson, R. (2009). Neuronal couplings between retinal ganglion cells inferred by efficient inverse statistical physics methods. *Proceedings of the National Academy of Sciences of the United States of America*, *106*(33), 14058–14062. <https://doi.org/10.1073/pnas.0906705106>
- Colafrancesco, V., Parisi, V., Sposato, V., Rossi, S., Russo, M. A., Coassin, M., ... Aloe, L. (2011). Ocular application of nerve growth factor protects degenerating retinal ganglion cells in a rat model of glaucoma. *Journal of Glaucoma*, *20*(2). <https://doi.org/10.1097/IJG.0b013e3181d787e5>
- Colonnese, M. T., & Khazipov, R. (2010). “Slow activity transients” in infant rat visual cortex: A spreading synchronous oscillation patterned by retinal waves. *Journal of Neuroscience*, *30*(12). <https://doi.org/10.1523/JNEUROSCI.4995-09.2010>
- Constantine-Paton, M., Cline, H. T., & Debski, E. (1990). Patterned activity, synaptic convergence, and the NMDA receptor in developing visual pathways. *Annual Review of Neuroscience*, *13*(1). <https://doi.org/10.1146/annurev.ne.13.030190.001021>

- Cook, J. E., & Becker, D. L. (1995). Gap junctions in the vertebrate retina. *Microscopy Research and Technique*, 31(5). <https://doi.org/10.1002/jemt.1070310510>
- Cooler, S., & Schwartz, G. W. (2020). An offset ON-OFF receptive field is created by gap junctions between distinct types of retinal ganglion cells. *BioRxiv*, 1–15.
- Curcio, C. A., Sloan, K. R., Kalina, R. E., & Hendrickson, A. E. (1990). Human photoreceptor topography. *Journal of Comparative Neurology*, 292(4), 497–523. <https://doi.org/10.1002/cne.902920402>
- Dalkara, D., Byrne, L. C., Klimczak, R. R., Visel, M., Yin, L., Merigan, W. H., ... Schaffer, D. V. (2013). In Vivo – Directed Evolution of a New Adeno-Associated Virus for Therapeutic Outer Retinal Gene Delivery from the Vitreous, 5(189), 1–12.
- Demb, J. B., & Singer, J. H. (2015). *Functional Circuitry of the Retina*. *Annual Review of Vision Science* (Vol. 1). <https://doi.org/10.1146/annurev-vision-082114-035334>
- Denk, W., & Detwiler, P. B. (1999). Optical recording of light-evoked calcium signals in the functionally intact retina. *Proceedings of the National Academy of Sciences of the United States of America*, 96(12), 7035–7040. <https://doi.org/10.1073/pnas.96.12.7035>
- Devries, S. H. (2000). Bipolar Cells Use Kainate and AMPA Receptors to Filter Visual Information into Separate Channels (X-like), and direction-selective responses in retinal ganglion cells (Cohen and Sterling, 1990). If bipolar cells function only to carry ON and OFF signals. *Neuron*, 28, 847–856.
- Devries, S. H., & Baylor, D. A. (1995). An alternative pathway for signal flow from rod photoreceptors to ganglion cells in mammalian retina. *Proceedings of the National Academy of Sciences of the United States of America*, 92(23). <https://doi.org/10.1073/pnas.92.23.10658>
- DeVries, S. H., Qi, X., Smith, R., Makous, W., & Sterling, P. (2002). Electrical coupling between mammalian cones. *Current Biology*, 12(22), 1900–1907. [https://doi.org/10.1016/S0960-9822\(02\)01261-7](https://doi.org/10.1016/S0960-9822(02)01261-7)

- Diamond, J. S. (2017). Inhibitory Interneurons in the Retina: Types, Circuitry, and Function. *Annual Review of Vision Science*. <https://doi.org/10.1146/annurev-vision-102016-061345>
- Dong, C. J., & McReynolds, J. S. (1991). The relationship between light, dopamine release and horizontal cell coupling in the mudpuppy retina. *The Journal of Physiology*. <https://doi.org/10.1113/jphysiol.1991.sp018709>
- Dong, Cun Jian, & Werblin, F. S. (1998). Temporal contrast enhancement via GABA(c) feedback at bipolar terminals in the tiger salamander retina. *Journal of Neurophysiology*, 79(4), 2171–2180. <https://doi.org/10.1152/jn.1998.79.4.2171>
- Drinneberg, A., Franke, F., Morikawa, R. K., Jüttner, J., Hillier, D., Hantz, P., ... Roska, B. (2018). How Diverse Retinal Functions Arise from Feedback at the First Visual Synapse. *Neuron*, 117–134. <https://doi.org/10.1016/j.neuron.2018.06.001>
- Euler, T. (2019). QDSpy. GitHub. Retrieved from <https://github.com/eulerlab/QDSpy>
- Euler, T., Hausselt, S. E., Margolis, D. J., Breuninger, T., Castell, X., Detwiler, P. B., & Denk, W. (2009). Eyecup scope-optical recordings of light stimulus-evoked fluorescence signals in the retina. *Pflügers Archiv European Journal of Physiology*, 457(6), 1393–1414. <https://doi.org/10.1007/s00424-008-0603-5>
- Euler, T., Haverkamp, S., Schubert, T., & Baden, T. (2014). Retinal bipolar cells: Elementary building blocks of vision. *Nature Reviews Neuroscience*. <https://doi.org/10.1038/nrn3783>
- Famiglietti, E. V., & Kolb, H. (1975). A bistratified amacrine cell and synaptic circuitry in the inner plexiform layer of the retina. *Brain Research*, 84(2). [https://doi.org/10.1016/0006-8993\(75\)90983-X](https://doi.org/10.1016/0006-8993(75)90983-X)
- Ferguson, L. R., Dominguez, J. M., Balaiya, S., Grover, S., & Chalam, K. V. (2013). Retinal Thickness Normative Data in Wild-Type Mice Using Customized Miniature SD-OCT. *PLoS ONE*, 8(6), 1–8. <https://doi.org/10.1371/journal.pone.0067265>

- Ferrer-Martín, R. M., Martín-Oliva, D., Sierra-Martín, A., Carrasco, M. C., Martín-Estebané, M., Calvente, R., ... Cuadros, M. A. (2015). Microglial activation promotes cell survival in organotypic cultures of postnatal mouse retinal explants. *PLoS ONE*, *10*(8). <https://doi.org/10.1371/journal.pone.0135238>
- Field, G. D., & Chichilnisky, E. J. (2007). Information processing in the primate retina: Circuitry and coding. *Annual Review of Neuroscience*. <https://doi.org/10.1146/annurev.neuro.30.051606.094252>
- Flores-Herr, N., Protti, D. A., & Wässle, H. (2001). Synaptic currents generating the inhibitory surround of ganglion cells in the mammalian retina. *Journal of Neuroscience*, *21*(13). <https://doi.org/10.1523/jneurosci.21-13-04852.2001>
- Franke, K., Chagas, A. M., Zhao, Z., Zimmermann, M. J. Y., Bartel, P., Qiu, Y., ... Euler, T. (2019). An arbitrary-spectrum spatial visual stimulator for vision research. *eLife*, *8*. <https://doi.org/10.7554/eLife.48779>
- Fu, Y., & Yau, K. W. (2007). Phototransduction in mouse rods and cones. *Pflügers Archiv European Journal of Physiology*. <https://doi.org/10.1007/s00424-006-0194-y>
- Furshpan, E. J., & Potter, D. D. (1959). Transmission at the giant motor synapses of the crayfish. *The Journal of Physiology*, *145*(2). <https://doi.org/10.1113/jphysiol.1959.sp006143>
- Gastinger, M., Tian, N., Horvath, T., & Marshak, D. (2006). Retinopetal axons in mammals: Emphasis on histamine and serotonin. *Current Eye Research*, *31*(7–8). <https://doi.org/10.1080/02713680600776119>
- Gibson, J. R., Beierlein, M., & Connors, B. W. (2005). Functional properties of electrical synapses between inhibitory interneurons of neocortical layer 4. *Journal of Neurophysiology*, *93*(1), 467–480. <https://doi.org/10.1152/jn.00520.2004>
- Giovannucci, A., Friedrich, J., Gunn, P., Kalfon, J., Brown, B. L., Koay, S. A., ... Pnevmatikakis, E. A. (2019). CaImAn an open source tool for scalable calcium imaging data analysis, 1–45.
- Gollisch, T., & Meister, M. (2010). Eye Smarter than Scientists Believed: Neural Computations in Circuits of the Retina. *Neuron*.

<https://doi.org/10.1016/j.neuron.2009.12.009>

- Goodenough, D. A., & Revel, J. P. (1970). A fine structural analysis of intercellular junctions in the mouse liver. *Journal of Cell Biology*, 45(2). <https://doi.org/10.1083/jcb.45.2.272>
- Gouras, P. (1969). Antidromic responses of orthodromically identified ganglion cells in monkey retina. *The Journal of Physiology*, 204(2). <https://doi.org/10.1113/jphysiol.1969.sp008920>
- Greschner, M., Heitman, A. K., Field, G. D., Li, P. H., Ahn, D., Sher, A., ... Chichilnisky, E. J. (2016). Identification of a Retinal Circuit for Recurrent Suppression Using Indirect Electrical Imaging. *Current Biology*, 26(15). <https://doi.org/10.1016/j.cub.2016.05.051>
- Gribizis, A., Ge, X., Daigle, T. L., Ackman, J. B., Zeng, H., Lee, D., & Crair, M. C. (2019). Visual Cortex Gains Independence from Peripheral Drive before Eye Opening. *Neuron*, 104(4). <https://doi.org/10.1016/j.neuron.2019.08.015>
- Grienberger, C., & Konnerth, A. (2012). Imaging Calcium in Neurons. *Neuron*. <https://doi.org/10.1016/j.neuron.2012.02.011>
- Guo, L., Davis, B. M., Ravindran, N., Galvao, J., Kapoor, N., Haamedi, N., ... Cordeiro, M. F. (2020). Topical recombinant human Nerve growth factor (rh-NGF) is neuroprotective to retinal ganglion cells by targeting secondary degeneration. *Scientific Reports*, 10(1). <https://doi.org/10.1038/s41598-020-60427-2>
- Hampson, E. C. G. M., Vaney, D. I., & Weiler, R. (1992). Dopaminergic modulation of gap junction permeability between amacrine cells in mammalian retina. *Journal of Neuroscience*, 12(12). <https://doi.org/10.1523/jneurosci.12-12-04911.1992>
- Haverkamp, S., Wässle, H., Duebel, J., Künér, T., Augustine, G. J., Feng, G., & Euler, T. (2005). The primordial, blue-cone color system of the mouse retina. *Journal of Neuroscience*, 25(22). <https://doi.org/10.1523/JNEUROSCI.1117-05.2005>
- Hecht, S., Shlaer, S., & Pirenne, M. H. (1942). Energy, quanta, and vision. *Journal of General Physiology*, 25(6), 819–840. <https://doi.org/10.1085/jgp.25.6.819>

- Helmstaedter, M., Briggman, K. L., Turaga, S. C., Jain, V., Seung, H. S., & Denk, W. (2013). Connectomic reconstruction of the inner plexiform layer in the mouse retina. *Nature*, *500*(7461), 168–174. <https://doi.org/10.1038/nature12346>
- Herrmann, R., Heflin, S. J., Hammond, T., Lee, B., Wang, J., Gainetdinov, R. R., ... Arshavsky, V. Y. (2011). Article Rod Vision Is Controlled by Dopamine-Dependent Sensitization of Rod Bipolar Cells by GABA. *NEURON*, *72*(1), 101–110. <https://doi.org/10.1016/j.neuron.2011.07.030>
- Hidaka, S., Akahori, Y., & Kurosawa, Y. (2004). Dendrodendritic electrical synapses between mammalian retinal ganglion cells. *Journal of Neuroscience*, *24*(46). <https://doi.org/10.1523/JNEUROSCI.3319-04.2004>
- Hodgkin, A. L., & Huxley, A. F. (1952). A quantitative description of membrane current and its application to conduction and excitation in nerve. *The Journal of Physiology*, *117*(4). <https://doi.org/10.1113/jphysiol.1952.sp004764>
- Hormuzdi, S. G., Filippov, M. A., Mitropoulou, G., Monyer, H., & Bruzzone, R. (2004, March 23). Electrical synapses: A dynamic signaling system that shapes the activity of neuronal networks. *Biochimica et Biophysica Acta - Biomembranes*. <https://doi.org/10.1016/j.bbamem.2003.10.023>
- Hu, E. H., & Bloomfield, S. A. (2003). Gap junctional coupling underlies the short-latency spike synchrony of retinal  $\alpha$  ganglion cells. *Journal of Neuroscience*, *23*(17). <https://doi.org/10.1523/jneurosci.23-17-06768.2003>
- Huang, E. J., & Reichardt, L. F. (2003). Trk receptors: Roles in neuronal signal transduction. *Annual Review of Biochemistry*. <https://doi.org/10.1146/annurev.biochem.72.121801.161629>
- Ito, M. (2000). Mechanisms of motor learning in the cerebellum. *Brain Research*, *886*(1–2). [https://doi.org/10.1016/S0006-8993\(00\)03142-5](https://doi.org/10.1016/S0006-8993(00)03142-5)
- Jackman, S. L., Babai, N., Chambers, J. J., Thoreson, W. B., & Kramer, R. H. (2011). A positive feedback synapse from retinal horizontal cells to cone photoreceptors. *PLoS Biology*, *9*(5). <https://doi.org/10.1371/journal.pbio.1001057>
- Jacobs, G. H., Neitz, J., & Deegan, J. F. (1991). Retinal receptors in rodents

- maximally sensitive to ultraviolet light. *Nature*, 353(6345).  
<https://doi.org/10.1038/353655a0>
- Jin, N. G., Chuang, A. Z., Masson, P. J., & Ribelayga, C. P. (2015). Rod electrical coupling is controlled by a circadian clock and dopamine in mouse retina. *Journal of Physiology*, 593(7), 1597–1631.  
<https://doi.org/10.1113/jphysiol.2014.284919>
- Kenyon, G. T., & Marshak, D. W. (1998). Gap junctions with amacrine cells provide a feedback pathway for ganglion cells within the retina. *Proceedings of the Royal Society B: Biological Sciences*, 265(1399).  
<https://doi.org/10.1098/rspb.1998.0379>
- Kim, T., Shen, N., Hsiang, J. C., Johnson, K. P., & Kerschensteiner, D. (2020). Dendritic and parallel processing of visual threats in the retina control defensive responses. *Science Advances*, 6(47), 1–12.  
<https://doi.org/10.1126/sciadv.abc9920>
- Kobayashi, T., Nakamura, H., & Yasuda, M. (1990). Disturbance of refinement of retinotectal projection in chick embryos by tetrodotoxin and grayanotoxin. *Developmental Brain Research*, 57(1). [https://doi.org/10.1016/0165-3806\(90\)90181-W](https://doi.org/10.1016/0165-3806(90)90181-W)
- Koch, C. (1998). *Biophysics of Computation: Information Processing in Single Neurons*. New York: Oxford University Press.
- Kolb, H., & Famiglietti, E. V. (1974). Rod and cone pathways in the inner plexiform layer of cat retina. *Science*, 186(4158).  
<https://doi.org/10.1126/science.186.4158.47>
- Koves, K., & Csaki, A. (2016). Recent Research on the Centrifugal Visual System in Mammalian Species. *Anatomy & Physiology*, 06(03).  
<https://doi.org/10.4172/2161-0940.1000216>
- Kuffler, S. W. (1953). Discharge patterns and functional organization of mammalian retina. *Journal of Neurophysiology*, 16(1).  
<https://doi.org/10.1152/jn.1953.16.1.37>
- Kumar, N. M., & Gilula, N. B. (1992). Molecular biology and genetics of gap junction channels. *Seminars in Cell Biology*, 3(1), 3–16.

[https://doi.org/10.1016/S1043-4682\(10\)80003-0](https://doi.org/10.1016/S1043-4682(10)80003-0)

- Lambiase, A., Aloe, L., Centofanti, M., Parisi, V., Mantelli, F., Colafrancesco, V., ... Levi-Montalcini, R. (2009). Experimental and clinical evidence of neuroprotection by nerve growth factor eye drops: Implications for glaucoma. *Proceedings of the National Academy of Sciences of the United States of America*, *106*(32). <https://doi.org/10.1073/pnas.0906678106>
- Lapicque, L. (1907). Recherches quantitatives sur l'excitation électrique des nerfs traitée comme une polarisation. *J. Physiol. Pathol. Gen.*, *9*.
- Lasater, E. M., & Dowling, J. E. (1985). Dopamine decreases conductance of the electrical junctions between cultured retinal horizontal cells. *Proceedings of the National Academy of Sciences of the United States of America*, *82*(9), 3025–3029. <https://doi.org/10.1073/pnas.82.9.3025>
- Lefebvre, J. L., Zhang, Y., Meister, M., Wang, X., & Sanes, J. R. (2008).  $\gamma$ -Protocadherins regulate neuronal survival but are dispensable for circuit formation in retina. *Development*, *135*(24). <https://doi.org/10.1242/dev.027912>
- Levi-Montalcini, R. (1987). The nerve growth factor: thirty-five years later. *The EMBO Journal*. <https://doi.org/10.1002/j.1460-2075.1987.tb02347.x>
- Lewis, T. J., & Rinzel, J. (2000). Self-organized synchronous oscillations in a network of excitable cells coupled by gap junctions. *Network: Computation in Neural Systems*, *11*(4). [https://doi.org/10.1088/0954-898X\\_11\\_4\\_304](https://doi.org/10.1088/0954-898X_11_4_304)
- Li, F., Jiang, D., & Samuel, M. A. (2019). Microglia in the developing retina. *Neural Development*. <https://doi.org/10.1186/s13064-019-0137-x>
- Li, P. H., Verweij, J., Long, J. H., & Schnapf, J. L. (2012). Gap-junctional coupling of mammalian rod photoreceptors and its effect on visual detection. *Journal of Neuroscience*, *32*(10). <https://doi.org/10.1523/JNEUROSCI.2144-11.2012>
- Lin, B., & Masland, R. H. (2006). Populations of wide-field amacrine cells in the mouse retina. *Journal of Comparative Neurology*, *499*(5). <https://doi.org/10.1002/cne.21126>
- Maass, W., & Markram, H. (2004). On the computational power of circuits of spiking neurons. *Journal of Computer and System Sciences*, *69*(4), 593–616.

<https://doi.org/10.1016/j.jcss.2004.04.001>

- Maccione, A., Hennig, M. H., Gandolfo, M., Muthmann, O., van Coppenhagen, J., Eglen, S. J., ... Sernagor, E. (2014). Following the ontogeny of retinal waves: Pan-retinal recordings of population dynamics in the neonatal mouse. *Journal of Physiology*, 592(7). <https://doi.org/10.1113/jphysiol.2013.262840>
- Macneil, M. A., Heussy, J. K., Dacheux, R. F., Raviola, E., & Masland, R. H. (1999). The shapes and numbers of amacrine cells: Matching of photofilled with Golgi-stained cells in the rabbit retina and comparison with other mammalian species. *Journal of Comparative Neurology*, 413(2). [https://doi.org/10.1002/\(SICI\)1096-9861\(19991018\)413:2<305::AID-CNE10>3.0.CO;2-E](https://doi.org/10.1002/(SICI)1096-9861(19991018)413:2<305::AID-CNE10>3.0.CO;2-E)
- MacNeil, M. A., & Masland, R. H. (1998). Extreme diversity among amacrine cells: Implications for function. *Neuron*, 20(5). [https://doi.org/10.1016/S0896-6273\(00\)80478-X](https://doi.org/10.1016/S0896-6273(00)80478-X)
- Maffei, L., & Galli-Resta, L. (1990). Correlation in the discharges of neighboring rat retinal ganglion cells during prenatal life. *Proceedings of the National Academy of Sciences of the United States of America*, 87(7). <https://doi.org/10.1073/pnas.87.7.2861>
- Marinelli, S., Basilico, B., Marrone, M. C., & Ragozzino, D. (2019). Microglia-neuron crosstalk: Signaling mechanism and control of synaptic transmission. *Seminars in Cell and Developmental Biology*, 94(April), 138–151. <https://doi.org/10.1016/j.semcdb.2019.05.017>
- Masland, R. H. (1977). Maturation of function in the developing rabbit retina. *Journal of Comparative Neurology*, 175(3). <https://doi.org/10.1002/cne.901750303>
- Masland, R. H. (2012). The Neuronal Organization of the Retina. *Neuron*. <https://doi.org/10.1016/j.neuron.2012.10.002>
- Mastrorarde, D. N. (1983). Interactions between ganglion cells in cat retina. *Journal of Neurophysiology*, 49(2), 350–365. <https://doi.org/10.1152/jn.1983.49.2.350>
- Matthews, G. (1999). Synaptic mechanisms of bipolar cell terminals. *Vision*

- Research*, 39(15). [https://doi.org/10.1016/S0042-6989\(98\)00249-1](https://doi.org/10.1016/S0042-6989(98)00249-1)
- Meister, M., Pine, J., & Baylor, D. A. (1994). Multi-neuronal signals from the retina: acquisition and analysis. *Journal of Neuroscience Methods*, 51(1). [https://doi.org/10.1016/0165-0270\(94\)90030-2](https://doi.org/10.1016/0165-0270(94)90030-2)
- Meister, M., Wong, R. O. L., Baylor, D. A., & Shatz, C. J. (1991). Synchronous bursts of action potentials in ganglion cells of the developing mammalian retina. *Science*, 252(5008). <https://doi.org/10.1126/science.2035024>
- Mesentier-Louro, L. A., De Nicolò, S., Rosso, P., De Vitis, L. A., Castoldi, V., Leocani, L., ... Lambiase, A. (2017). Time-dependent nerve growth factor signaling changes in the rat retina during optic nerve crush-induced degeneration of retinal ganglion cells. *International Journal of Molecular Sciences*, 18(1). <https://doi.org/10.3390/ijms18010098>
- Mooney, R., Penn, A. A., Gallego, R., & Shatz, C. J. (1996). Thalamic relay of spontaneous retinal activity prior to vision. *Neuron*, 17(5). [https://doi.org/10.1016/S0896-6273\(00\)80218-4](https://doi.org/10.1016/S0896-6273(00)80218-4)
- Morgans, C. W., Zhang, J., Jeffrey, B. G., Nelson, S. M., Burke, N. S., Duvoisin, R. M., & Brown, R. L. (2009). TRPM1 is required for the depolarizing light response in retinal ON-bipolar cells. *Proceedings of the National Academy of Sciences of the United States of America*, 106(45), 19174–19178. <https://doi.org/10.1073/pnas.0908711106>
- Münch, T. A., Da Silveira, R. A., Siebert, S., Viney, T. J., Awatramani, G. B., & Roska, B. (2009). Approach sensitivity in the retina processed by a multifunctional neural circuit. *Nature Neuroscience*, 12(10). <https://doi.org/10.1038/nn.2389>
- Nawy, S. (2000). Regulation of the on bipolar cell mGluR6 pathway by Ca<sup>2+</sup>. *Journal of Neuroscience*, 20(12), 4471–4479. <https://doi.org/10.1523/jneurosci.20-12-04471.2000>
- Nelson, R., Famiglietti, E. V., & Kolb, H. (1978). Intracellular staining reveals different levels of stratification for on- and off-center ganglion cells in cat retina. *Journal of Neurophysiology*, 41(2), 472–483. <https://doi.org/10.1152/jn.1978.41.2.472>

- Nelson, R., & Kolb, H. (1985). A17: A broad-field amacrine cell in the rod system of the cat retina. *Journal of Neurophysiology*, 54(3). <https://doi.org/10.1152/jn.1985.54.3.592>
- Newman, E. A. (2005). Calcium increases in retinal glial cells evoked by light-induced neuronal activity. *Journal of Neuroscience*, 25(23). <https://doi.org/10.1523/JNEUROSCI.1354-05.2005>
- Nirenberg, S., & Meister, M. (1997). The light response of retinal ganglion cells is truncated by a displaced amacrine circuit. *Neuron*, 18(4). [https://doi.org/10.1016/S0896-6273\(00\)80304-9](https://doi.org/10.1016/S0896-6273(00)80304-9)
- O'Brien, J. (2019). Design principles of electrical synaptic plasticity. *Neuroscience Letters*, 695(August 2017), 4–11. <https://doi.org/10.1016/j.neulet.2017.09.003>
- Pak, T., Yoo, S., Miranda-Angulo, A. M., Wang, H., & Blackshaw, S. (2014). Rax-CreERT2 knock-in mice: A tool for selective and conditional gene deletion in progenitor cells and radial glia of the retina and hypothalamus. *PLoS ONE*, 9(4). <https://doi.org/10.1371/journal.pone.0090381>
- Paolicelli, R. C., Bolasco, G., Pagani, F., Maggi, L., Scianni, M., Panzanelli, P., ... Gross, C. T. (2011). Synaptic pruning by microglia is necessary for normal brain development. *Science*, 333(6048). <https://doi.org/10.1126/science.1202529>
- Pereda, A. E., Curti, S., Hoge, G., Cachope, R., Flores, C. E., & Rash, J. E. (2013). Gap junction-mediated electrical transmission: Regulatory mechanisms and plasticity. *Biochimica et Biophysica Acta - Biomembranes*, 1828(1). <https://doi.org/10.1016/j.bbamem.2012.05.026>
- Pillow, J. W., Shlens, J., Paninski, L., Sher, A., Litke, A. M., Chichilnisky, E. J., & Simoncelli, E. P. (2008). Spatio-temporal correlations and visual signalling in a complete neuronal population, 454(August). <https://doi.org/10.1038/nature07140>
- Plane, J. M., Shen, Y., Pleasure, D. E., & Deng, W. (2010). Prospects for minocycline neuroprotection. *Archives of Neurology*, 67(12). <https://doi.org/10.1001/archneurol.2010.191>
- Pouzat, C., Mazor, O., & Laurent, G. (2002). Using noise signature to optimize

- spike-sorting and to assess neuronal classification quality. *Journal of Neuroscience Methods*, 122(1). [https://doi.org/10.1016/S0165-0270\(02\)00276-5](https://doi.org/10.1016/S0165-0270(02)00276-5)
- Puñal, V. M., Paisley, C. E., Brecha, F. S., Lee, M. A., Perelli, R. M., Wang, J., ... Kay, J. N. (2019). Large-scale death of retinal astrocytes during normal development is non-apoptotic and implemented by microglia. *PLoS Biology*, 17(10). <https://doi.org/10.1371/journal.pbio.3000492>
- Rall, W. (1964). *Neural Theory and Modeling*. Stanford: Stanford University Press.
- Rashid, K., Akhtar-Schaefer, I., & Langmann, T. (2019). Microglia in retinal degeneration. *Frontiers in Immunology*. <https://doi.org/10.3389/fimmu.2019.01975>
- Raviola, E., & Gilula, N. B. (1973). Gap junctions between photoreceptor cells in the vertebrate retina. *Proceedings of the National Academy of Sciences of the United States of America*, 70(6), 1677–1681. <https://doi.org/10.1073/pnas.70.6.1677>
- Real, E., Asari, H., Gollisch, T., & Meister, M. (2017). Neural Circuit Inference from Function to Structure. *Current Biology*, 27(2), 189–198. <https://doi.org/10.1016/j.cub.2016.11.040>
- Reichardt, L. F. (2006). Neurotrophin-regulated signalling pathways. *Philosophical Transactions of the Royal Society B: Biological Sciences*. <https://doi.org/10.1098/rstb.2006.1894>
- Repérant, J., Ward, R., Miceli, D., Rio, J. P., Médina, M., Kenigfest, N. B., & Vesselkin, N. P. (2006). The centrifugal visual system of vertebrates: A comparative analysis of its functional anatomical organization. *Brain Research Reviews*. <https://doi.org/10.1016/j.brainresrev.2005.11.008>
- Ribelayga, C., Cao, Y., & Mangel, S. C. (2008). The Circadian Clock in the Retina Controls Rod-Cone Coupling. *Neuron*, 59(5). <https://doi.org/10.1016/j.neuron.2008.07.017>
- Rizzi, C., Tiberi, A., Giustizieri, M., Marrone, M. C., Gobbo, F., Carucci, N. M., ... Cattaneo, A. (2018). NGF steers microglia toward a neuroprotective phenotype. *Glia*, 66(7), 1395–1416. <https://doi.org/10.1002/glia.23312>

- Roska, B., & Werblin, F. (2001). Vertical interactions across ten parallel, stacked representations in the mammalian retina. *Nature*, *410*(6828). <https://doi.org/10.1038/35069068>
- Roy, K., Kumar, S., & Bloomfield, S. A. (2017). Gap junctional coupling between retinal amacrine and ganglion cells underlies coherent activity integral to global object perception. *Proceedings of the National Academy of Sciences of the United States of America*. <https://doi.org/10.1073/pnas.1708261114>
- Roy, S., & Field, G. D. (2019). Dopaminergic modulation of retinal processing from starlight to sunlight. *Journal of Pharmacological Sciences*. <https://doi.org/10.1016/j.jphs.2019.03.006>
- Sakai, H. M., & Naka, K. I. (1988). Dissection of the neuron network in the catfish inner retina. II. Interactions between ganglion cells. *Journal of Neurophysiology*, *60*(5), 1568–1583. <https://doi.org/10.1152/jn.1988.60.5.1568>
- Sakai, H. M., & Naka, K. I. (1990). Dissection of the neuron network in the catfish inner retina. V. Interactions between NA and NB amacrine cells. *Journal of Neurophysiology*, *63*(1), 120–130. <https://doi.org/10.1152/jn.1990.63.1.120>
- Sakata, L. M., DeLeon-Ortega, J., Sakata, V., & Girkin, C. A. (2009). Optical coherence tomography of the retina and optic nerve - A review. *Clinical and Experimental Ophthalmology*, *37*(1), 90–99. <https://doi.org/10.1111/j.1442-9071.2009.02015.x>
- Sakuranaga, M., & Naka, K. (1985). Signal transmission in the catfish retina. I. Transmission in the outer retina. *Journal of Neurophysiology*, *53*(2), 373–389. <https://doi.org/10.1152/jn.1985.53.2.373>
- Sanes, J. R., & Masland, R. H. (2015). The Types of Retinal Ganglion Cells : Current Status and Implications for Neuronal Classification, 221–248. <https://doi.org/10.1146/annurev-neuro-071714-034120>
- Santos, A. M., Calvente, R., Tassi, M., Carrasco, M. C., Martín-Oliva, D., Marín-Teva, J. L., ... Cuadros, M. A. (2008). Embryonic and postnatal development of microglial cells in the mouse retina. *Journal of Comparative Neurology*, *506*(2). <https://doi.org/10.1002/cne.21538>

- Schafer, D. P., Lehrman, E. K., Kautzman, A. G., Koyama, R., Mardinly, A. R., Yamasaki, R., ... Stevens, B. (2012). Microglia Sculpt Postnatal Neural Circuits in an Activity and Complement-Dependent Manner. *Neuron*, 74(4). <https://doi.org/10.1016/j.neuron.2012.03.026>
- Schein, S. J. (1988). Anatomy of macaque fovea and spatial densities of neurons in foveal representation. *Journal of Comparative Neurology*, 269(4). <https://doi.org/10.1002/cne.902690403>
- Sekaran, S., Lupi, D., Jones, S. L., Sheely, C. J., Hattar, S., Yau, K. W., ... Hankins, M. W. (2005). Melanopsin-dependent photoreception provides earliest light detection in the mammalian retina. *Current Biology*, 15(12). <https://doi.org/10.1016/j.cub.2005.05.053>
- Shekhar, K., Lapan, S. W., Whitney, I. E., Tran, N. M., Evan, Z., Kowalczyk, M., ... Cepko, C. L. (2017). Neurons By Single-Cell Transcriptomics, 166(5), 1308–1323. <https://doi.org/10.1016/j.cell.2016.07.054>. COMPREHENSIVE
- Shen, Y., Heimel, J. A., Kamermans, M., Peachey, N. S., Gregg, R. G., & Nawy, S. (2009). A transient receptor potential-like channel mediates synaptic transmission in rod bipolar cells. *Journal of Neuroscience*, 29(19), 6088–6093. <https://doi.org/10.1523/JNEUROSCI.0132-09.2009>
- Silverman, S. M., & Wong, W. T. (2018). Microglia in the retina: Roles in development, maturity, and disease. *Annual Review of Vision Science*. <https://doi.org/10.1146/annurev-vision-091517-034425>
- Simon, D. K., Prusky, G. T., O’Leary, D. D. M., & Constantine-Paton, M. (1992). N-Methyl-D-aspartate receptor antagonists disrupt the formation of a mammalian neural map. *Proceedings of the National Academy of Sciences of the United States of America*, 89(22). <https://doi.org/10.1073/pnas.89.22.10593>
- Simoncelli, E. P., Paninski, L., Pillow, J., & Schwartz, O. (2004). Characterization of Neural Responses with Stochastic Stimuli. *The Cognitive Neurosciences III*, 327–338. <https://doi.org/10.1161/CIRCULATIONAHA.108.827121>. A
- Srinivas, M., Rozental, R., Kojima, T., Dermietzel, R., Mehler, M., Condorelli, D. F., ... Spray, D. C. (1999). Functional properties of channels formed by the

- neuronal gap junction protein connexin36. *Journal of Neuroscience*, 19(22).  
<https://doi.org/10.1523/jneurosci.19-22-09848.1999>
- Sterling, P., & Matthews, G. (2005). Structure and function of ribbon synapses. *Trends in Neurosciences*, 28(1), 20–29.  
<https://doi.org/10.1016/j.tins.2004.11.009>
- Stringer, C., Pachitariu, M., Steinmetz, N., Reddy, C. B., Carandini, M., & Harris, K. D. (2018). Spontaneous behaviors drive multidimensional, brain-wide population activity. *BioRxiv*, 306019. <https://doi.org/10.1101/306019>
- Stuart, G. J., Dodt, H. U., & Sakmann, B. (1993). Patch-clamp recordings from the soma and dendrites of neurons in brain slices using infrared video microscopy. *Pflügers Archiv European Journal of Physiology*, 423(5–6).  
<https://doi.org/10.1007/BF00374949>
- Tachibana, M., & Kaneko, A. (1988). Retinal bipolar cells receive negative feedback input from GABAergic amacrine cells. *Visual Neuroscience*, 1(3).  
<https://doi.org/10.1017/S0952523800001954>
- Tengölics, Á. J., Szarka, G., Ganczer, A., Szabó-Meleg, E., Nyitrai, M., Kovács-Öller, T., & Völgyi, B. (2019). Response Latency Tuning by Retinal Circuits Modulates Signal Efficiency. *Scientific Reports*, 9(1).  
<https://doi.org/10.1038/s41598-019-51756-y>
- Thoreson, & Mangel. (2012). Lateral interactions in the vertebrate retina, 31(5), 407–441. <https://doi.org/10.1016/j.preteyeres.2012.04.003>. Lateral
- Tran, N. M., Shekhar, K., Whitney, I. E., Jacobi, A., Benhar, I., Hong, G., ... Sanes, J. R. (2019). Single-Cell Profiles of Retinal Ganglion Cells Differing in Resilience to Injury Reveal Neuroprotective Genes. *Neuron*, 104(6), 1039–1055.e12. <https://doi.org/10.1016/j.neuron.2019.11.006>
- Tremblay, M. Ě., Lowery, R. L., & Majewska, A. K. (2010). Microglial interactions with synapses are modulated by visual experience. *PLoS Biology*, 8(11).  
<https://doi.org/10.1371/journal.pbio.1000527>
- Trenholm, S., McLaughlin, A. J., Schwab, D. J., & Awatramani, G. B. (2013). Dynamic tuning of electrical and chemical synaptic transmission in a network of motion coding retinal neurons. *Journal of Neuroscience*, 33(37), 14927–

14938. <https://doi.org/10.1523/JNEUROSCI.0808-13.2013>
- Trenholm, S., McLaughlin, A. J., Schwab, D. J., Turner, M. H., Smith, R. G., Rieke, F., & Awatramani, G. B. (2014). Nonlinear dendritic integration of electrical and chemical synaptic inputs drives fine-scale correlations. *Nature Neuroscience*. <https://doi.org/10.1038/nn.3851>
- Trong, P. K., & Rieke, F. (2008). Origin of correlated activity between parasol retinal ganglion cells. *Nature Neuroscience*, *11*(11). <https://doi.org/10.1038/nn.2199>
- Vaney, D. I. (1990). Chapter 2 The mosaic of amacrine cells in the mammalian retina. *Progress in Retinal Research*. [https://doi.org/10.1016/0278-4327\(90\)90004-2](https://doi.org/10.1016/0278-4327(90)90004-2)
- Vaney, D. I. (1991). Many diverse types of retinal neurons show tracer coupling when injected with biocytin or Neurobiotin. *Neuroscience Letters*, *125*(2), 187–190. [https://doi.org/10.1016/0304-3940\(91\)90024-N](https://doi.org/10.1016/0304-3940(91)90024-N)
- Völgyi, B., Pan, F., Paul, D. L., Wang, J. T., Huberman, A. D., & Bloomfield, S. A. (2013). Gap Junctions Are Essential for Generating the Correlated Spike Activity of Neighboring Retinal Ganglion Cells. *PLoS ONE*. <https://doi.org/10.1371/journal.pone.0069426>
- Völgyl, B., Chheda, S., & Bloomfield, S. A. (2009). Tracer coupling patterns of the ganglion cell subtypes in the mouse retina. *Journal of Comparative Neurology*, *512*(5), 664–687. <https://doi.org/10.1002/cne.21912>
- Walløe, S., Pakkenberg, B., & Fabricius, K. (2014). Stereological estimation of total cell numbers in the human cerebral and cerebellar cortex. *Frontiers in Human Neuroscience*, *8*(JULY), 1–9. <https://doi.org/10.3389/fnhum.2014.00508>
- Wässle, H. (2004). Parallel processing in the mammalian retina. *Nature Reviews Neuroscience*, *5*(10), 747–757. <https://doi.org/10.1038/nrn1497>
- Wässle, H., Puller, C., Müller, F., & Haverkamp, S. (2009). Cone contacts, mosaics, and territories of bipolar cells in the mouse retina. *Journal of Neuroscience*, *29*(1), 106–117. <https://doi.org/10.1523/JNEUROSCI.4442-08.2009>
- Weng, S., Sun, W., & He, S. (2005). Identification of ON-OFF direction-selective

- ganglion cells in the mouse retina. *Journal of Physiology*, 562(3), 915–923.  
<https://doi.org/10.1113/jphysiol.2004.076695>
- Witkovsky, P., & Deary, A. (1991). Chapter 10 Functional roles of dopamine in the vertebrate retina. *Progress in Retinal Research*.  
[https://doi.org/10.1016/0278-4327\(91\)90031-V](https://doi.org/10.1016/0278-4327(91)90031-V)
- Wong, W. T., Myhr, K. L., Miller, E. D., & Wong, R. O. L. (2000). Developmental changes in the neurotransmitter regulation of correlated spontaneous retinal activity. *Journal of Neuroscience*, 20(1). <https://doi.org/10.1523/jneurosci.20-01-00351.2000>
- Wu, M. C.-K., David, S. V, & Gallant, J. L. (2006). Complete functional characterization of sensory neurons by system identification. *Annual Review of Neuroscience*. <https://doi.org/10.1146/annurev.neuro.29.051605.113024>
- Xiaojing, W. (2008). Decision Making in Recurrent Neuronal Circuits. *Neuron*, 60(2), 215–234. <https://doi.org/10.1016/j.neuron.2008.09.034>.Decision
- Xin, D., & Bloomfield, S. A. (1999). Dark- and light-induced changes in coupling between horizontal cells in mammalian retina. *Journal of Comparative Neurology*, 405(1), 75–87. [https://doi.org/10.1002/\(SICI\)1096-9861\(19990301\)405:1<75::AID-CNE6>3.0.CO;2-D](https://doi.org/10.1002/(SICI)1096-9861(19990301)405:1<75::AID-CNE6>3.0.CO;2-D)
- Yamada, E., & Ishikawa, T. (1965). The fine structure of the horizontal cells in some vertebrate retinæ. *Cold Spring Harbor Symposia on Quantitative Biology*, 30. <https://doi.org/10.1101/SQB.1965.030.01.038>
- Yan, W., Laboulaye, M. A., Tran, N. M., Whitney, I. E., Benhar, I., & Sanes, J. R. (2020). Mouse Retinal Cell Atlas: Molecular Identification of over Sixty Amacrine Cell Types. *Journal of Neuroscience*, 40(27), 5177–5195. <https://doi.org/10.1523/JNEUROSCI.0471-20.2020>
- Yau, K. W., & Hardie, R. C. (2009). Phototransduction Motifs and Variations. *Cell*, 139(2), 246–264. <https://doi.org/10.1016/j.cell.2009.09.029>
- Yger, P., Spampinato, G. L. B., Esposito, E., Lefebvre, B., Deny, S., Gardella, C., ... Marre, O. (2018). A spike sorting toolbox for up to thousands of electrodes validated with ground truth recordings in vitro and in vivo. *ELife*, 7. <https://doi.org/10.7554/eLife.34518>

- Young, R. W. (1984). Cell death during differentiation of the retina in the mouse. *Journal of Comparative Neurology*, 229(3). <https://doi.org/10.1002/cne.902290307>
- Young, R. W. (1985). Cell differentiation in the retina of the mouse. *The Anatomical Record*, 212(2). <https://doi.org/10.1002/ar.1092120215>
- Zhang, A. J., & Wu, S. M. (2009). Receptive fields of retinal bipolar cells are mediated by heterogeneous synaptic circuitry. *Journal of Neuroscience*, 29(3). <https://doi.org/10.1523/JNEUROSCI.4984-08.2009>
- Zhang, A. J., & Wu, S. M. (2010). Responses and receptive fields of amacrine cells and ganglion cells in the salamander retina. *Vision Research*, 50(6). <https://doi.org/10.1016/j.visres.2010.01.009>
- Zhang, C., Kolodkin, A. L., Wong, R. O., & James, R. E. (2017). Establishing Wiring Specificity in Visual System Circuits: From the Retina to the Brain. *Annual Review of Neuroscience*, 40(1), 395–424. <https://doi.org/10.1146/annurev-neuro-072116-031607>
- Zhang, Y., Kim, I. J., Sanes, J. R., & Meister, M. (2012). The most numerous ganglion cell type of the mouse retina is a selective feature detector. *Proceedings of the National Academy of Sciences of the United States of America*, 109(36), E2391–E2398. <https://doi.org/10.1073/pnas.1211547109>
- Zhao, L., Zabel, M. K., Wang, X., Ma, W., Shah, P., Fariss, R. N., ... Wong, W. T. (2015). Microglial phagocytosis of living photoreceptors contributes to inherited retinal degeneration. *EMBO Molecular Medicine*, 7(9). <https://doi.org/10.15252/emmm.201505298>